

An Electrothermally-Actuated Bistable MEMS Relay for Power Applications

by

Jin Qiu

M.S. Mechanical Engineering, M.I.T. 1999
B.S. Electrical Engineering, Nanjing University 1997

Submitted to the Department of Mechanical Engineering
in Partial Fulfillment of the Requirements for the Degree of

Doctor of Philosophy in Mechanical Engineering

at the

Massachusetts Institute of Technology

June 2003

© Massachusetts Institute of Technology 2003. All rights reserved.

Author
Department of Mechanical Engineering
May 27, 2003

Certified by.....
Alexander H. Slocum
Professor of Mechanical Engineering
Thesis Supervisor

Certified by.....
Jeffrey H. Lang
Professor of Electrical Engineering
Thesis Supervisor

Accepted by.....
Professor Ain A. Sonin
Chairman, Department Committee on Graduate Students

An Electrothermally-Actuated Bistable MEMS Relay for Power Applications

by

Jin Qiu

(E-mail, jqiu@alum.mit.edu)

Submitted to the Department of Mechanical Engineering on May 27, 2003
in Partial Fulfillment of the Requirements for the Degree of
Doctor of Philosophy in Mechanical Engineering

ABSTRACT

This thesis first develops a bistable mechanism that does not rely on internal stress or hinges for its bistability, which is then combined with transient electrothermal actuation and contact structure to develop a MEMS relay for power switching. The relay components, fabricated by a through etch of a silicon wafer using deep reactive ion etch (DRIE), move laterally in the plane of the wafer. The synthesis, analysis, design, fabrication and testing of the relay are all described in this thesis.

The bistable mechanism comprises two parallel cosine curved clamped-clamped beams that are also clamped together at their centers. If designed properly it exhibits a second stable deflected shape that is nearly a mirror image of its as-fabricated shape mirrored through the centerline connecting its clamped ends. Both theoretical and finite-element analyses are applied to the modeling, design and optimization of the force-displacement characteristic of the curved beam mechanism. The analyses results agree well with experimental measurement after accounting for fabrication variations. If fabricated properly, the mechanism is mechanically robust; some mechanisms have been switched between their bistable states one million times without sign of failure.

The bistable mechanism is combined with two contacts to form a crossbar relay. The contact structure is designed with flat shape and additional compliance; and proper metalization process is developed for its DRIE etched sidewalls; both contributing to a more reliable and low resistance contact. Because of bistability this relay requires no actuation power in either its on or off states. Therefore, transient electrothermal actuators to switch its states are designed, partially with a mechanical model developed for cantilevers subjected to both lateral and axial forces. These actuators typically require 1-ms 50-V pulses to switch the relay. In the off state, the relay contacts stand off more than 200 V. In the on state the best relay contacts exhibit a total resistance of 60 m Ω and a current carrying capacity of 3 A. The relay can switch at a maximum 5 Hz rate. These characteristics make it a good candidate for power protection applications.

Thesis committee:

Alexander H. Slocum (Chairman), Professor of Mechanical Engineering

Jeffrey H. Lang, Professor of Electrical Engineering

Martin A. Schmidt, Professor of Electrical Engineering

ACKNOWLEDGEMENTS

First of all I thank my advisors Professor Jeffrey Lang and Professor Alexander Slocum for their encouragement, guidance, input and discussion in the last four years. Thank Jeff for appointing me to work on this project, from which I surely got exposed to many things. Thank Alex for accommodating me in his precision engineering research group, and for many aspects of care he gave to make me feel at home.

I thank Professor Martin Schmidt for being my thesis committee member and for his helpful suggestions; Professor Nicolas Hadjiconstantinou for appointing me a TA position during the course of this thesis project; my master degree advisor Professor Zaichun Feng for initially bringing me to MIT.

I thank many MTL staffs including Kurt Broderick, Dr. Vicky Diadiuk, Gwen Donahue, Paul Tierney, and Dennis Ward for fabrication training and assistance; Ramkumar Krishnan for help with electroplating; Professor L. Mahadevan for help with beam modeling in electrostatic field; and Chris Spadaccini for help with IR camera experiment. I thank many groupmates for help and working together including but not limited to Jian Li, Jose Oscar Miranda, Joachim Sihler, and Victoria Sturgeon.

I thank my parents Yande Qiu and Luping Chen, who raised me up and created an environment in which I could concentrate on pursuing intellectual pleasures. When visiting me during the beginning of this thesis project, they supported me to immerse in the work on the bistable stuff without a single complaint about my regrettably very lack of time spending with them. I thank my wife Yi Sun for loving me and bringing to my life joy, dimension, and more responsibilities, all of which make a Doctor's degree much more meaningful. This thesis is dedicated to my family.

Finally, I thank ABB for sponsoring this project, as well as for some testing and metrology help from the ABB group of Sami Kotilainen, Jan Henning and Ralf Struempler.

TABLE OF CONTENT

ABSTRACT	2
ACKNOWLEDGEMENTS	3
LIST OF FIGURES	7
LIST OF TABLES	9
LIST OF SYMBLES	10
CHAPTER 1	13
Introduction	13
1.1 Technology foundations.....	13
1.1.1 MEMS technology	13
1.1.2 Flexure mechanisms.....	14
1.2 Overview of the relay.....	15
1.2.1 Background	15
1.2.2 Basic process and design.....	17
1.3 Thesis layout	18
CHAPTER 2	19
Curved beam bistable mechanism.....	19
2.1 Introduction to bistable mechanism	19
2.2 Modeling of curved beam	20
2.2.1 Buckling of straight beam	20
2.2.2 Equation formation for curved beam	22
2.2.3 Solution with higher mode neglected.....	26
2.2.4 Solution with higher modes included.....	28
2.2.5 Comparison of the solutions and FEA	29
2.3 Design of curved beam bistable mechanism.....	30
2.4 Fabrication and testing of curved beam mechanism	32

2.5 Optimization of curved beam mechanism	36
2.5.1 Optimization of the force-displacement curve symmetry	36
2.5.2 Optimization of the force-displacement curve stiffness	39
CHAPTER 3	40
Actuators	40
3.1 Electrothermal actuator	40
3.1.1 Mechanical modeling approach	41
3.1.2 Basic mechanical model.....	42
3.1.3 Complete mechanical model.....	43
3.1.4 Mechanical model comparison and design	46
3.1.5 Electrothermal modeling and design.....	47
3.2 Electrostatic actuators considered.....	50
3.2.1 Feasibility study of comb drive type actuators	50
3.2.2 Preliminary study of zipper actuators	52
CHAPTER 4.....	58
Relay contact.....	58
4.1 Mechanical design of the contact.....	58
4.1.1 Identification of ideal contact shape	58
4.1.2 Design of contact compliance	59
4.2 Process development for DRIE sidewall contact.....	60
4.2.1 Challenges.....	60
4.2.2 Alleviation of bottom-of-etch problem	61
4.2.2.1 Direct mounting method	62
4.2.2.2 Backside shallow etch method.....	64
4.2.3 Sidewall surface treatment and metalization	65
4.2.3.1 Sidewall cleaning and seed metal layer deposition.....	65
4.2.3.2 Wet etch process for smoothing the sidewall	67
4.2.3.3 Electroplating.....	70
4.2.4 Edge nibble method for metal continuity across edge	70

CHAPTER 5	72
The relays	72
5.1 Design.....	72
5.2 Fabrication.....	74
5.3 Testing.....	76
CHAPTER 6	82
Summary and conclusions.....	82
APPENDIX A	84
MatLab code of the thermal actuator complete model.....	84
APPENDIX B.....	88
Masks	88
APPENDIX C	92
Fabrication process flow	92
BIBLIOGRAPHY	93

LIST OF FIGURES

Figure 1-1 Basic fabrication method.....	17
Figure 1-2 The effect of fabrication process on the development of this relay	17
Figure 1-3 Relay plan view.....	18
Figure 2-1 General behavior of bistable mechanisms.....	19
Figure 2-2 Clamped-clamped beam buckling modes	21
Figure 2-3 Geometry and notation for curved beam deflection analysis.....	22
Figure 2-4 F- Δ relations of curved beam	27
Figure 2-5 f-d curve for a second-mode-constrained curved beam when $Q \gg 1$	28
Figure 2-6 Comparison of theoretical models and FEA for curved beam.....	30
Figure 2-7 Double curved beam versus single curved beam	30
Figure 2-8 The bistable mechanism as pushed manually by a probe.....	32
Figure 2-9 SEM of a beam fabricated with DRIE	33
Figure 2-10 Flextester for measuring MEMS force-displacement curve	35
Figure 2-11 Comparison of f-d curve from theory, FEA and measurement.....	35
Figure 2-12 A three-hinge bistable mechanism	37
Figure 2-13 Curved beam with cosine thickness modulation.....	37
Figure 2-14 FEA study of cosine thickness modulated beams	38
Figure 2-15 f-d curve by FEA for the cosine thickness modulated beam mechanisms.....	39
Figure 2-16 Double beam with softspring	39
Figure 3-1 Schematic of the electrothermal actuator.....	40
Figure 3-2 Thermal actuator mechanical model	41
Figure 3-3 Treatment of the cantilever in the basic and the complete models	41
Figure 3-4 Comparison of thermal actuator model results	46
Figure 3-5 Electrothermal actuator driving circuit	49
Figure 3-6 f-d curves of three comb drive type electrostatic actuator units	51
Figure 3-7 f-d curve for electrostatic taper comb drive and bistable mechanism.....	52
Figure 3-8 Electrostatic zipper actuator with rolling contact.....	53
Figure 3-9 A zipper actuator concept with flexible elements	57
Figure 4-1 Contact geometry explored	58

Figure 4-2 f-d characteristic of double beam and softspring-coupled crossbar	59
Figure 4-3 Microscope picture of the cantilever and the closed contacts	60
Figure 4-4 Regular wafer mounting method for DRIE through-etch.....	61
Figure 4-5 SEM pictures of the bottom of DRIE etched beams	62
Figure 4-6 Direct mounting method.....	62
Figure 4-7 Backside shallow etch method	64
Figure 4-8 The clear bottom of etch with backside shallow etch method.....	64
Figure 4-9 Metalization quality measurement method	66
Figure 4-10 Metal on DRIE sidewall with many grooves	67
Figure 4-11 Sidewalls of DRIE etched structure after wet etch.....	68
Figure 4-12 Poor metal continuity across the edge between wafer top and sidewall	70
Figure 4-13 Edge nibble concept	70
Figure 4-14 Edge nibble patterns	71
Figure 5-1 Key fabrication steps	74
Figure 5-2 Au plated relay in G14	77
Figure 5-3 Bistability of G15 and G16. b (bistable) m(monostable), x(broken)	77
Figure 5-4 Cu plated relay in G15 after annealing.....	78
Figure 5-5 Upper thermal actuator in G15 after cyclic actuation	78
Figure 5-6 G11 pictures.....	79
Figure 5-7 IR image of the thermal actuator in G18.....	79
Figure 5-8 Switch-on contact response in G18.....	80
Figure 5-9 f-d measurement of the bistable mechanism in G18	81
Figure B-1 Device mask.....	88
Figure B-2 Device backside mask.....	89
Figure B-3 Handle mask	90
Figure B-4 Shadow mask	91

LIST OF TABLES

Table 1-1 Performance of several MEMS relays for power applications.....	16
Table 1-2 Functional requirements of this relay	16
Table 2-1 A design of bistable double beam for the relay	31
Table 2-2 Thickness modulation optimized results	39
Table 3-1 Requirement and design of the thermal actuator used in the relay.....	47
Table 3-2 Comparison of parallel plate, comb drive, and taper comb drive actuators	50
Table 4-1 Design of a contact structure	60
Table 4-2 Challenges of the DRIE sidewall relay contact and solutions.....	61
Table 4-3 Test runs for the direct mounting method	63
Table 4-4 Metalization process matrix and resistance measurement.....	66
Table 4-5 Measured resistance for wet etched channels.....	69
Table 4-6 Measured resistance for edge nibbled channels	71
Table 5-1 Guidelines of design for fabrication of the relay.....	72
Table 5-2 Characteristics of the design of relays with large and small dimensions	73
Table 5-3 Relay mask set chart.....	74
Table 5-4 Relay device chart	75
Table C-1 Fabrication process flow	92

LIST OF SYMBLES

A_j	Normalized amplitude of the j^{th} beam buckling mode
\bar{A}_j	Normalized initial amplitude of the j^{th} beam buckling mode
b	Width (depth) of beam
$c (C)$	Coordinate (normalized) of the contact point of rolling boundary beam
d	Displacement. Or maximum stroke of comb drive type actuators
d_{bot}	Displacement at minimum force of curved beam
d_{top}	Displacement at maximum force of curved beam
d_{end}	Displacement at the second stable position of curved beam
d_{zero}	Displacement at unstable zero force position of curved beam
E	Young's modulus
$f(F)$	Force (normalized)
$f_c (F_c)$	Force (normalized) on the cold beam in thermal actuator
f_{block}	Blocked force of thermal actuator
f_{dbbot}	Minimum force in a double curved beam f-d curve
f_{dbtop}	Maximum force in a double curved beam f-d curve
f_e	Electrical force per unit length
$f_h (F_h)$	Force (normalized) on the hot beam in thermal actuator
$f_{bot} (F_{bot})$	Min. force (normalized) in a 2nd-mode-constrained curved beam f-d curve
$f_{top} (F_{top})$	Max. force (normalized) in a 2nd-mode-constrained curved beam f-d curve
F_1	First kind of solution for normalized lateral force in curved beam modeling
F_2	Second kind of solution for normalized lateral force in curved beam modeling
F_3	Third kind of solution for normalized lateral force in curved beam modeling
g	Gap between comb drive teeth
h	Initial apex height of a curved beam
I	Moment of inertia of beam
I_c	Moment of inertia of cold beam in thermal actuator
I_h	Moment of inertia of hot beam in thermal actuator
l	Horizontal span of beam
$l_c (L_c)$	Initial length (normalized) of the cold beam in thermal actuator
l_{diff}	Thermal diffusion length

l_h	Initial length of the hot beam in thermal actuator
$m (M)$	Moment (normalized)
$m_c (M_c)$	Moment (normalized) on cold beam in thermal actuator
$m_h (M_h)$	Moment (normalized) on hot beam in thermal actuator
N	Square root of normalized beam axial force
N_c	Square root of normalized hot beam axial force in thermal actuator
N_h	Square root of normalized cold beam axial force in thermal actuator
N_j	Square root of normalized axial force of the j^{th} beam buckling mode
N_p^2	Intermediate variable in beam analysis
p	Axial compression force of beam
Q	Ratio of initial apex height and thickness of a curved beam
r	Asymmetric factor of a curved beam f-d curve
$s (S)$	Curved length (normalized) of beam
$t (T)$	Thickness (normalized) of beam
t_a	Average beam thickness of a cosine-modulated curved beam
$t_c (T_c)$	Thickness (normalized) of cold beam in thermal actuator
t_{diff}	Thermal diffusion time
t_g	Gap between hot and cold beam in thermal actuator
$t_h (T_h)$	Thickness (normalized) of hot beam in thermal actuator
T_{rise}	Temperature rise in hot beam in thermal actuator
$t_0 (T_0)$	Distance (normalized) between hot and cold beam center in thermal actuator
$u_b (U_b)$	Bending energy (normalized) in a curved beam
$u_f (U_f)$	External force energy (normalized) in a curved beam
$u_s (U_s)$	Compression energy (normalized) in a curved beam
U_t	Normalized total energy in a curved beam
$v (V)$	Voltage (normalized)
$w (W)$	Lateral beam deflection (normalized)
$w_j (W_j)$	Mode shape (normalized) of the j^{th} beam buckling mode
w_t	Width of comb drive teeth
$\bar{w} (\bar{W})$	Initial shape (normalized) of a curved beam
$x (X)$	Coordinate (normalized) of beam
\tilde{X}	Re-normalized coordinate of beam with rolling boundary
y	Gap
$z (Z)$	Oxide layer thickness

α	Thermal expansion rate for the thermal actuator
β	Ratio of maximum and minimum modulated beam thicknesses
ε	Beam compression strain
ε_{\max}	Maximum beam compression strain
ε_a	Thermal strain in the hot beam of thermal actuator
ε_{ox}	Relative electrical permittivity in oxide
ε_0	Electrical permittivity in vacuum
δ	Beam tip displacement
δ_{free}	Free displacement of thermal actuator
Δ	Normalized displacement
Δ_c	Normalized cold beam displacement in thermal actuator
Δ_h	Normalized hot beam displacement in thermal actuator
η	Ratio of beam tip axial displacement and beam length
$\theta (\Theta)$	Beam tip rotation (normalized)
$\theta_c (\Theta_c)$	Cold beam tip rotation (normalized)
$\theta_h (\Theta_h)$	Hot beam tip rotation (normalized)

Chapter 1

INTRODUCTION

This thesis concerns the design, modeling, fabrication and testing of an electrothermally actuated bistable MEMS relay for power applications. Two key technologies that enable this thesis are MEMS technology and flexure mechanism design and modeling. This chapter describes these two foundational technologies, introduces the specifications, basic fabrication, and configuration of the relay, and finally gives an overview of the thesis.

The fundamental contributions of this thesis to these two technologies are (1) Design, modeling and optimization of a curved beam bistable mechanism; (2) Design and modeling of an electrothermal actuator, especially a mechanical model developed to capture the beam force-deflection cross-coupling effects between the lateral and axial directions; (3) Design and process development to achieve good metalization and relay contact through deep reactive ion etched sidewalls.

1.1 Technology foundations

1.1.1 MEMS technology

MEMS is an acronym for *Micro Electro Mechanical Systems* [1][2][3]. It uses fabrication processes that are similar or identical to Integral Circuit (IC) fabrication processes to make micro scale devices and systems that involve mechanical motions. This technology was originated in the 1980's principally by electrical engineers who designed and fabricated IC circuits. Recently engineers from other fields, especially mechanical engineering, have focused on MEMS. The application of MEMS has also grown from simple sensors and actuators to optical devices, bio- and chemical systems etc.

As the name suggests, MEMS has the scale on the order of microns, but in reality, most MEMS devices range in size from microns to even centimeters. MEMS devices are mostly built on silicon wafers. Other materials are also used, for example, Pyrex wafers and deposited metals. Each MEMS device goes through a series of micro fabrication steps, mostly in clean rooms where there are only 10-100 particles per cubic meter. These micro fabrication steps include photolithography, deep reactive ion etching (DRIE), bonding, various cleaning process by chemicals or plasmas, and thin film deposition including metal and silicon oxide.

MEMS is an ideal candidate for micro devices for several reasons. First, many fabrication technologies have already been developed by the IC industry. These technologies have great precision and they are usually batch processes. Taking direct advantage of these, MEMS can

build devices with great precision, minimum assembly, and low cost. MEMS devices are also more easily integrated with integrated circuits. However, MEMS also faces challenges, such as low yield and high packaging cost, which are typically related to new technologies. In addition, variations in wafer processing can affect performance because etch widths vary, and many mechanical system performance metrics depend on the stiffness of mechanical components.

With respect to design engineering, most physical relations still hold the same for MEMS as in macro world, but the relative orders of importance of different physical phenomena are very different in the micro world. For example, on the micro scale, the inertial and magnetic forces are less prominent, while surface tension and electrostatic forces are more significant. Designs of micro systems should take this into account, and more importantly, take advantage of these new relations. Another important effect of MEMS on its design is its 2D nature. Most MEMS structures are 2D structures stacked together, though the structure creating and stacking methods can vary a lot. It is hard to implement many components common in macro world, such as screws, hinges etc. Thus, one task of MEMS design is to find specific micro mechanisms that can be easily fabricated and that have good performance. MEMS are also fragile, effects such as surface tension from wet processing and resonance during processing and handling can cause breakage. Designs should take such factors into account. For example, the rule of thumb to prevent breakage from resonance during fabrication and handling is to have all structural natural frequencies above $1k\text{ Hz}$.

1.1.2 Flexure mechanisms

Flexure mechanisms are natural candidates for MEMS. There are two important elements of all mechanisms, those that allow movement such as joints and ball bearings, and those that transmit force or displacements such as links. With flexures, these two functions are realized together by compliant structures. Such flexure mechanisms are usually made from one monolithic element. Due to the distributed compliance along them, analysis and design of flexures is complex.

A simple beam is the most basic and important flexure mechanism. The application of beams in MEMS include cantilevers (AFM tip, inertial accelerometers), folded crab leg bearings, etc. The main goal of beam structure analysis is to find the response (deflection, speed etc) to external actuation (force, moment etc) under certain constraints (boundary conditions etc). The micro behavior of beams is readily described by classical beam equations expressed in a derivative form [1]–Section 9.3.5. But the macro behavior of beams could be more complex than a simple cantilever. The challenges of beam modeling lies in the fact that it is a continuum structure, the response of any segment of the beam depends not only on the external actuation but also on all other segments of the beam.

One powerful modeling technique is the energy method [1]-chapter 10. It divides the beam response into two elements, the shape and the amplitude. Shape is then guessed or deliberately selected and the amplitude is solved analytically by the minimum energy argument, which states that the response of the beam is such that the sum of the internally stored structural energy and the external actuation energy reaches a minimum at its

amplitude of deflection. Common energy method guesses one shape and solves for one amplitude, and the solution is approximate. By the same minimum energy argument, more modes of the shape can be used and an equal number of amplitudes can be solved too. If the number of modes used is infinite, an exact solution can be reached. The curved beam analysis in this thesis is such an example.

Another modeling technique is to solve for the exact beam solution by differential equations. With concentrated lateral actuations, a second order beam equation is sufficient. But when there is either axial force, or distributed lateral actuation such as when the beam is in an electrostatic field, usually a fourth order beam equation is needed. Simple equations can be found in many textbooks for the lateral response subject to lateral actuation. Buckling equations also exist for a beam subject to pure axial actuation, which gives a critical value above which the beam buckles. But very few treatments can be found in the literature for beams subject to both lateral and axial actuations, beyond the use of energy methods. This thesis works on this in the complete model of the thermal actuator.

Still another beam modeling technique is by lumped parameter modeling. It determines the beam shape first by the two methods mentioned above or by FEA or experiment, and then observes the solution and simplifies them so the beam behavior is described by a lumped parameter system. An example is the BYU work [4].

1.2 Overview of the relay

1.2.1 Background

While the same basic action of relays is to switch on and off a circuit, their working principle, manufacture, and application vary significantly. Mechanical relay driven by magnetic coils are probably the oldest and most commonly seen type, which offers low on-state resistance and high off-state resistance. Solid state relay [5] fabricated by semiconductor processing is low cost and can be easily integrated with electronics, but usually has a high on-state resistance and low off-state resistance. Relays can employ other working principles, such as a device described in [6] which takes advantage of the positive temperature coefficient of a specialized polymer.

MEMS relay is basically miniature mechanical relay fabricated by MEMS technologies. Due to its mechanical nature and silicon processing, MEMS relay can potentially have both advantage of mechanical relay and solid state relay. The development of MEMS relays has attracted considerable attention in recent years. Relays have been fabricated through surface [7][8][9][10] and bulk [11][12] micro-machining, have employed electrical [10][11], magnetic [8][12] and thermal [7][9] actuation, have employed monostable [7][9][10][11][12] and bistable [8] structures, and have employed lateral [7][9] and vertical [8][10][11][12] moving contacts. One relay has employed liquid metal movement [9]. The applications have ranged from signal [7][8][9] to power [10][11][12] switching. For power switching applications, the lowest reported on-state resistance is 15 m Ω [11] and the highest reported

current-carrying capacity is several Amperes [10]. Table 1-1 shows the performance of several relays for power applications, which also includes the relay developed by this thesis.

Table 1-1 Performance of several MEMS relays for power applications

Developer	Delphi	MIT Wang	Georgia Tech	This thesis
Actuation	Electrostatic	Electrostatic	Magnetic	Thermal
Stability	Mono	Mono	Mono	Bi
Actuation voltage	20 V			50 V
Actuation power		20 W	33 mW	50 W, 1 ms
Trip time	0.05 ms	20-50 ms	0.5-2.5 ms	1.5-2.5 ms
Max on current	several A	0.4 A	3 A	3 A
On-Resistance	30 m Ω	15-50 m Ω	1.3 Ω	60 m Ω
Contact force			2.5 mN	1 mN
Frequency			>1 k Hz	<5 Hz
Off-resistance		>3e7 Ω	1e10 Ω	>3e7 Ω
Gap			10 μ m	>50 μ m
Reference	[10]	[11]	[12]	Partial result in [13]

This relay is developed as the mechanical component of a power protection device. The intended configuration of the device has a MEMS relay component and an electronic control component. The electronic component senses the abnormality of AC power and sends a signal to the relay, which can be switched off as the AC voltage passes through zero to prevent arcing problems. The requirement of the relay thus is to have good on-state and off-state characteristics, and high switching speed. Since power abnormalities are relatively rare events, the operational frequency of the relay is not emphasized. Table 1-2 shows the functional requirements as given by ABB, the sponsoring company of this project. Contact resistance is a function of contact force among other things. To have a low resistance, the force required is assumed to be 1 mN. In order to have a large stand-off voltage when the relay is at the off-state, a minimum gap between the contacts is given as 24 μ m. To be able to switch the relay at zero AC voltage, the speed of the switching is required to be less than 4 ms.

Table 1-2 Functional requirements of this relay

Contact force	>1 mN
Contact gap	> 24 μ m
Switching time	< 4 ms
Size	< 7 mm by 7 mm by 1 mm
Cost	~ \$ 2
Ampacity	Several amps
Switching frequency	Not critical
Power consumption	Bistable
Life time	> Thousands switch

1.2.2 Basic process and design

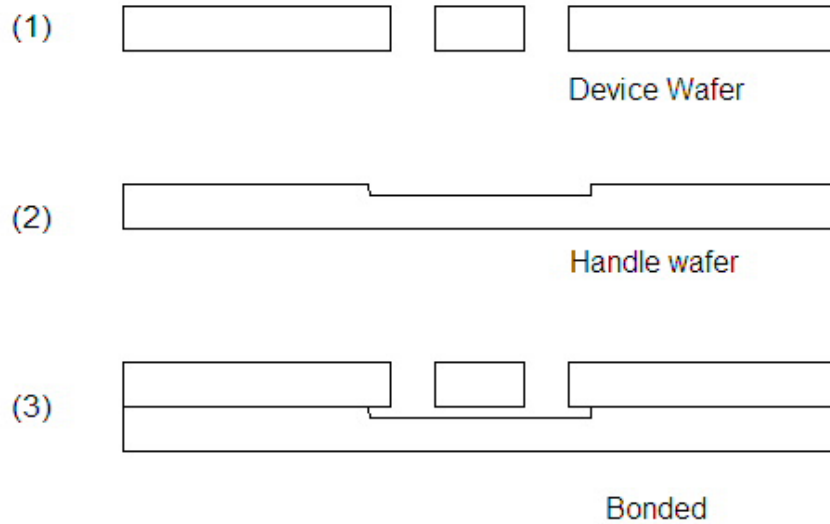


Figure 1-1 Basic fabrication method

The key factors make the relay reported in this thesis different than those found in literature are its straightforward fabrication method and its mechanical bistability. With these two main features, the relay can have many advantages over existing ones. A basic fabrication scheme is shown in Figure 1-1. A silicon device wafer is through-etched by DRIE and bonded to a handle wafer that has shallow etched pits, above which the device feature can move. As can be seen, all relay components move in the direction parallel to the wafer plane, thus the contact happens through the sidewalls of DRIE etched beams being pushed against each other. The sidewalls are deep etched surfaces, which do not have perfectly planar surfaces. This poses challenges that are one of the main topics of this thesis. Figure 1-2 summarizes the effect of the process on the development of this relay.



Figure 1-2 The effect of fabrication process on the development of this relay

The relay reported in this thesis is a bulk-micromachined electrothermally-actuated bistable lateral relay for power applications. The bulk micromachined structure ensures good thermal diffusion at the relay contact, which together with a low contact resistance, contributes to a high current-carrying capacity. Compared with other actuators, the thermal actuator has a larger force and stroke, and requires a lower driving voltage. When coupled with a bistable

relay, the disadvantage of high power required for thermal actuation is minimized by requiring only the small transient energy consumed during the actuation of a bistable relay.

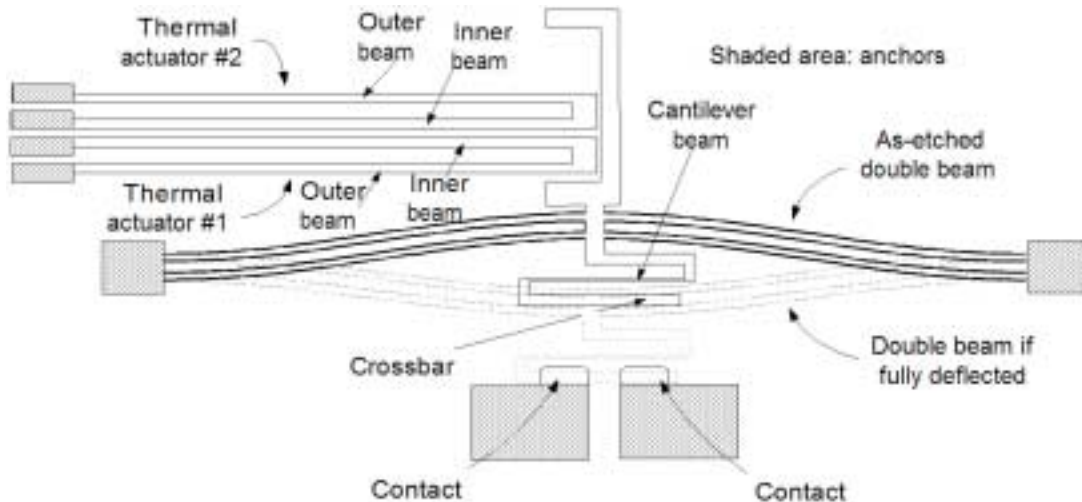


Figure 1-3 Relay plan view

Figure 1-3 shows the relay plan view, with shaded areas anchored to a handle wafer. All moving components of the relay are through-etched by DRIE of a silicon wafer. At the center is a mechanically bistable pre-curved double beam that moves laterally in the wafer plane. A crossbar is attached to the double beam by a cantilever beam. When the double beam is in its as-etched position (solid lines) the two contacts below the crossbar are not connected, and the relay is off. When the double beam snaps toward its second stable position (dashed lines), it pushes the crossbar against the two contacts, and the relay is on. Good electrical contact is ensured through metal deposited on the etched sidewalls; flat contacts have experimentally proven to give the best electrical contact. Thermal actuator #1 in Figure 1-3 deflects downward to close the relay. Thermal actuator #2 deflects upward to open the relay.

1.3 Thesis layout

Chapter 1 describes the background of the relay; the basic process and final device layout are also given. Three main components comprise the relay: the bistable mechanism, the thermal actuator and the contact. The following three chapters each describe one of these components. Chapter 2 describes the design, modeling, optimization, fabrication and testing of a curved beam bistable mechanism. Chapter 3 describes the design and modeling of the actuators. In Section 3.1 the electrothermal actuator is presented, and in Section 3.2 some electrostatic actuation considered are presented. Chapter 4 describes both the mechanical design and process development for the relay contact. Chapter 5 describes the design, fabrication and testing of the whole relays. Chapter 6 summarizes and concludes this thesis. In appendixes, a Matlab script for the mechanical modeling of thermal actuator, a set of mask artworks, and a detailed fabrication process flow for the relay and are presented.

Chapter 2

CURVED BEAM BISTABLE MECHANISM

2.1 Introduction to bistable mechanism

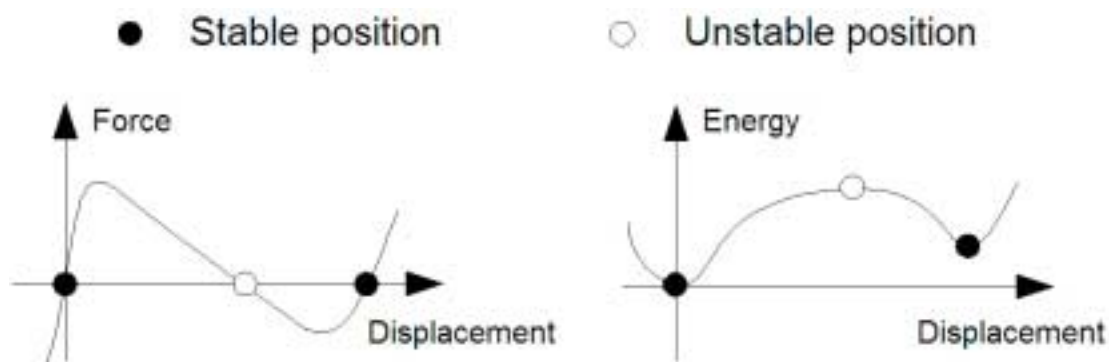


Figure 2-1 General behavior of bistable mechanisms

Mechanically-bistable mechanisms are useful in MEMS devices such as relays, valves, clips, threshold switches and memory cells etc. One advantage of such mechanisms is that they can apply a force to a contact without actuation power. A bistable structure has two positions or shapes where its elastic energy is at a local minimum. Usually, an external force is applied to the bistable structure to switch it between two stable positions. The bistable behavior can be characterized by either energy or force versus displacement (or deflection) plots. Both plots are presented in Figure 2-1. Figure 2-1 (a) shows the force-displacement plot, the curve has a range of negative stiffness and a range of negative force. Figure 2-1 (b) is an integration of Figure 2-1 (a), which yields an energy plot. Usually the energy or force versus displacement curve is not symmetric for the two stable positions.

Three main categories of bistable mechanisms have been reported in the MEMS literature: latch-lock mechanisms [14][15], hinged multi-segment mechanisms [4][16][17], and residual-compressive-stress buckled beam or membrane mechanisms [18][19][20]. The latch-lock mechanisms require complex actuation to lock and unlock; the hinges (zero friction, zero clearance, and zero stiffness) are hard to realize generally in MEMS process, and especially in deep reactive ion etch (DRIE) process; the residual stress is hard to realize or control in bulk fabricated structures; so all these bistable mechanisms are not ideal, if not impossible, for this relay. Various bistable design concepts were designed, modeled and compared in [21]. A novel monolithic bistable mechanism selected is presented in this chapter, also in [22][32][34], that uses no latches, no hinges, and no residual stress to achieve its bistability. This mechanism is easy to fabricate using DRIE.

2.2 Modeling of curved beam

2.2.1 Buckling of straight beam

The design of a curved beam bistable mechanism proposed in this thesis is inspired from the bistable buckled straight beam mechanism, where a straight beam is axially compressed to buckle to stable positions at either side. The buckling modes of the latter mechanism are critical in the modeling of the curved beam mechanism. Therefore this section derives the classical buckling beam analysis of a double clamped straight beam.

The beam equation describing a straight beam subjected to axial load P is

$$EI \frac{d^4 w}{dx^4} + P \frac{d^2 w}{dx^2} = 0 \quad (2.1)$$

where w is the lateral beam displacement, E is the Young's modulus of the beam material and I the moment of inertia of the beam. With clamped-clamped conditions, the boundary conditions to (2.1) are

$$w(0) = w(l) = 0 \quad (2.2)$$

$$\left(\frac{dw}{dx} \right)_{x=0} = \left(\frac{dw}{dx} \right)_{x=l} = 0 \quad (2.3)$$

Normalize the axial force by

$$N^2 = \frac{Pl^2}{EI} \quad (2.4)$$

Then, (2.1) has the solution

$$w = C_1 \sin\left(N \frac{x}{l}\right) + C_2 \cos\left(N \frac{x}{l}\right) + C_3 x + C_4 \quad (2.5)$$

where $C_1 - C_4$ are constants. Substitute (2.5) into (2.2) and (2.3), in order to have non-zero constants, N must satisfy

$$\sin\left(\frac{N}{2}\right) \left[\tan\left(\frac{N}{2}\right) - \frac{N}{2} \right] = 0 \quad (2.6)$$

which allows two kinds of solution, namely

$$\left. \begin{aligned} w_j(x) &= C \left[1 - \cos\left(N_j \frac{x}{l}\right) \right] \\ N_j &= (j+1)\pi \end{aligned} \right\} j = 1, 3, 5, \dots \quad (2.7)$$

and

$$w_j(x) = C \left[1 - 2\frac{x}{l} - \cos\left(N_j \frac{x}{l}\right) + \frac{2\sin\left(N_j \frac{x}{l}\right)}{N_j} \right] \quad \left. \vphantom{w_j(x)} \right\} j = 2, 4, 6, \dots$$

$$N_j = 2.86\pi, 4.92\pi, \dots \quad (2.8)$$

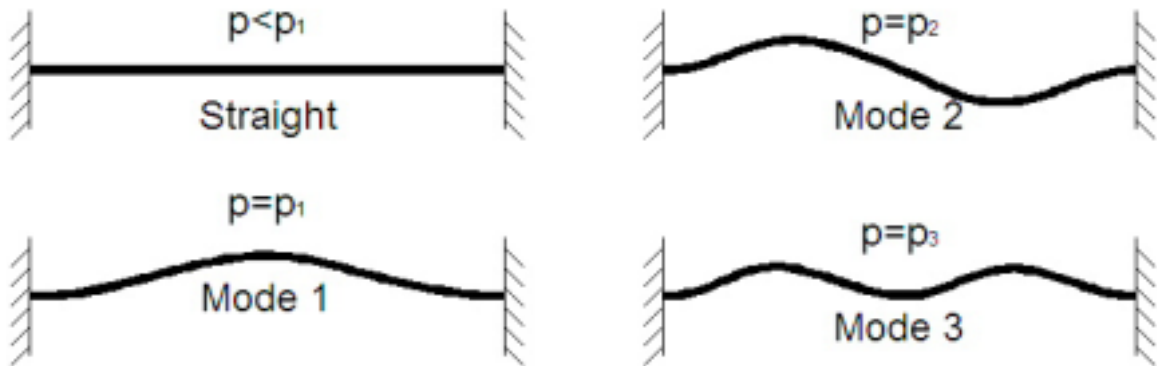


Figure 2-2 Clamped-clamped beam buckling modes

The above analysis gives a mathematical solution to the buckling analysis. The first three modes found from this analysis are shown in Figure 2-2. Stability information of the buckling modes can also be obtained with energy analysis. In short, when a straight beam is only subjected to compression force P , if P is less than P_1 , it is only compressed; if P reaches P_1 , the beam also buckles. The buckling of the first mode would increase the total length of the beam and thus lower the compression force. The amplitude of the buckling would be just enough to keep the axial force at P_1 so the axial force can not exceed P_1 . P can exceed P_1 only when there is lateral force or an applied constraint. For example, if the center of the beam is not allowed to move up and down, then the first buckling mode can not happen, and the compression force can reach P_2 and the second mode can appear. If the center twisting is also not allowed, similarly P can increase to P_3 and the third mode can appear.

A common bistable mechanism involves a pre-stressed straight beam buckled at its first mode [18]. Since buckling can take either an up or down direction, this creates two stable positions of the mechanism. Pre-stress is not easy to obtain and control in MEMS especially in bulk micromachining. A design concept to eliminate the need for pre-stress is to have an as-fabricated curved beam with a first buckling mode shape. The next section models such a structure to see if it is bistable.

2.2.2 Equation formation for curved beam

To analyze the curved beam analytically, consider first the single beam shown in Figure 2-3. It has thickness t , depth b , span l , Young's modulus E and moment of inertia I . Let $w(x)$ denote the distance of the beam from the straight line connecting its two boundaries. The as-fabricated shape of the beam is

$$\bar{w}(x) = \frac{h}{2} \left[1 - \cos \left(2\pi \frac{x}{l} \right) \right] \quad (2.9)$$

where h is the initial apex height of the beam. As can be seen later in the modeling, the geometry constant Q is critical for the behavior of this mechanism, which is defined as

$$Q = \frac{h}{t} \quad (2.10)$$

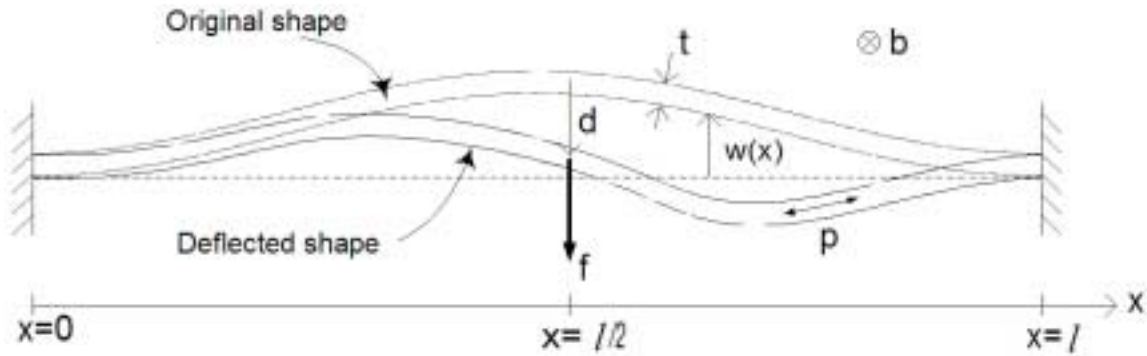


Figure 2-3 Geometry and notation for curved beam deflection analysis

As the lateral force f is applied to the center of the beam at $x = l/2$, the center of the beam deflects by d ,

$$d = \bar{w} \left(\frac{l}{2} \right) - w \left(\frac{l}{2} \right) \quad (2.11)$$

The total length of the beam s changes too,

$$s = \int_0^l \sqrt{1 + \left(\frac{dw}{dx} \right)^2} dx \approx \int_0^l \left[1 + \frac{1}{2} \left(\frac{dw}{dx} \right)^2 \right] dx \quad (2.12)$$

where a small deflection assumption is used. The change of s gives rise to the axial force P by Hooke's law

$$P = Ebt \left(1 - \frac{s}{(s)_{w=\bar{w}}} \right) \quad (2.13)$$

During deflection, define u_b as the beam bending energy, u_s as the beam compression energy, and u_f as the actuation energy. Then the variation of bending energy inside the beam is

$$\partial(u_b) = \partial \left[\frac{EI}{2} \int_0^l \left(\frac{d^2 \bar{w}}{dx^2} - \frac{d^2 w}{dx^2} \right)^2 dx \right] \quad (2.14)$$

The variation of the compression energy is

$$\partial(u_s) = -p \partial(s) \quad (2.15)$$

The variation of the actuation energy is

$$\partial(u_f) = -f \partial(d) \quad (2.16)$$

During deflection, the beam maintains the same clamped-clamped boundary conditions as in (2.2) and (2.3), so its shape can be expressed as a superposition of an infinite set of buckling modes of the straight beam, given by (2.7)(2.8). To simplify this, first normalize the parameters according to

$$X = \frac{x}{l}, W(X) = \frac{w(Xl)}{h} \quad (2.17)$$

Then the superposition of the beam shape is,

$$W(X) = \sum_{j=1}^{\infty} A_j W_j(X) \quad (2.18)$$

where,

$$\left. \begin{aligned} W_j(X) &= 1 - \cos(N_j X) \\ N_j &= (j+1)\pi \end{aligned} \right\} j=1,3,5... \quad (2.19)$$

and,

$$\left. \begin{aligned} W_j(x) &= 1 - 2X - \cos(N_j X) + \frac{2\sin(N_j X)}{N_j} \\ N_j &= 2.86\pi, 4.92\pi... \end{aligned} \right\} j=2,4,6... \quad (2.20)$$

The normalized beam shape as fabricated is

$$\bar{W}(X) = \frac{1}{2} W_1(X) \quad (2.21)$$

Now normalize the applied force f and parameters in (2.11)-(2.16) according to

$$F = \frac{fl^3}{EIh}, \Delta = \frac{d}{h}, S = \frac{sl}{h^2}, N^2 = \frac{pl^2}{EI}, U_b = \frac{u_b l^3}{EIh^2}, U_s = \frac{u_s l^3}{EIh^2}, U_f = \frac{u_f l^3}{EIh^2} \quad (2.22)$$

With the normalization in (2.17) and (2.22), and the mode superposition in (2.18)-(2.21), the relations in (2.11)-(2.16) can now be expressed as,

$$\Delta = 1 - 2 \sum_{j=1,5,9,13\dots} A_j \quad (2.23)$$

$$S = 1 + \sum_{j=1}^{\infty} \frac{A_j^2 N_j^2}{4} \quad (2.24)$$

$$\frac{N^2}{12Q^2} = (S)_{w=\bar{w}} - S = \frac{N_1^2}{16} - \sum_{j=1}^{\infty} \frac{A_j^2 N_j^2}{4} \quad (2.25)$$

$$\partial(U_b) = \partial \left[\frac{\left(\frac{1}{2} - A_1\right)^2 N_1^4}{4} + \sum_{j=2}^{\infty} \frac{A_j^2 N_j^4}{4} \right] \quad (2.26)$$

$$\partial(U_s) = -N^2 \partial(S) = -N^2 \partial \left(\sum_{j=1}^{\infty} \frac{A_j^2 N_j^2}{4} \right) \quad (2.27)$$

$$\partial(U_f) = -F \partial(\Delta) = 2F \sum_{j=1,5,9,13\dots} A_j \quad (2.28)$$

Note that all variables can be expressed in terms of the mode amplitudes without any cross-terms. The variation of the total energy within the mechanism U_t is the sum of (2.26)-(2.28)

$$\begin{aligned} \partial(U_t) &= \partial \left[\left(\frac{N_1^4 (A_1^2 - A_1)}{4} - \frac{N^2 A_1^2 N_1^2}{4} + 2FA_1 \right) + \left(\sum_{j=2}^{\infty} \frac{N_j^4 A_j^2}{4} - \sum_{j=2}^{\infty} \frac{N^2 A_j^2 N_j^2}{4} + 2F \sum_{j=5,9,13\dots} A_j \right) \right] \\ &= \left(\frac{N_1^4 - N^2 N_1^2}{2} A_1 - \frac{N_1^4}{4} + 2F \right) \partial(A_1) + \sum_{j=2,3,4,6,7\dots} \left(\frac{N_j^4 - N^2 N_j^2}{4} \right) \partial(A_j^2) \\ &+ \sum_{j=5,9,13\dots} \left(\frac{N_j^4 - N^2 N_j^2}{2} A_j + 2F \right) \partial(A_j) \end{aligned} \quad (2.29)$$

The mode amplitudes should minimize U_t , thus

$$\partial(U_t) \geq 0 \quad (2.30)$$

In order to satisfy (2.30), the coefficients of the $\partial(A_j)$, $j=1,5,9,13\dots$ terms in (2.29) should be zero, which yields

$$A_1 = -\frac{1}{2} \frac{N_1^2}{N^2 - N_1^2} + \frac{4F}{N_1^2 (N^2 - N_1^2)} \quad (2.31)$$

$$A_j = \frac{4F}{N_j^2(N^2 - N_j^2)}, \quad j=5,9,13\dots \quad (2.32)$$

The $\partial(A_j^2)$, $j=2,3,4,6,7\dots$ terms in (2.29) must also satisfy (2.30), which leads to the following conclusions. First, if its coefficient is positive, A_j^2 must be zero to satisfy (2.30), in which case any variation of A_j^2 is positive. Second, if its coefficients is negative, A_j^2 must have been constrained to satisfy (2.30), since any positive variance of A_j^2 can invalidate (2.30). So in short,

$$A_j \begin{cases} = 0, & N^2 < N_j^2 \\ \text{must have been constrained,} & N^2 > N_j^2 \\ \text{can take any value as long as} & N^2 = N_j^2 \end{cases} \quad j=2,3,4,6,7\dots \quad (2.33)$$

For practical reasons, only the second mode can be easily constrained mechanically without affecting the first mode, so the second condition of (2.33) dictates that j can only take the value of 2 when the second mode is not constrained, or 3 when the second mode is constrained.

Equation (2.33) permits three kinds of solutions. The first kind is

$$\begin{cases} F = F_1 \\ N^2 < \begin{cases} N_1^2, & \text{with second mode constrained} \\ N_2^2, & \text{with second mode not constrained} \end{cases} \\ A_j = 0, \quad j \neq 1,5,9,13\dots \end{cases} \quad (2.34)$$

the second kind is

$$\begin{cases} F = F_2 \\ N^2 = N_2^2 \\ A_j = 0, \quad j \neq 1,2,5,9,13\dots \end{cases} \quad (2.35)$$

and the third kind is

$$\begin{cases} F = F_3 \\ N^2 = N_3^2 \\ A_j = 0, \quad j \neq 1,3,5,9,13\dots \end{cases} \quad (2.36)$$

Equations (2.23),(2.25),(2.31),(2.32),(2.34),(2.35) and (2.36) define the $F - \Delta$ relation of the curved beam. Neglecting the higher modes in (2.32), closed form solutions can be obtained. Keeping those modes, however, gives a better result. Both solutions are discussed and compared hereafter.

2.2.3 Solution with higher mode neglected

The denominator of (2.32) is orders of magnitude larger than in (2.31), so for simplicity, all these higher order terms are neglected in this solution,

$$A_j = 0, \quad j=5,9,13\dots \quad (2.37)$$

From (2.23), (2.31), (2.34), and (2.37), the first kind of solution is

$$\begin{aligned} F_1 &= N_1^4 Q^2 \left[\frac{3}{32} \Delta^3 - \frac{9}{32} \Delta^2 + \left(\frac{3}{16} + \frac{1}{8Q^2} \right) \Delta \right] = \frac{3\pi^4 Q^2}{2} \left[\Delta^3 - 3\Delta^2 + \left(2 + \frac{4}{3Q^2} \right) \Delta \right] \\ &= \frac{3\pi^4 Q^2}{2} \left[(\Delta - 2)^3 + 3(\Delta - 2)^2 + \left(2 + \frac{4}{3Q^2} \right) (\Delta - 2) + \frac{8}{3Q^2} \right] \\ &= \frac{3\pi^4 Q^2}{2} \Delta \left[(\Delta - 1)(\Delta - 2) + \frac{4}{3Q^2} \right] \\ &= \frac{3\pi^4 Q^2}{2} \Delta \left(\Delta - \frac{3}{2} + \sqrt{\frac{1}{4} - \frac{4}{3Q^2}} \right) \left(\Delta - \frac{3}{2} - \sqrt{\frac{1}{4} - \frac{4}{3Q^2}} \right) \end{aligned} \quad (2.38)$$

In (2.38), F_1 is expressed in various ways, so the values and derivatives at several critical points can be quickly obtained. From (2.25)(2.31)(2.34), the normalized axial force when the curved beam at either stable position is

$$\left(N^2 \right)_{F_1=0} = 0, \text{ or } N_1^2 \left[1 + \frac{3Q^2}{8} \left(1 - \sqrt{1 - \frac{16}{3Q^2}} \right) \right] \quad (2.39)$$

From (2.23)(2.25)(2.31)(2.35),

$$F_2 = \frac{N_1^2 (N_2^2 - N_1^2)}{8} \left(\frac{N_2^2}{N_2^2 - N_1^2} - \Delta \right) = 4.18\pi^4 - 2.18\pi^4 \Delta \quad (2.40)$$

which exists if (1) the second mode is not constrained and (2), by (2.25), (2.31), and (2.35),

$$Q > \frac{2N_2}{\sqrt{3}N_1} = 1.67$$

From (2.23)(2.25)(2.31)(2.36),

$$F_3 = \frac{N_1^2 (N_3^2 - N_1^2)}{8} \left(\frac{N_3^2}{N_3^2 - N_1^2} - \Delta \right) = 8\pi^4 - 6\pi^4 \Delta \quad (2.41)$$

which exists if (1) the second mode is constrained and (2), by (2.25), (2.31), and (2.36),

$$Q > \frac{2N_3}{\sqrt{3}N_1} = 2.31$$

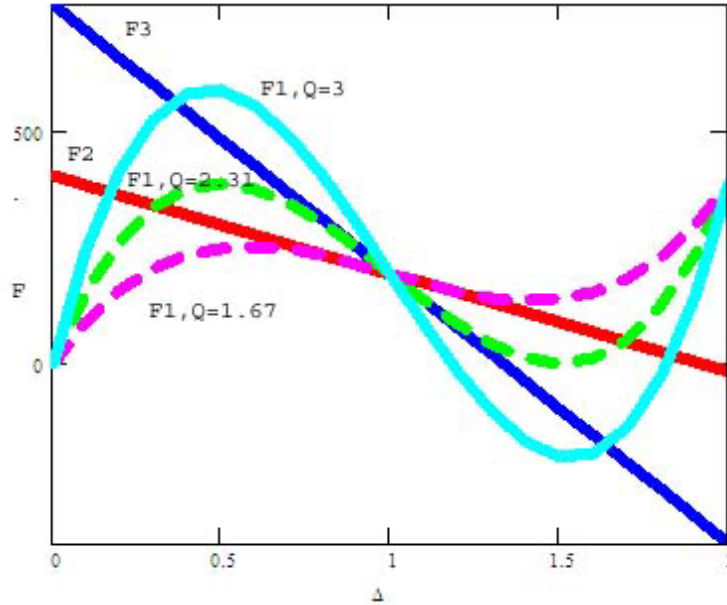


Figure 2-4 F- Δ relations of curved beam

The $F_1, F_2, F_3 - \Delta$ relations are shown in Figure 2-4, all of which are extrapolated to the whole range of $\Delta = 0$ to 2. F_2 and F_3 are straight lines with a negative slope that do not depend on Q . F_3 can exist only if mode 2 is constrained. F_1 depends on Q , but its values at $\Delta = 0, 1, 2$ are constants. Moreover, at $\Delta = 1$, F_1 , F_2 and F_3 pass through the same point. The higher the Q , the higher the curving of F_1 . With $Q = 1.67$, F_1 becomes tangential with F_2 at $\Delta = 1$. With $Q = 2.31$, F_1 becomes tangential with F_3 at $\Delta = 1$. When Q is larger than those tangential values, curve F_1 has two more intersections with either F_2 or F_3 besides $\Delta = 1$. These two additional intersections are where the axial force equals that of the second mode or the third mode. Between these two intersections, either F_2 or F_3 exists, while outside this interior range of Δ , only F_1 exists. The actual $F - \Delta$ curve is therefore a hybrid curve that switches between the F_1 curve and either the F_2 or F_3 curve at these two intersections.

The F_2 line is always above zero force except for its small negative value before $\Delta = 2$, which means that with the second mode free, even with a very high Q the curved beam can be at most marginally bistable. On the other hand, the F_3 curve has a large portion below zero force. With the second mode constrained, the curved beam is bistable with $Q > 2.31$.

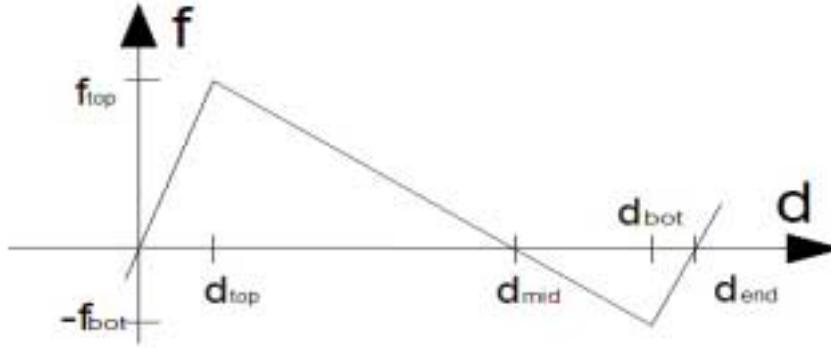


Figure 2-5 f-d curve for a second-mode-constrained curved beam when $Q \gg 1$

With high Q , the $F - \Delta$ curve takes the shape of three straight lines. Dimensionalizing the curves shown in Figure 2-4 according to (2.22), the force-displacement curve of a curved beam with the second mode constrained can be shown in Figure 2-5. For $Q \geq 6$, the approximate values in Figure 2-5 are

$$f_{top} \approx 8\pi^4 \frac{EIh}{l^3}, f_{bot} \approx 4\pi^4 \frac{EIh}{l^3}, d_{mid} = 1.33 h \quad (2.42)$$

$$d_{top} \approx \frac{8t}{3Q}, d_{bot} \approx 2h - \frac{8t}{3Q}, d_{end} \approx 2h - \frac{4t}{3Q} \quad (2.43)$$

where (2.42) is derived from (2.41), and (2.43) is derived from (2.38) and (2.42). Due to the absence of higher mode terms in (2.32), both (2.42) and (2.43) are only approximate. Moreover, (2.43) does not give the correct scaling due to the simplification. The next section describes the solution with higher modes included, which gives exact expressions for the values shown in Figure 2-5.

2.2.4 Solution with higher modes included

Keeping all the higher order terms as (2.32), or at least the first two or three terms, would give more accurate stiffness prediction than neglecting them.

From (2.23), (2.25), (2.31), (2.32), and (2.34), the first kind of solution should satisfy,

$$\sum_{j=1,5,9,13,\dots} \frac{4(N^2 - N_1^2)^2}{N_j^2 (N^2 - N_j^2)^2} F_1^2 - N_1^2 F_1 + \frac{N^2 (N^2 - N_1^2)^2}{12Q^2} - \frac{N_1^2 N^2 (N^2 - 2N_1^2)}{16} = 0 \quad (2.44)$$

(2.44) can be used to determine F_1 from N^2 . Following this, (2.23), (2.31) and (2.32) can be used to determine the beam shape and hence Δ from F_1 .

From (2.23)(2.25)(2.31)(2.32)(2.35), the second kind of solution is

$$F_2 = \frac{1}{\sum_{j=1,5,9,13\dots} \frac{8}{N_j^2 (N_2^2 - N_j^2)}} \left(\frac{N_2^2}{N_2^2 - N_1^2} - \Delta \right) \quad (2.45)$$

From (2.23)(2.25)(2.31)(2.32)(2.36), the third kind of solution is

$$F_3 = \frac{1}{\sum_{j=1,5,9,13\dots} \frac{8}{N_j^2 (N_3^2 - N_j^2)}} \left(\frac{N_3^2}{N_3^2 - N_1^2} - \Delta \right) \quad (2.46)$$

Similar curves to those shown in Figure 2-4 can be obtained. With high Q , the $F - \Delta$ curve again takes the shape of three straight lines. The resulting force-displacement curve of a curved beam with the second mode constrained with $Q \geq 6$ can still be shown with Figure 2-5, but with different values than given by (2.42)(2.43):

$$f_{top} \approx 740 \frac{EIh}{l^3}, \quad f_{bot} \approx 370 \frac{EIh}{l^3}, \quad d_{mid} = 1.33 h \quad (2.47)$$

$$d_{top} \approx 0.16h, \quad d_{bot} \approx 1.92h, \quad d_{end} \approx 1.99h \quad (2.48)$$

2.2.5 Comparison of the solutions and FEA

Nonlinear finite element analysis (FEA) by Algor was performed. The solution neglecting higher modes (2.42)(2.43), the solution including higher modes (2.47)(2.48), and the FEA results are shown in Figure 2-6 for a second-mode-constrained curved beam $3mm$ long, $6\mu m$ thick, $60\mu m$ apex height, $490\mu m$ depth, and $169Pa$ of Young's modulus. As can be seen, the solution neglecting higher modes predicts a stiffer curve near both stable positions, while the solution including higher modes agrees very well with FEA.

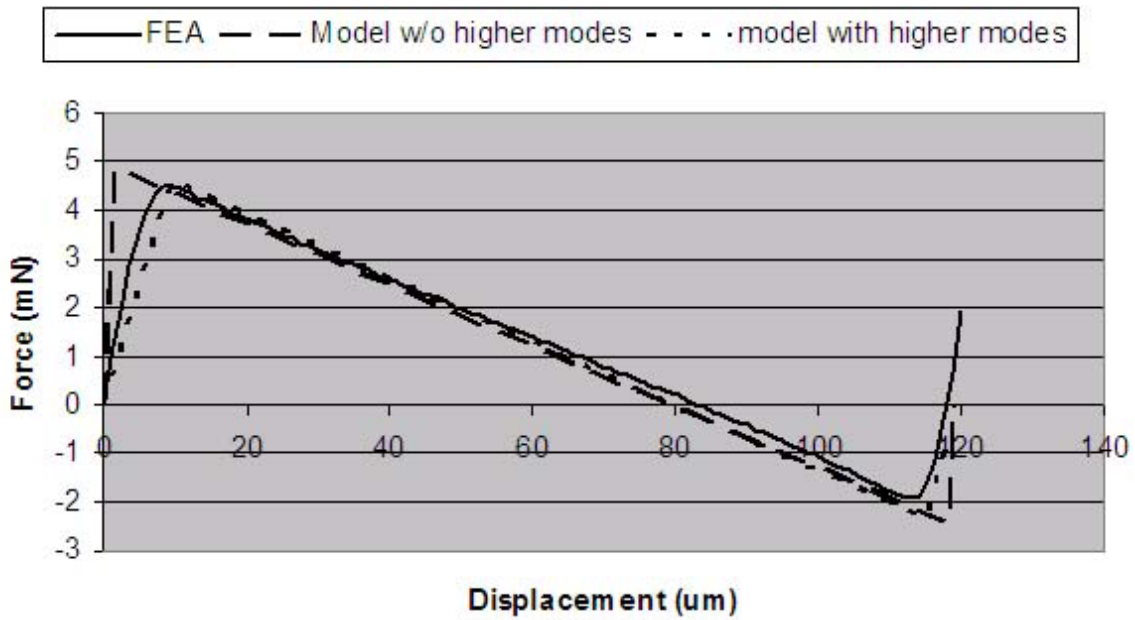
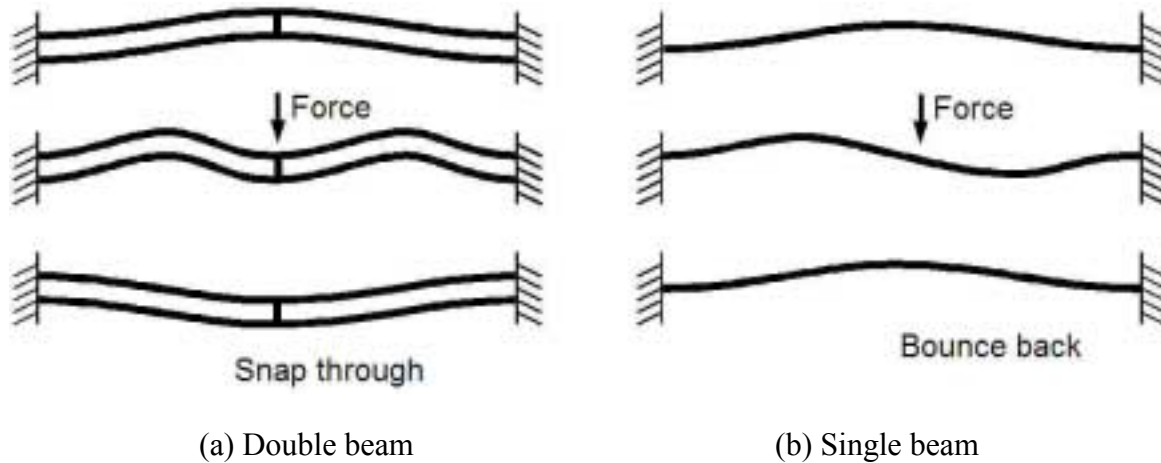


Figure 2-6 Comparison of theoretical models and FEA for curved beam

2.3 Design of curved beam bistable mechanism



(a) Double beam

(b) Single beam

Figure 2-7 Double curved beam versus single curved beam

Structural energy inside the curved beam during deflection comprises both bending energy and compression energy. Qualitatively from an energy viewpoint, the bending energy in the beam increases monotonically whenever the beam is moving downward; while the compression energy increases to maximum approximately at the centerline, but then decreases after crossing the line. If the beam is designed so that the decrease of compression energy after crossing the centerline is faster than the increase of the bending energy, then a negative force results, which is an indication of bistability.

Based on the last section, a curved beam is bistable if two conditions hold: (1) Q has to be large enough, and (2) the second mode must be constrained. The first condition is easy to satisfy in DRIE etch since the shape of the beam is only defined by the etching mask. To satisfy the second condition, one method is to have a center plunger attached to a single curved beam, and this plunger is guided in an open slot to prevent it from twisting much. Another more effective method is to clamp two curved beams together at the center [18] to have a double beam structure. The center clamp transfers the rotational motion of either beam center to the axial translational motion of the other beam. Since the beams are stiff at the axial direction, the rotational motion of both beams can be effectively reduced. The longer the center clamp or the gap between the two beams, the more the second mode can be overcome. With a gap five times larger than the beam thickness, both FEA and micro fabricated beams show a visible second mode during the transition, while the f-d curve is still very close to the behavior of a curved beam with the second mode completely constrained. Note that the twisting is only present during the negative stiffness region; at the region close to the two stable positions, the beams move straight even if the center clamp is not long. The bistable double beam mechanism is shown in Figure 2-7 (a), while the monostable single beam mechanism is shown in Figure 2-7 (b).

The force-displacement curve of a double beam would just look like what is shown in Figure 2-5, with the displacement values equal to, but the force values doubled from, what are given in (2.47)(2.48). Thus,

$$f_{dbtop} \approx 1480 \frac{EIh}{l^3}, f_{dbbot} \approx 740 \frac{EIh}{l^3} \quad (2.49)$$

In designing a curved beam bistable mechanism to provide a certain force, the maximum strain during deflection should be within the yield strain of DRIE etched silicon structure. The maximum strain during deflection can be estimated as

$$\varepsilon_{\max} \approx 2\pi^2 \frac{th}{l^2} + 4\pi^2 \frac{t^2}{3l^2} = \pi^2 \frac{th}{l^2} \left(2 + \frac{4}{3Q} \right) \approx 2\pi^2 \frac{th}{l^2} \quad (2.50)$$

From (2.49)(2.50),

$$l = \frac{6.31Qf_{dbbot}}{\varepsilon_{\max}^2 Eb} \quad (2.51)$$

which shows that with a certain force requirement, the length is inversely proportional to the strain square. A smaller design requires higher fracture strength.

The design requirements of the relay as given in Table 1-2, the design for fabrication guidelines given in Table 5-1, and equations (2.48) and (2.49) together determine the design of bistable double beam to be used in the relay. Table 2-1 shows such a design for the relay.

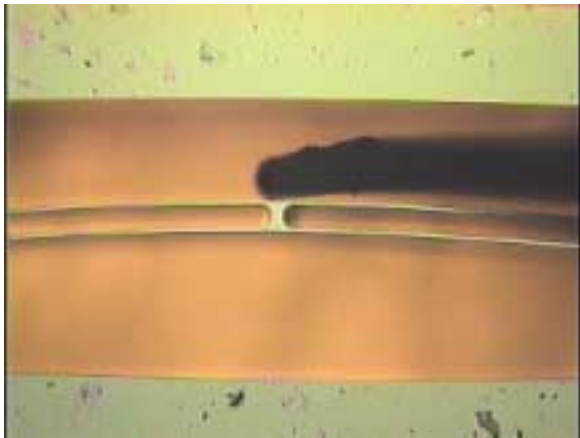
Table 2-1 A design of bistable double beam for the relay

Dimensions	$t = 12\mu\text{m}, h = 72\mu\text{m}, l = 4\text{mm}, b = 0.3\text{mm}, (E = 169\text{Pa})$
------------	--

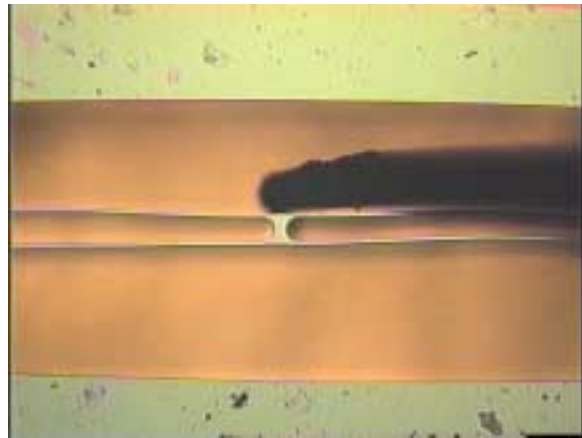
Characteristics	$f_{dbtop} = 11.3mN, f_{dbbot} = 5.7mN,$ $d_{top} = 12\mu m, d_{mid} = 96\mu m, d_{bot} = 135\mu m, d_{end} = 141\mu m$
-----------------	--

2.4 Fabrication and testing of curved beam mechanism

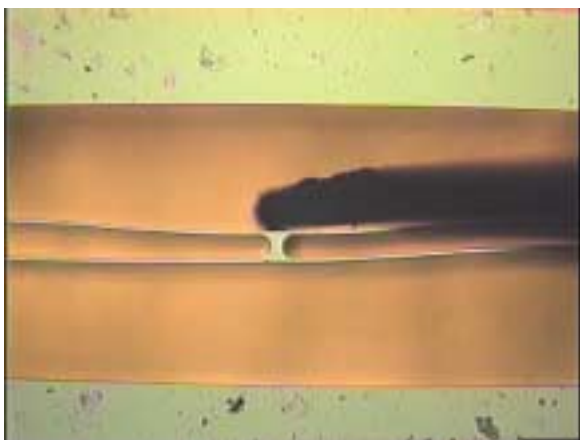
Micro-scale double beam mechanisms designed by the previous section have been fabricated and successfully tested. The mechanism described below has been designed with a span of $l = 3mm$, a thickness of $t = 10\mu m$, a depth of $b = 490\mu m$ and an initial apex height of $h = 60\mu m$. The estimated maximum strain within the mechanism during snap through is 0.16%.



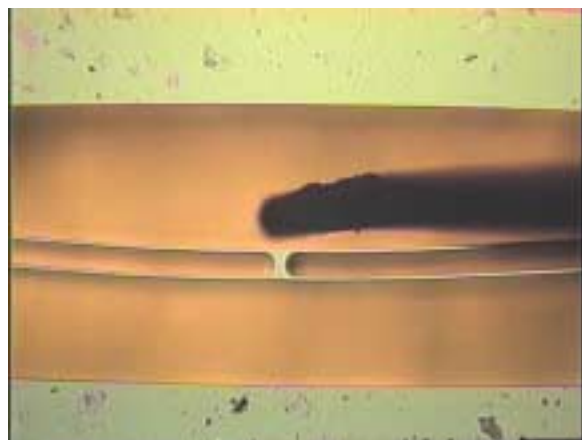
(a) Probe touches



(b) Deflects



(c) Deflects more



(d) After snap

Figure 2-8 The bistable mechanism as pushed manually by a probe

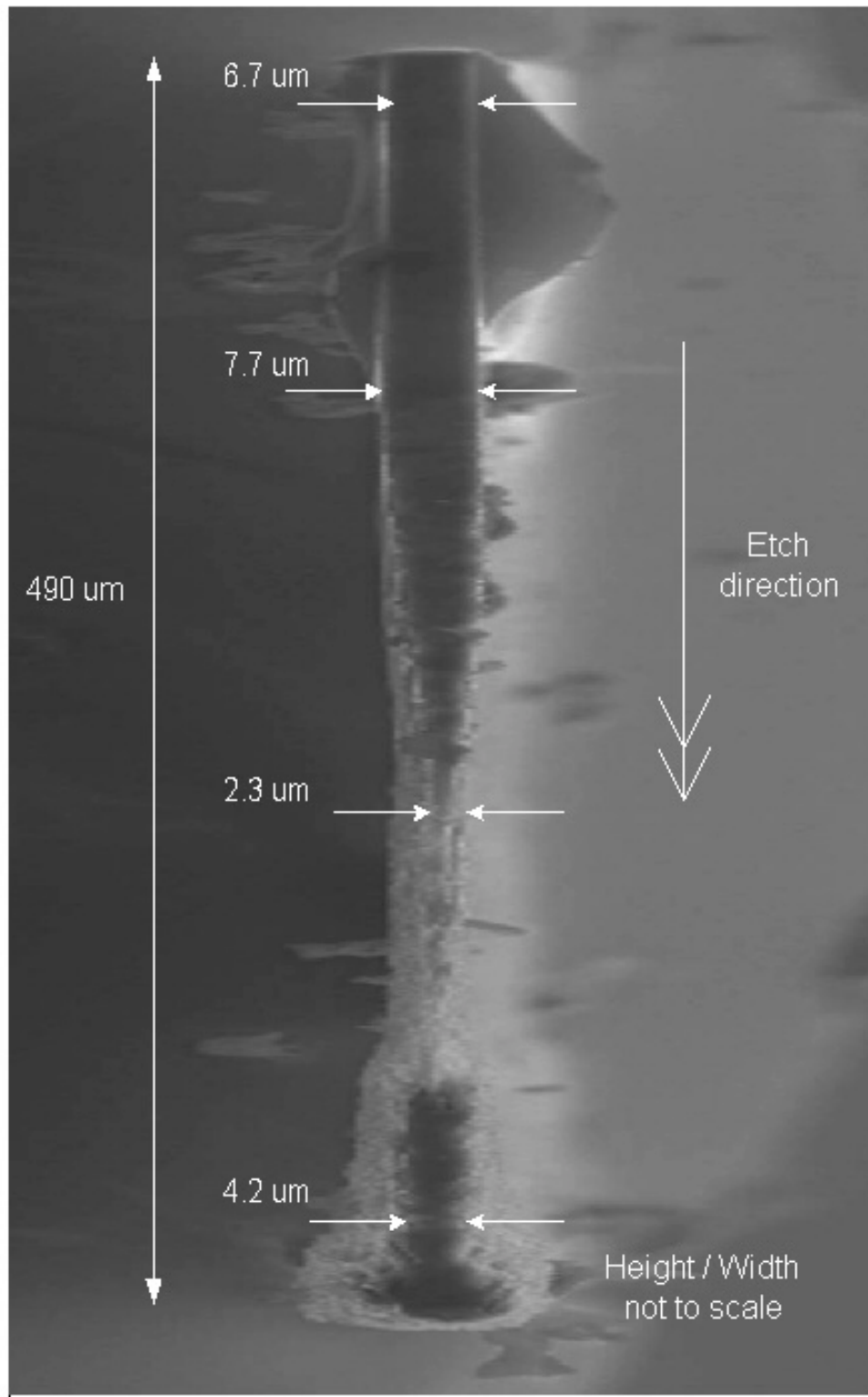


Figure 2-9 SEM of a beam fabricated with DRIE

The experimental mechanism is etched on a (100), double side polished silicon wafer. The orientation of the bistable beams is parallel to the primary flat. In this direction, according to the data provided in [24], the beams have a Young's modulus of 168.9 GPa. Fillets were added in the etch mask at the sharp corners to lower the stress concentration. Further, halos were included in the mask, so that the etch space has the same 20 μm width throughout the mask. This arrangement helps to ensure that etching occurs at the same rate at all locations. The etch mask itself comprised a 0.75 μm oxide hard mask, and a 15 μm photoresist soft mask. The etch recipe "MIT69A" was used as developed in the Microsystems Technology Laboratories of MIT. The total time taken to etch through the whole wafer thickness of 490 μm was about 4.5 hours. To help smooth out the sidewall surface roughness created during DRIE, a dry isotropic etch using SF₄ for 15 seconds follows the through-etch. This technique can increase the fracture stress of a DRIE structure [25].

A micro probe was used to push the experimental mechanism down and up at its center. The two stable positions of the mechanism, together with two middle positions while being pushed down are shown in Figure 2-8; only the center portion of the mechanism is shown.

The characteristic parameters of the bistability curves are determined by the etched beam geometry and the Young's modulus of the wafer. Therefore they can be significantly affected by fabrication variation especially by variation of the beam thickness. The actual beam thickness after fabrication is significantly less than the designed 10 μm , as shown in the Scanning Electron Microscope (SEM) picture in Figure 2-9. As it can be seen, the cross sectional thickness varies between 2.3 and 7.7 microns. Note also the eroded structure at the bottom. The reduction of the fabricated beam thickness versus the designed value results mainly from the loss of mask coverage during the etch process. Due to the long etching time for through-etch; a relatively thick mask resist layer is required. Such a thick resist layer shows slanted sidewalls after exposure and development. During DRIE, the resist is continuously etched away not only from the top surface but also from the sidewalls, which exposes regions on the wafer that are supposed to be protected, hence the reduction in beam thickness. The thickness variation along the wafer depth is fairly large due to the phenomenon that the DRIE process produces non-ideally etched sidewalls. Careful tuning of the machine parameters can result in almost straight side walls for a particular process, but after days or weeks during which the condition of the machine changes, the etched side wall would become non-ideal again even with the same recipe.

To measure the force-deflection characteristics of the experimental bistable mechanisms, a specialized MEMS flextester [26][33] was developed, as shown in Figure 2-10. The tester features a resolution of 10 nm for the displacement, and 100 μN for the force. A total of twenty force-displacement measurements were performed on ten bistable mechanisms with the same design geometry at different locations on the same wafer. For each measurement, the bistable mechanism has to be touched from both sides, since at the snap through point, it moves away from the probe tip. The overall force-displacement curve is found by "stitching" the two graphs together.

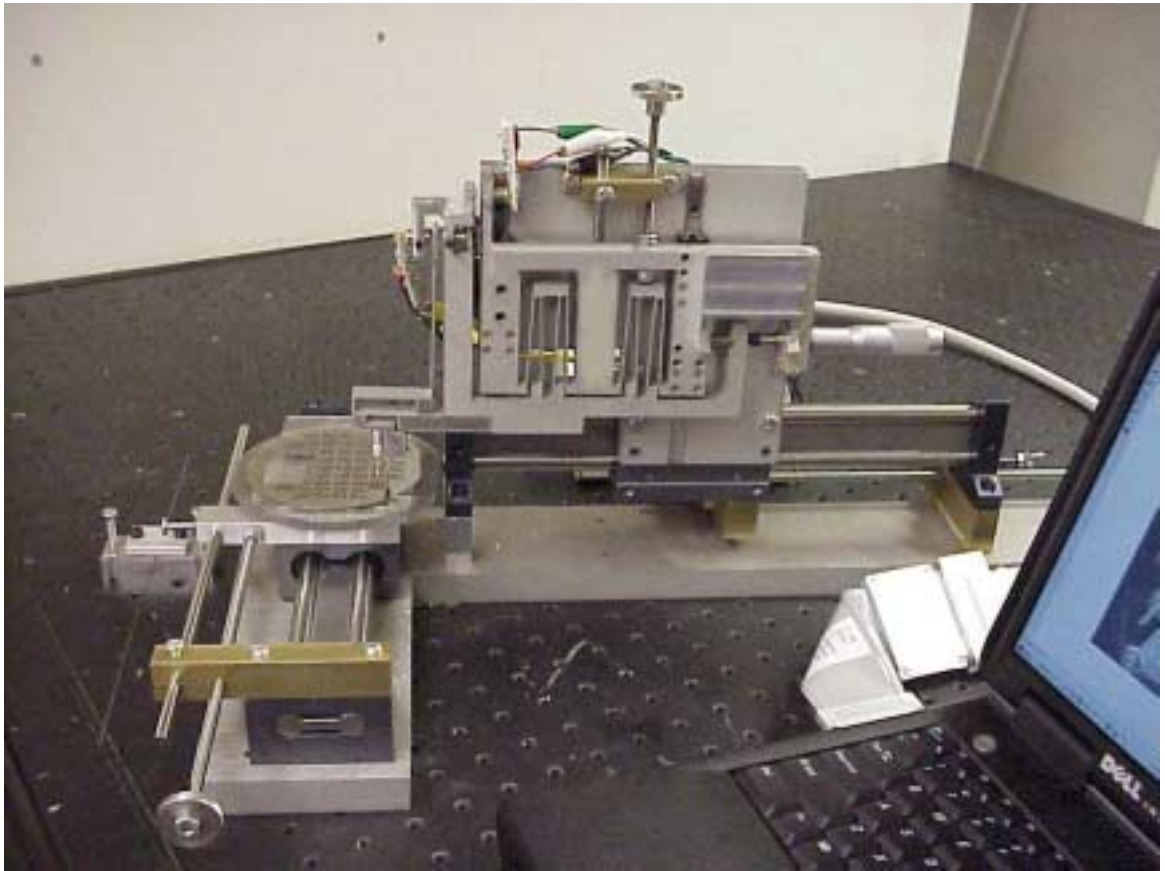


Figure 2-10 Flextester for measuring MEMS force-displacement curve

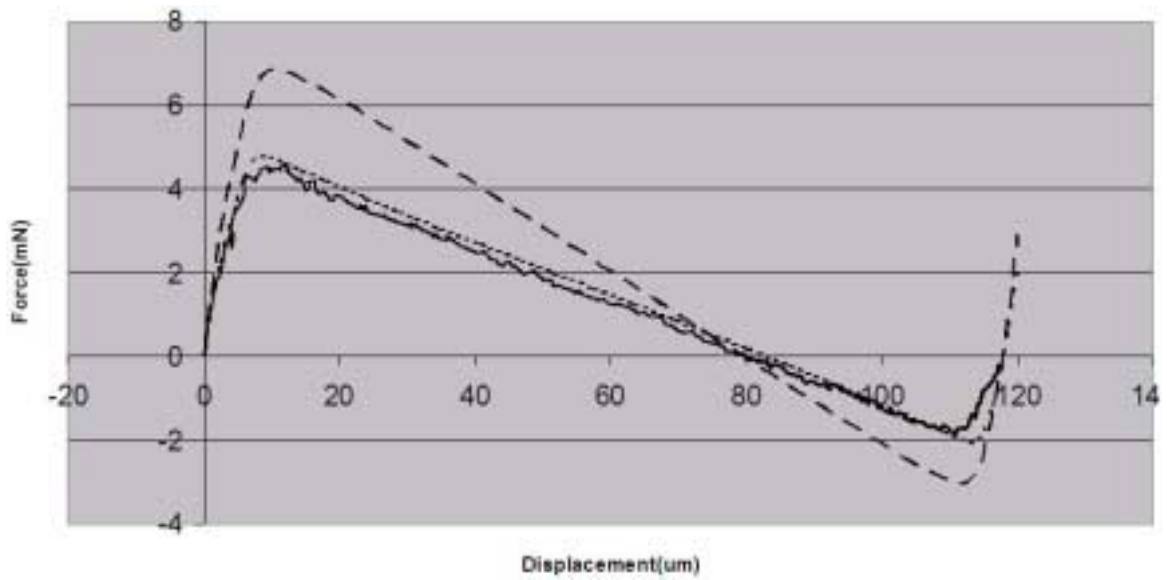


Figure 2-11 Comparison of f-d curve from theory, FEA and measurement.

The behavior of the bistable mechanism, whose dimensions were described in the beginning of this section, is measured and predicted by 2D FEA, as shown in Figure 2-11. The solid curve is one of the measurement result, while the dashed and dotted curves are FEA results for beam thickness of 6.7 μm and 6 μm , which are the top thickness and cubic average thickness of the fabricated beam shown in Figure 2-9 respectively. Note that the top thickness of the beam could be measured by a microscope with a scale, but a detailed knowledge of the beam thickness variation along the depth could only be obtained destructively. It can be seen that the measured curve suggests less force than the FEA prediction for 6.7 μm thick beams, but it is very close to the prediction for 6 μm thick beams.

2.5 Optimization of curved beam mechanism

2.5.1 Optimization of the force-displacement curve symmetry

The basic double beam design has an asymmetric force-displacement curve, as shown in Figure 2-5. In some applications, a more symmetric f-d curve is desired. Define the asymmetry factor as:

$$r = \frac{f_{top}}{f_{bottom}} \quad (2.52)$$

then (2.42) gives $r = 2$. Note that if we define the asymmetric factor as the ratio of the length of the positive force region and the negative force region, it gives almost the same numerical value. Two approaches have been explored to optimize the double beam mechanism so r could be closer to unity. The first approach is to optimize the initial shape of the mechanism; the second approach is to modulate the beam thickness.

Both analytic and FEA work were done to find an initial shape including some higher buckling mode that can give a reduced asymmetry factor, but no improvement has been found. The first mode as the initial shape gives the best symmetry. A brief insight as to why modes 5,9,13... do not help can be obtained by examining the role of those modes in the beam behavior. Equation (2.32) states that since $N_{5,9,13...}^2 \gg N_1^2$, $A_{5,9,13...} \ll A_1$. But if we have some higher mode amplitude $\bar{A}_{5,9,13...}$ in the initial shape, instead of (2.32), the expression for $A_{5,9,13...}$ will be similar to (2.31) as

$$A_{5,9,13...} = -\bar{A}_{5,9,13...} \frac{N_{5,9,13...}^2}{N^2 - N_{5,9,13...}^2} + \frac{4F}{N_{5,9,13...}^2 (N^2 - N_{5,9,13...}^2)} \quad (2.53)$$

In this case, due to the first term in (2.53), $A_{5,9,13...}$ would be larger during the beam deflection than without any initial higher mode. This enhancement of mode 5,9,13... components, according to (2.25), would lower the changing rate of N^2 , and compression energy that is the key factor to make the structure bistable, so the snap-through is less likely to happen and bistability is lost or reduced.

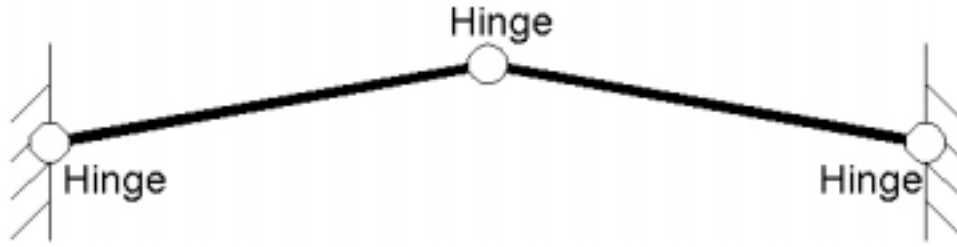


Figure 2-12 A three-hinge bistable mechanism

Another approach involves the modulation of beam thickness. Initial insight into the way to optimize comes again from the model analysis. For the curved beam, the bending energy increases monotonically during the beam deflection, while the compression energy first increases than decreases during the snap-through. It is the dominance of the change of the compression energy over the bending energy that gives bistability, thus a beam shape that minimizes the bending energy change relative to the compression energy change during the beam deflection can help enhance the bistability. The predominant mode in the double-beam deflection is the first mode, which has maximum bending stress near the two boundary clamp sites and the center clamp site. Thus if the thickness at these three locations is decreased, the bending effect is significantly lowered. Another view of this design is to consider the three-hinge bistable structure shown in Figure 2-12. Due to the perfect symmetry of the structure at the up and down position, the asymmetric factor r is unity. However, it is not easy to implement a perfect hinge (zero friction, zero clearance, and zero stiffness) in MEMS fabrications, especially in bulk micro machining. An approximate structure is to use thin section of a beam, which again leads to a thin-thick-thin-thick-thin thickness design. To avoid dramatic thickness change, a cosine modulation of the thickness is adopted as shown in Figure 2-13

$$t(x) = t_a \left[1 - \frac{\beta - 1}{\beta + 1} \cos\left(4\pi \frac{x}{l}\right) \right] \quad (2.54)$$

where t_a is the average thickness of the modulated beam, and β is the ratio of the largest thickness and the smallest thickness.



Figure 2-13 Curved beam with cosine thickness modulation

An FEA study was performed on the thickness modulation. As shown in Figure 2-14, eight independent curved beams with different shape and constraint are subjected to center displacement load indicated by arrows. They are all clamped, indicated by triangles, on both ends. Beam 1,2,3,4 also have the center rotation constrained, indicated as a circles, so their second modes are constrained. All beams have 3mm length and $60\mu\text{m}$ initial apex height. Beams 4 and 8 have uniform thickness of $10\mu\text{m}$. The thickness of beams 1,2,3,5,6,7 are

modulated by a cosine function as in (2.54) so they all have thin-thick-thin-thin-thin thickness variations. The average beam thicknesses are still $t_a = 10\mu m$, while the amplitude of the thickness variation is $\beta = 3(t_{\min} = 5\mu m, t_{\max} = 15\mu m)$. Though beams 1,2,3,5,6,7 have the same thickness profile, they are modulated differently: Beams 3 and 7 only have the bottom edge modulated; Beams 1 and 5 only have the top edge modulated; Beams 2 and 6 have both the top and the bottom edges modulated.

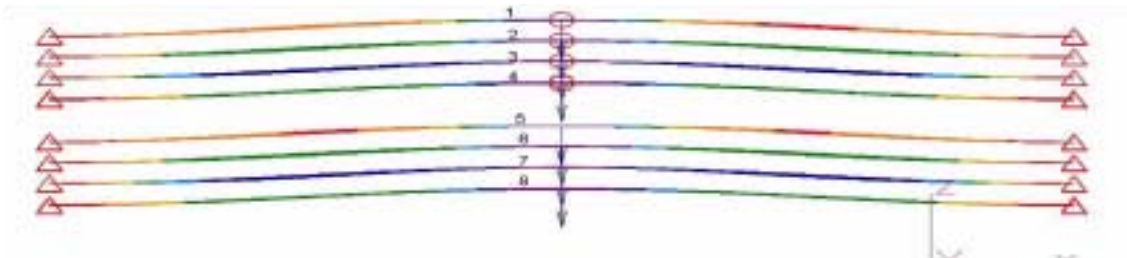
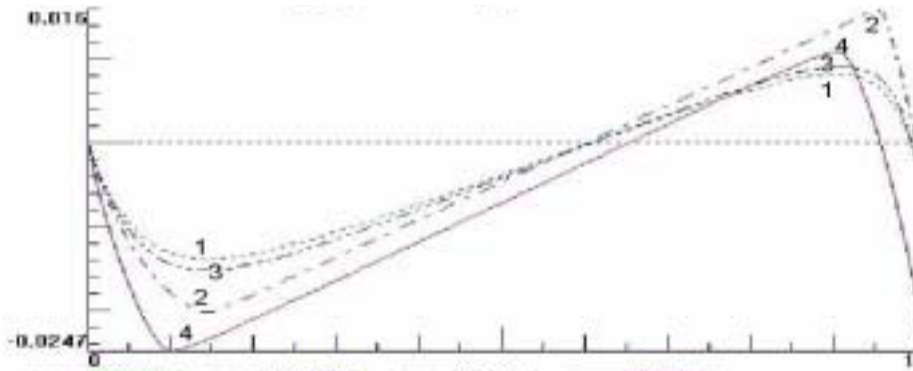
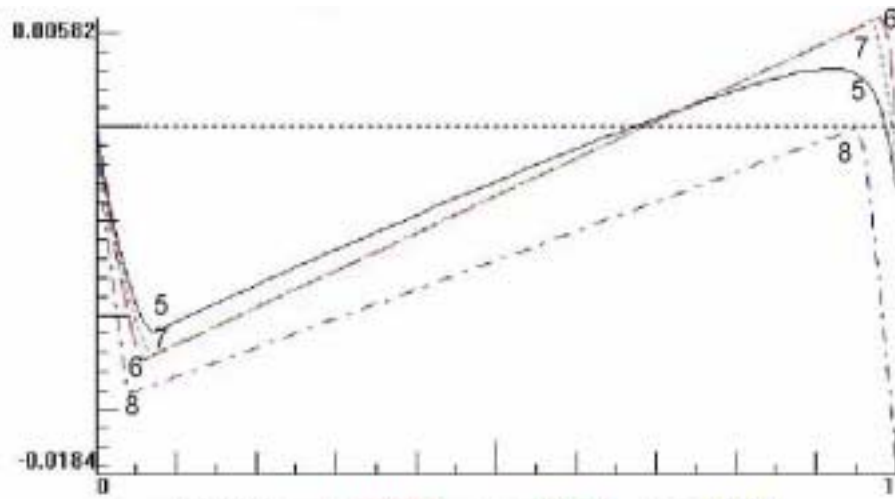


Figure 2-14 FEA study of cosine thickness modulated beams



(a)



(b)

Figure 2-15 f-d curve by FEA for the cosine thickness modulated beam mechanisms

The FEA force-displacement curves for the mechanisms shown in Figure 2-14 are shown in Figure 2-15 (a) for the second-mode-constrained beams, and in Figure 2-15 (b) for the second-mode-free beams, where the x axis is center displacement divided by $120\mu\text{m}$ and the y axis is force in unit of N. It was found that this design does move the asymmetric factor closer to unity. Moreover, it makes the second-mode-free curved beam bistable. Among the three beam thickness modulations, with both the top and bottom edge are modulated, the optimization result is the best as shown by curve 2 and 6 in Figure 2-15. The FEA study also shows that such modulated beams have more stress than the basic double beam, with the maximum stress occurring at the thin beam sections. The maximum stress is usually two or three times higher than in a uniform-thickness double beam. Table 2-2 summarizes the results for beam 2, 6. To lower the value of r , higher values of β can be used.

Table 2-2 Thickness modulation optimized results

Center condition	β	r
Constrained	3	1.25
Free	3	2.5

The thin-thick-thin-thick-thin thickness modulation concept was documented in the feasibility study report [21] of this thesis, while the FEA study was carried out shortly after. The method was discussed and more research was continued in [23] with an analytical approach, where a more sophisticated modulation pattern was found.

2.5.2 Optimization of the force-displacement curve stiffness

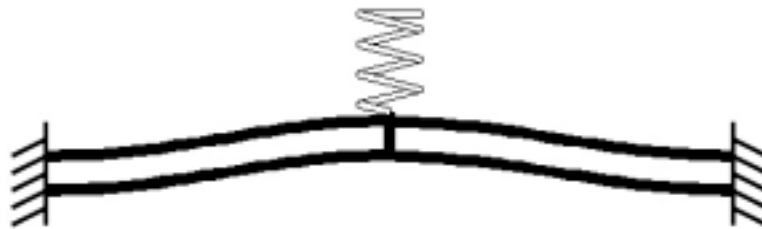


Figure 2-16 Double beam with softspring

The curved beam bistable mechanism has an f-d curve in which the maximum force occurs very close to the initial position, and then decreases. This property is not good for some actuators especially electrostatic actuators, whose actuation force starts low and then increases as the two electrodes get closer. A bistable f-d curve with a gentler ramping up of force may be needed for other reasons too. One way to modify this is to include a soft spring with the curved beam structure as shown in Figure 2-16. The spring can be linear or nonlinear, and correspondingly, the f-d curved could be modified in various ways. This concept is also used in the design of relay contacts, as shown later in Figure 4-2.

Chapter 3

ACTUATORS

Though some modeling was carried out in [21] for actuation of the double beam by an off-center force, or by a distributed force applied on the whole double beam body, the easiest actuation is by a force applied at the beam center. The bistable double beam shown in Table 2-1 requires an actuation of more than $10mN$ of maximum force and more than $100\mu m$ of stroke. To meet these requirements, a variety of actuation methods have been explored, which include magnetic actuator, electrostatic comb drive type actuator, electrostatic zipper actuator, and electrothermal actuators. The performance and fabrication challenges of each type of actuator are compared, and electrothermal actuator is selected to pursue due to its high performance and easy fabrication. The main disadvantage of electrothermal actuation is its high power consumption, which is less serious due to the bistability of this relay.

Section 3.1 describes the design and modeling of electrothermal actuator. Section 3.2.1 describes the feasibility study for electrostatic comb drive type actuators. Section 3.2.2 describes the preliminary study on electrostatic zipper actuators.

3.1 Electrothermal actuator

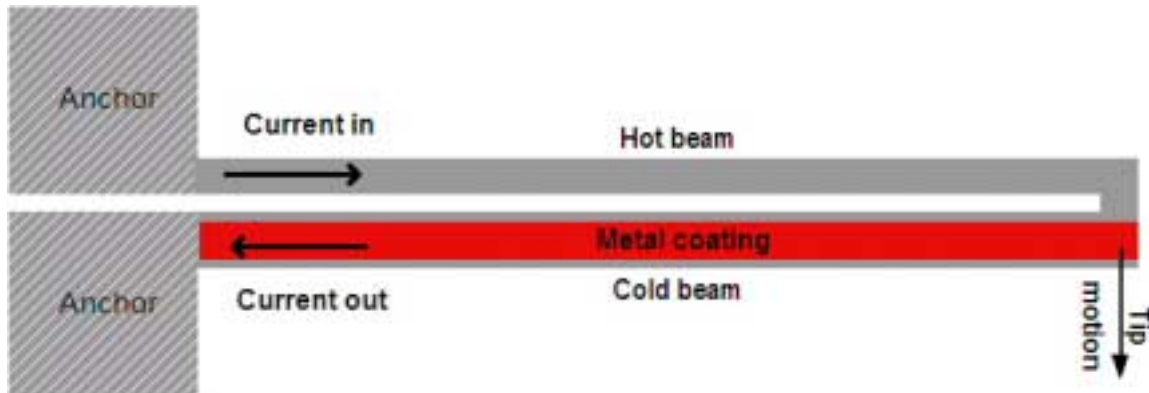


Figure 3-1 Schematic of the electrothermal actuator

Electrothermal actuators are commonly used in MEMS [27][28][29]. Figure 3-1 shows the schematic of the thermal actuator developed in this thesis. Two beams are mechanically anchored at one end, and joined together at the other end. One beam is coated with metal while the other is not, so a current going through the beams would generate heat on the bare silicon beam while the coated one is kept cold due to the high metal conductance. The hot beam thermally expands, but due to the constraint of the cold beam, both deflect sideways at the joint tip. This tip motion is used as the actuation. The heating of the beams are controlled

to be very short, so the actuator is in a thermal transient during the actuation. The detailed mechanical and electrothermal modeling of the actuator are presented in the next sections.

3.1.1 Mechanical modeling approach

The force experienced at the actuator tip affects the tip displacement, and moreover how the whole actuator deflects. The goal of mechanical modeling is to find out the relation of the force and displacement at the actuator tip, given the dimensions of the actuator and the thermal expansion difference between the hot beam and the cold beam. Two important characteristics of the actuator are: (1) its blocked force f_{block} at the tip when the tip displacement is blocked; and (2) its free displacement d_{free} at the tip when no tip force is applied.

In the modeling, the temperature of the hot beam is assumed uniform, and the temperature of the cold beam is assumed to be zero. The basic modeling approach is: (1) separate the actuator into three free bodies: the hot beam, the cold beam and the connector at the tip; (2) write the relation of force/moment and displacement/rotation for each of these three members; and (3) solve for the equation array.

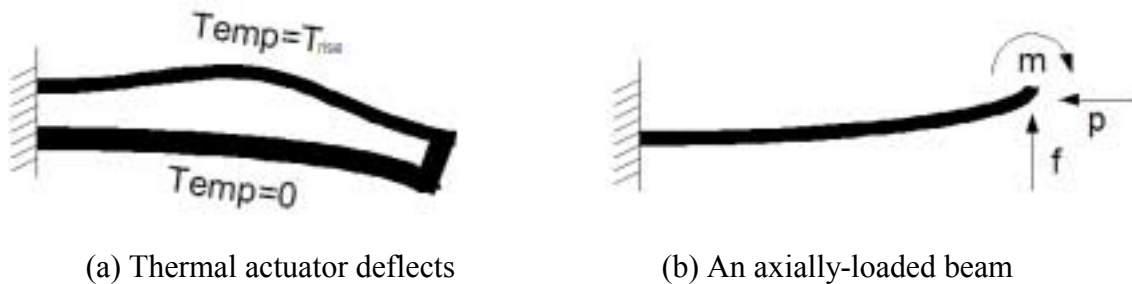


Figure 3-2 Thermal actuator mechanical model

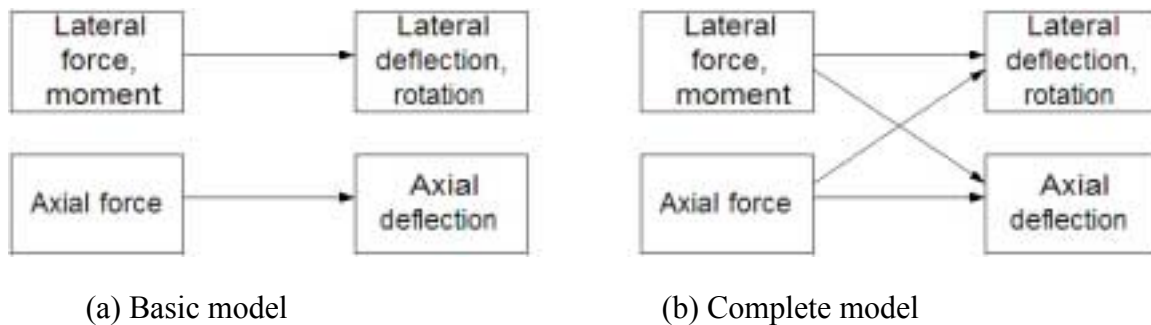


Figure 3-3 Treatment of the cantilever in the basic and the complete models

Two models for the mechanical deflection of the thermal actuator, shown in Figure 3-2 (a), are developed. The difference is their treatment of the cantilever, shown in Figure 3-2 (b), as a component of the thermal actuator, as shown in Figure 3-3. In the basic model, it is assumed that the lateral deflection of a beam is not affected by axial force, and the axial

deflection is not affected by lateral force and moment. In the complete model, those cross coupling effects are taken into account. The basic model gives a closed form solution and design, which can be verified and refined by the complete model.

3.1.2 Basic mechanical model

Assume a compression force P inside the top (hot) beam, a top beam thickness of t_h and a moment of inertial of I_h , bottom (cold) beam thickness of t_c and moment of inertial of I_c , gap between the two beams of t_g , beam depth into the paper of b , uniform temperature rise in the top beam of T_{rise} , thermal expansion ration of α , clockwise moment experienced by the top beam tip of m_h , the clockwise moment experienced by the bottom beam tip of m_c , the actuator tip lateral displacement δ , and the actuator tip rotation θ .

The moment balance of the connector between the two beam tips gives

$$P \left(\frac{t_h + t_c + 2t_g}{2} \right) = m_h + m_c \quad (3.1)$$

Assume that P has no effect on lateral deflection, the beam equations for the tip of the hot beam give

$$\delta = m_h \frac{l_h^2}{2EI_h} - f_h \frac{l_h^3}{3EI_h} \quad (3.2)$$

$$\theta = m_h \frac{l_h}{EI_h} - f_h \frac{l_h^2}{2EI_h} \quad (3.3)$$

The beam equations for the tip of the cold beam give

$$\delta = m_c \frac{l_c^2}{2EI_c} - f_c \frac{l_c^3}{3EI_c} \quad (3.4)$$

$$\theta = m_c \frac{l_c}{EI_c} - f_c \frac{l_c^2}{2EI_c} \quad (3.5)$$

The thermal actuator force is a sum of both forces,

$$f = f_h + f_c \quad (3.6)$$

Assuming that the lateral curving of the beams does not effect the axial tip position, the axial deformation geometric compatibility of the two beams gives

$$\alpha T_{rise} - \frac{P}{Ebt_h} - \frac{Pl_c}{Ebt_c l_h} = \theta \frac{(t_h + t_c + 2t_g)}{2l_h} \quad (3.7)$$

Equations (3.1)-(3.7) are linear equations, so the tip displacement is a linear function of tip force. The blocked force and free displacement can be obtained. For simplicity of the

expressions, assume both lengths are equal, and define $t_0 = \frac{(t_h + t_c + 2t_g)}{2}$. Then

$$f_{block} = \alpha T_{rise} \frac{3Eb(t_h^3 + t_c^3)t_0 t_h t_c}{2l(t_h^4 + t_h^3 t_c + t_h t_c^3 + t_c^4 + 3t_0^2 t_h t_c)} = \frac{3Eb\alpha T_{rise} t^2}{8l}, \text{ if } t_h = t_c = t_g = t \quad (3.8)$$

$$\delta_{free} = \alpha T_{rise} \frac{6t_0 t_h t_c l^2}{t_h^4 + t_h^3 t_c + t_h t_c^3 + t_c^4 + 12t_0^2 t_h t_c} = \frac{3\alpha T_{rise} l^2}{13t}, \text{ if } t_h = t_c = t_g = t \quad (3.9)$$

$$\frac{f_{block}}{\delta_{free}} = \frac{13Eb t^3}{8l^3}, \text{ if } t_h = t_c = t_g = t \quad (3.10)$$

3.1.3 Complete mechanical model

In the complete model, the lateral deflection and rotation are both caused by the lateral force and moment, and also amplified by axial compression, or de-amplified by axial tension. The self-enhancing amplification effect of axial compression is usually more significant than the self-limiting de-amplification effect of axial tension. On the other hand, the axial deformation, besides Hooke's law, is also determined by the curving of the beam from the lateral deflection. The cross effects shown in Figure 3-3 (b) are both very nonlinear, which make the complete model algebraically complex.

As a precursor to model development, consider the deflection of a single beam that is clamped at one end ($x=0$), free at the other end ($x=l$), yet compressed by axial force P , and deflected horizontally by force f and counterclockwise moment m applied at the free end, as shown in Figure 3-2 (b). The horizontal bending of the single beam is described by

$$EI \frac{d^2 w}{dx^2} = p(\delta - w) + m + f(l - x) \quad (3.11)$$

where E is the Young's modulus, I is the beam moment of inertia, w is the horizontal displacement, δ is the tip displacement, l is the length of the beam, and x is the axial coordinate. The tip rotation is

$$\theta = \left(\frac{dw}{dx} \right)_{x=l} \quad (3.12)$$

To clarify the analysis, define the normalized thickness

$$T = \frac{t}{l} \quad (3.13)$$

and the normalized variables

$$X = \frac{x}{l}, W = \frac{w}{t}, \Delta = \frac{\delta}{t}, \Theta = \frac{\theta l}{t}, N^2 = \frac{pl^2}{EI}, M = \frac{ml^2}{EI}, F = \frac{fl^3}{EI} \quad (3.14)$$

With these normalizations, (3.11) takes the form

$$\frac{d^2W}{dX^2} = N^2(\Delta - W) + M + F(1 - X) \quad (3.15)$$

The solution of (3.15) is

$$W = F \frac{\sin(NX) - \tan N \cos(NX) + \tan N - NX}{N^3} + M \frac{1 - \cos(NX)}{N^2 \cos N} \quad (3.16)$$

which gives a constitutive relation at the tip of

$$\Delta = c_{\Delta F}(N)F + c_{\Delta M}(N)M, c_{\Delta F}(N) = \frac{\tan N - N}{N^3}, c_{\Delta M}(N) = \frac{1 - \cos N}{N^2 \cos N} \quad (3.17)$$

and

$$\Theta = c_{\Theta F}(N)F + c_{\Theta M}(N)M, c_{\Theta F}(N) = \frac{\sin N \tan N + \cos N - 1}{N^2}, c_{\Theta M}(N) = \frac{\tan N}{N} \quad (3.18)$$

From Hooke's law, the beam compression strain is

$$\varepsilon = \frac{N^2 T^2}{12} \quad (3.19)$$

With a small deflection assumption, the ratio of the axial beam tip movement in the negative direction to the beam length is

$$\eta = \varepsilon + \frac{T^2}{2} \int_0^1 \left(\frac{dW}{dX} \right)^2 dX = \varepsilon + T^2 \left[c_{\eta F}(N)F^2 + c_{\eta M}(N)M^2 + c_{\eta FM}(N)FM \right]$$

$$c_{\eta F}(N) = \frac{2N \cos^2 N - 3 \sin N \cos N + N}{4N^5 \cos^2 N}, c_{\eta M}(N) = \frac{-\sin N \cos N + N}{4N^3 \cos^2 N}$$

$$c_{\eta FM}(N) = \frac{2 \cos^2 N + N \sin N - 2 \cos N}{2N^4 \cos^2 N} \quad (3.20)$$

We can now consider the thermal actuator, shown in Figure 3-2 (a), to be a combination of two beams with analytic notation defined in (3.13)-(3.20). Let the subscripts h and c denote the individual beams with hot beam h to the positive-deflection side of cold beam c . The deflection of the beam pair is as described in (3.15) through (3.20) with coupled boundary conditions at the tip. To continue the analysis, define

$$L_c = \frac{l_c}{l_h} \quad (3.21)$$

$$T_0 = \frac{2t_g + t_h + t_c}{2l_h} \quad (3.22)$$

where t_g is the gap between the two beams. The thermal strain difference between the two beams is

$$\varepsilon_\alpha = \alpha T_{rise} \quad (3.23)$$

where α is the thermal expansion rate and T_{rise} is the average temperature difference. Next, the two axial forces must have equal value but opposite sign so that

$$N_c = N_h \sqrt{-E_h I_h L_c^2 / (E_c I_c)} \quad (3.24)$$

Further, the moment and force relation at the tip of the actuator is

$$M_h + \frac{M_c E_c I_c T_c}{E_h I_h T_h L_c} + \frac{N_h^2 T_0}{T_h} = 0 \quad (3.25)$$

According to (3.17) and (3.18), the constitutive behavior of both beam tips is described by

$$c_{\Delta Fh}(N_h)F_h + c_{\Delta Mh}(N_h)M_h - \Delta_h = 0 \quad (3.26)$$

$$c_{\Delta Fc}(N_c)F_c + c_{\Delta Mc}(N_c)M_c - \Delta_c = 0 \quad (3.27)$$

$$c_{\Theta Fh}(N_h)F_h + c_{\Theta Mh}(N_h)M_h - \Theta_h = 0 \quad (3.28)$$

$$c_{\Theta Fc}(N_c)F_c + c_{\Theta Mc}(N_c)M_c - \Theta_c = 0 \quad (3.29)$$

The geometric constraints of the two beam tips are

$$\Theta_h - \frac{T_c}{T_h} \Theta_c = 0 \quad (3.30)$$

$$\Delta_h - \frac{L_c T_c}{T_h} \Delta_c = 0 \quad (3.31)$$

$$\varepsilon_a - \eta_h + L_c \eta_c + T_h^2 T_0 \Theta_h = 0 \quad (3.32)$$

Combining (3.19), (3.20) and (3.32) gives

$$\begin{aligned} \varepsilon_a - \frac{N_h^2 T_h^2}{12} + \frac{L_c N_c^2 T_c^2}{12} + T_h^2 T_0 \Theta_h - T_h^2 [c_{\varepsilon Fh}(N_h)F_h^2 + c_{\varepsilon Mh}(N_h)M_h^2 + c_{\varepsilon FMh}(N_h)F_h M_h] \\ + L_c T_c^2 [c_{\varepsilon Fc}(N_c)F_c^2 + c_{\varepsilon Mc}(N_c)M_c^2 + c_{\varepsilon FMc}(N_c)F_c M_c] = 0 \end{aligned} \quad (3.33)$$

Assuming a given K_h , (3.24) gives K_c , and then (3.25)-(3.31) are linear equations which can be summarized by

$$(F_h, M_h, \Delta_h, F_c, M_c, \Delta_c, \Theta_c)^T = Q_1 \Theta_h + Q_2 \quad (3.34)$$

where Q_1 and Q_2 are both 7-element vector functions of N_h . Substitution of (3.34) into (3.33) gives a quadratic equation,

$$q_1(N_h)\Theta_h^2 + q_2(N_h)\Theta_h + q_3(N_h) + \varepsilon_a = 0 \quad (3.35)$$

that can be solved for Θ_h . Given Θ_h , (3.34) then gives solutions for all other variables.

Returning to dimensional form, (3.14) gives

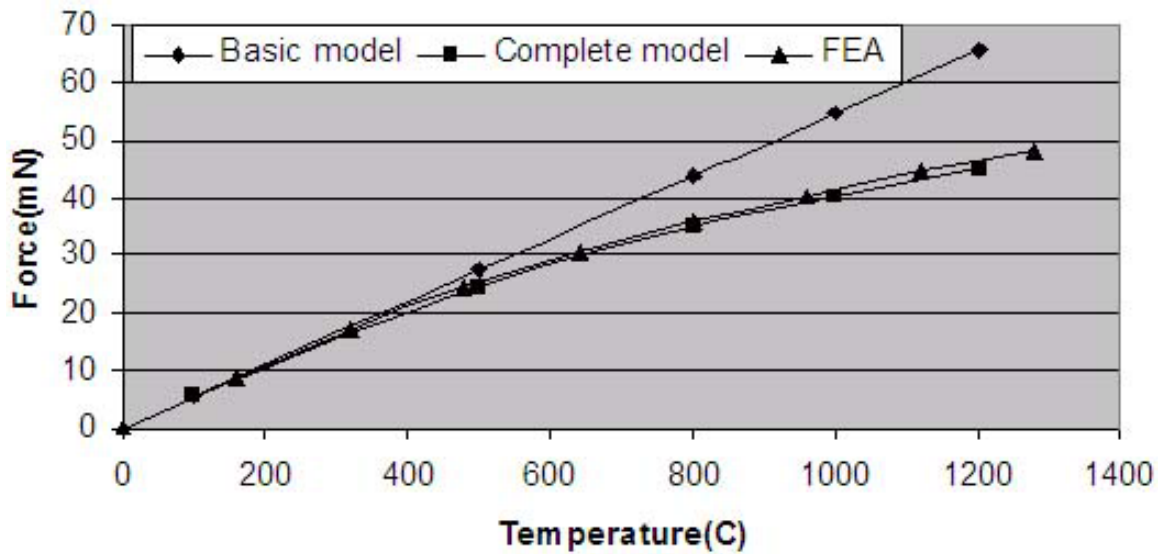
$$\delta_{free} = \Delta_h t_h \quad (3.36)$$

From a force balance and (3.14)

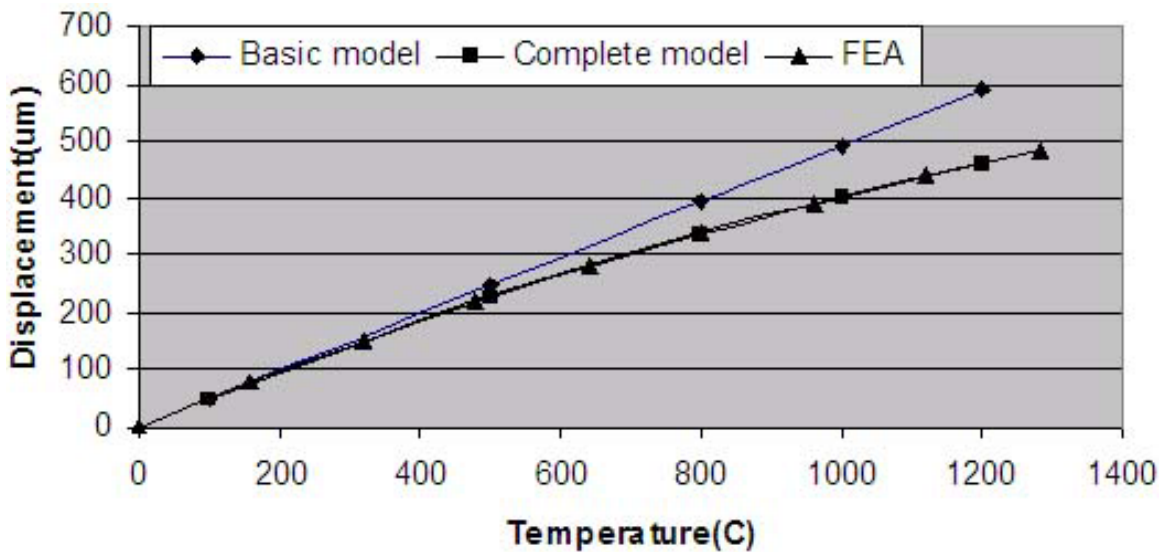
$$f_{block} = f_h + f_c = \frac{F_h E_h I_h t_h}{l_h^3} + \frac{F_c E_c I_c t_c}{l_c^3} \quad (3.37)$$

Note that (3.36) and (3.37) together give the force-displacement characteristic of the thermal actuator, parametrically over N_h . Therefore, varying N_h over a reasonable range sweeps the trajectory of the actuator force-displacement characteristic. A zero force gives the free displacement of the actuator; a zero displacement gives the blocked force of the actuator. The complete model is implemented in Matlab code as shown in Appendix A.

3.1.4 Mechanical model comparison and design



(a) Blocked force versus temperature



(b) Free displacement versus temperature

Figure 3-4 Comparison of thermal actuator model results

Both models can be compared with nonlinear FEA to show their effectiveness. A MatLab implementation of the model gives a result less than 1 second, while construction and running of an FEA model usually takes more than 10 minutes for a specific design. Figure 3-4 shows the model comparison for a thermal actuator having 6mm length, 80μm hot beam thickness, 60μm cold beam thickness, 20μm gap, 300μm depth, and 169GPa Young's modulus. The complete model strictly agrees with the FEA, while the basic model is only effective with low temperature. The thinner the hot beam compared to the cold beam, the lower the temperature with which the basic model could be effective. To have an effective transformation of axial expansion to lateral motion, a hot beam thickness similar to the cold beam is preferred.

In designing a thermal actuator with required temperature rise, blocked force and free displacement, the simple form of (3.8)-(3.10) assuming equal thickness and length can be used first to quickly identify the ratio of thickness over length, and the length of the thermal actuator. Then, the relative ratio of thicknesses could be fine tuned with the exact formula in equations (3.8) and (3.9), or they can be substituted into the complete model to verify the results. For practical proposes, the temperature rise in the hot beam should be kept below 300 degree C. Table 3-1 shows the thermal actuator design later used in the relay to actuate the bistable double beam shown in Table 2-1. The slightly larger force and displacement required for the thermal actuator than the ones with the double beam are due to the 20μm etch gap between them.

Table 3-1 Requirement and design of the thermal actuator used in the relay

Actuation requirements	$f_{block} = 13mN, \delta_{free} = 120\mu m, T_{rise} = 220K$
Mechanical design	$l = 6mm, t_h = 80\mu m, t_c = 60\mu m, t_0 = 20\mu m, b = 300\mu m$

3.1.5 Electrothermal modeling and design

Mechanical design determines the thermal actuator dimensions with given temperature rise to actuate the bistable element. The electrothermal design needs to heat the hot beam up to the temperature required. As discussed before, the basic method is to cover the colder beam metal to make it more electrically conductive than the hot beam. This permits differential heating and expansion of the beams as an electrical current is passed around them to produce the desired deflection.

Heat transfer has three mechanisms: conduction, convection and radiation. In MEMS scale, conduction is the dominant mechanism. To model the thermal effect in the thermal actuator, first it is important to know how fast the heat conducts in the silicon structure. A simple estimation is

$$t_{diff}(l_{diff}) = \frac{(\text{ThermalCapacity})l_{diff}^2}{(\text{ThermalConductivity})} = \frac{1.61 \times 10^6 \frac{J}{K \cdot m^3}}{157 \frac{J}{K \cdot m \cdot s}} l_{diff}^2 \quad (3.38)$$

where t_{diff} is the thermal diffusion time, and l_{diff} is the thermal diffusion length. (3.38) can also be written as,

$$l_{diff}(t_{diff}) = \sqrt{9.75 \times 10^{-5} t_{diff}} \quad (3.39)$$

The electrical pulse to heat up the thermal actuator is chosen to be $1ms$. (3.39) gives the thermal diffusion length in $1ms$

$$l_{diff}(1ms) = 315 \mu m \quad (3.40)$$

which is much less than $6mm$, the actuator length as given in Table 3-1, so the thermal diffusion in the actuator is negligible. Unlike many other thermal actuators, the actuator described here is a transient one. In this way, uniform temperature is maintained inside the hot beam and little heat flows into the cold beam, so the maximum expansion difference between the beams is obtained. To thermally diffuse through the $6mm$ whole length of the actuator, (3.38) gives the time required

$$t_{diff}(6mm) = 0.37s \quad (3.41)$$

which gives an estimate of how fast the thermal actuator can cool down. The thermal actuator mechanical structure can be actuated in a non-transient way too. With longer actuation time, the heat will flow in the structure and the temperature would change constantly before reaching a thermal steady state.

The electrical energy required is equal to the heat energy stored inside the hot beam, so for the thermal actuator shown in Table 3-1,

$$\begin{aligned} \text{ElectricalEnergy} &= \text{ThermalEnergy} = (\text{ThermalCapacity}) \times (\text{volumn}) \times T_{rise} \\ &= \left(1.61 \times 10^6 \frac{J}{K \cdot m^3} \right) (300 \mu m \times 80 \mu m \times 6mm) \times 220K = 50mJ \end{aligned} \quad (3.42)$$

The silicon resistivity determines the required excitation voltage and current. If an actuation voltage of $50V$ and pulse width of $1ms$ is desired, the resistivity of the wafer should be chosen as

$$\begin{aligned} \text{SiliconResistivity} &= \frac{(\text{Voltage})^2 (\text{PulseWidth})(\text{HotBeamDepth})(\text{HotBeamThickness})}{(\text{ElectricalEnergy})(\text{HotBeamLength})} \\ &= \frac{(50V)^2 (1ms)(300\mu m)(80\mu m)}{(50mJ)(6mm)} = 0.02(\Omega cm) \end{aligned} \quad (3.43)$$

The corresponding current at actuation is $1A$.

The metal layer should provide a much lower electrical resistance than the silicon it covers. Assuming only the top surface is covered by gold, to have one tenth of resistance as the silicon, its thickness is

$$Au \text{ Thickness} = 10 \frac{(\text{Au Resistivity})(\text{Silicon Depth})}{\text{Silicon Resistivity}} =$$

$$10 \frac{(2.35 \times 10^{-8} \Omega \cdot m)(300 \mu m)}{0.02 \Omega \cdot cm} = 0.5 \mu m \quad (3.44)$$

This means a gold layer of half micron should be enough to provide the high conductance. With this thickness, approximately equal to one tenth of the heat generated in the hot beam would be generated in the gold layer. According to (3.40), this heat would diffuse across the $300 \mu m$ silicon depth, so the temperature rise in the gold layer would be one order of magnitude lower than in the hot beam. However, even with this transient actuator, the heat will still flow from the hot beam to the cold beam through the junction after the electrical pulse. So the gold layer near the junction point will experience the hot beam temperature. Failure of gold layer at the junction was indeed observed during the operation of some of the devices.

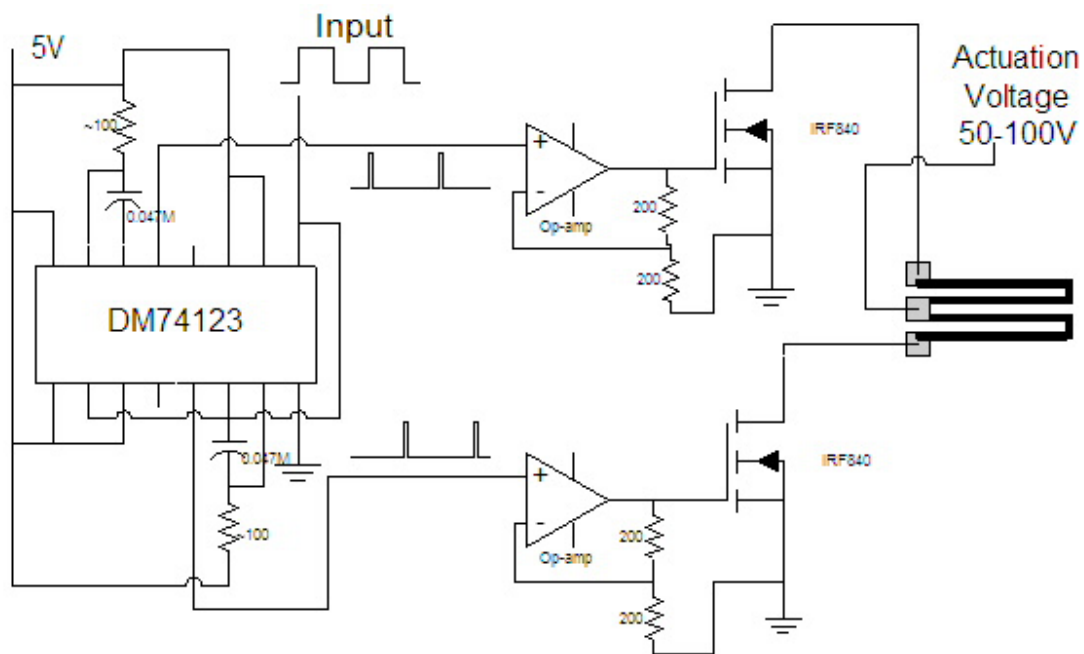


Figure 3-5 Electrothermal actuator driving circuit

Figure 3-5 shows the driving circuit to provide the electrical actuation pulse. A function generator feeds square waves to a pulse-generating chip DM74123. The width of pulses from the chip can be controlled by the external resistor and capacitor. These pulses go through Op-amps to be amplified, and then they can switch on the MOSFET. When either one of the transistors is switched on, a high voltage controlled by a power supply typically of 50-100 V is applied to the corresponding thermal actuator.

3.2 Electrostatic actuators considered

Electrostatic and magnetic actuations are commonly used in MEMS devices. An idea to use magnetic actuation is to place a permanent magnet close to the bistable double beam, and pulse a current through the double beam. The resulting Lorentz force may switch the double beam on or off. Estimation shows that this method would require a current too big or a magnetic field not realizable.

This section describes some work carried out to determine if electrostatic actuation could be feasible. It was decided that electrostatic actuators could be made to work, but they would require either larger size or more precise fabrication than the electrothermal actuator. To keep up the development speed for the relay, the electrothermal actuator was selected to go forward.

3.2.1 Feasibility study of comb drive type actuators

Table 3-2 Comparison of parallel plate, comb drive, and taper comb drive actuators

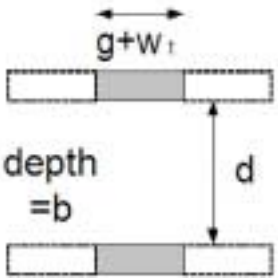
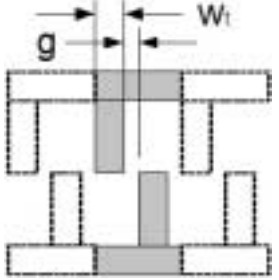
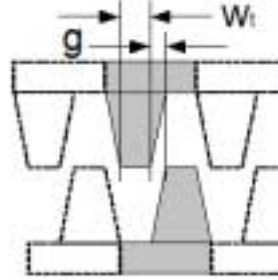
	 <p>(a) Parallel capacitor</p>	 <p>(b) Comb drive</p>	 <p>(c) Taper comb drive</p>
Capacitance per unit cell	$C_{par}(x) = \frac{2\epsilon_0(w_t + g)b}{d - x}$	$C_{comb}(x) = \frac{2\epsilon_0xb}{g}$	$C_{taper}(x) = \frac{2\epsilon_0xb}{g\left(1 - \frac{x}{d}\right)}$
Force per unit cell	$f_{par}(x) = \frac{\epsilon_0v^2(w_t + g)b}{(d - x)^2}$	$f_{comb}(x) = \frac{\epsilon_0v^2b}{g}$	$f_{taper}(x) = \frac{\epsilon_0v^2b}{g\left(1 - \frac{x}{d}\right)^2}$

Table 3-2 shows three types of electrostatic actuators. In the three figures, the shaded areas are each a unit cell of the actuator having the same length and maximum actuation strokes d . In the comb drive and taper comb drive actuator, the width of the fingers and the gap between fingers are w_t and g respectively. The smaller the w_t and g , the more forceful the actuators are. But they are both limited by the etching capability of the fabrication process.

A typical minimum dimension for a DRIE through-etch process is $w_t = g = 10\mu m$. The

capacitance and force per unit cell of each electrostatic actuator are derived and presented in the table, where ϵ_0 is the electrical permittivity, and the relation of capacitor and force is

$$f = \frac{v^2}{2} \frac{dC(x)}{dx} \quad (3.45)$$

Assuming $w_t = 10\mu m, g = 10\mu m, d = 120\mu m, b = 300\mu m, v = 100V$, the f-d curves of the electrostatic actuators shown in Table 3-2 are shown in Figure 3-6. The taper comb drive actuator is clearly much more forceful than the other two. To actuate the bistable mechanism shown in Table 2-1, more than $10mN$ of force and $100\mu m$ of stroke are needed. The curved beam bistable mechanism has its peak force close to the starting position, which is not good for comb drive actuation, which starts low and increases substantially toward the end of actuation stroke. The method shown in Figure 2-16 can be used to modify the f-d curve of the curved beam to shift the peak force to $96\mu m$. With the curved beam initially $20\mu m$ away from the taper comb drive, the f-d curve of 500 unit cells can snap the curved beam, as shown in Figure 3-7.

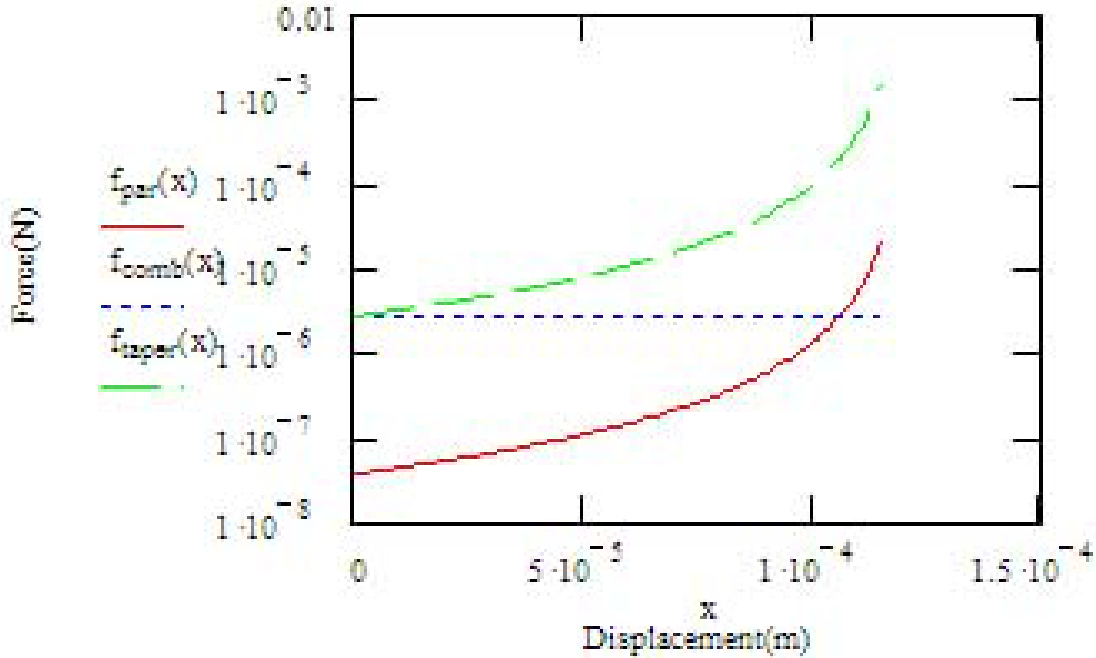


Figure 3-6 f-d curves of three comb drive type electrostatic actuator units

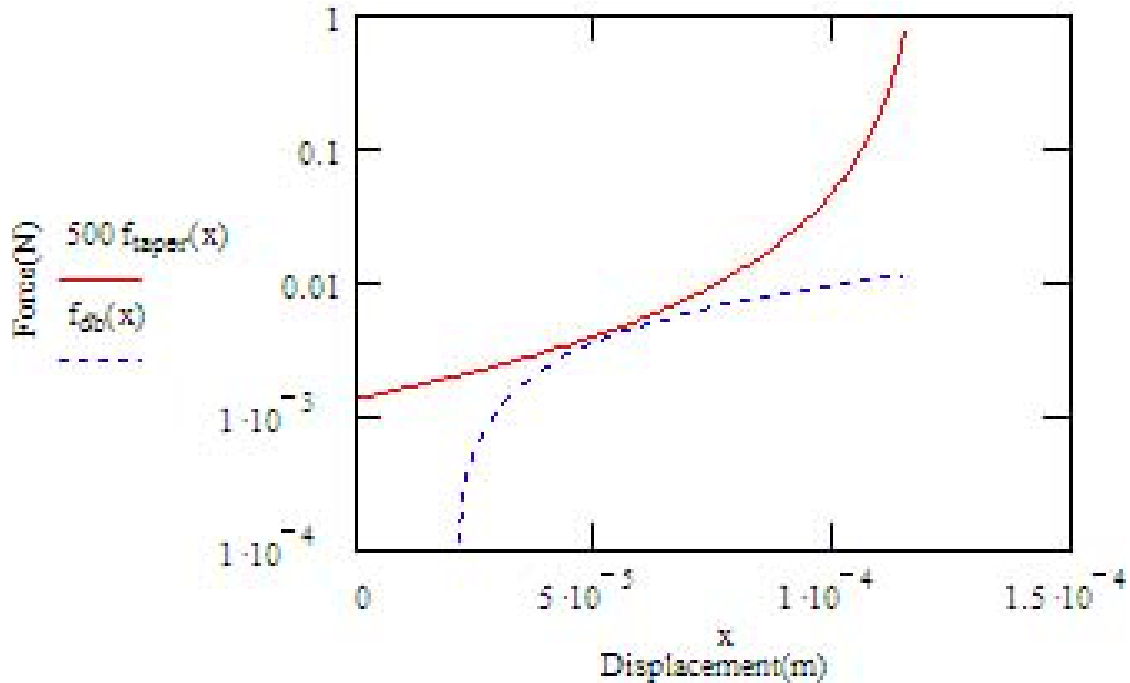


Figure 3-7 f-d curve for electrostatic taper comb drive and bistable mechanism

The 500 unit cells of taper comb drive are 20mm long if they are aligned one by one without any stacking arrangement. In order to support the moving half of the comb drive, bearings must be designed which should have low stiffness in the actuation direction and high stiffness in the perpendicular direction. The actuator must provide the force for the bearing flexure in addition to the force required to snap the bistable element. Since the tapered comb drive needs a larger size, it is abandoned in favor of the electrothermal actuator described in Section 3.1.

3.2.2 Preliminary study of zipper actuators

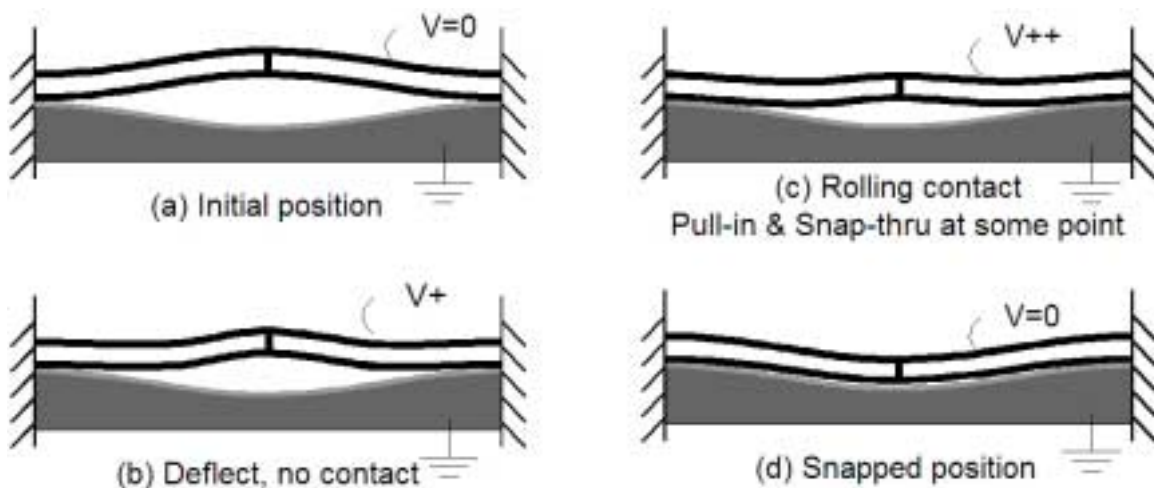


Figure 3-8 Electrostatic zipper actuator with rolling contact

One electrostatic actuation configuration with rolling beam contact is shown in Figure 3-8. Underneath the curved beam mechanism is an electrical ground with the shape negative to the beam shape. Between them is an oxide layer of thickness z , whose function is to prevent electrical shorts and breakdown. The electrical breakdown field density and maximum voltage applied across the oxide determines the minimum thickness of this layer. Figure 3-8 (a) shows the initial stage of actuation. When a voltage is applied on the curved beam, an electrostatic force pulls the curved beam down. In detail, the beams will first deflect with no contact as in stage (b), and then the contact point rolls from the clamped sides inward as shown in stage (c), at some point in stage (c), the beam mechanically snaps through, or pulls-in, toward the ground as shown in (d). At this point the double beam is in its second stable position. The difficulty of modeling this actuation arises from three parts. First, the amplitude of the electrostatic force depends on the beam deflection, which is at the same time determined by the electrostatic force. Second, the contact points roll, so no fixed boundary exists for the beam. Third, the axial compression of the beam makes the beam equation more nonlinear. The equation formation described in this section formalizes this hard problem to several nonlinear ordinary differential equations with fixed boundary conditions, which could then be solved numerically.

The initial shape of the beam is

$$\bar{w}(x) = \frac{h}{2} \left[1 - \cos\left(\frac{2\pi x}{l}\right) \right] \quad (3.46)$$

where h is the initial apex height, l is the beam length, and x is the horizontal coordinate with zero at the left clamped site. Due to symmetry, from now on only the left half beam is considered. The beam shape during bending is given by

$$w(x) = \begin{cases} -\bar{w}(x) & x \leq c \\ \text{unknown} & c < x < \frac{l}{2} \end{cases} \quad (3.47)$$

where c is the length between the rolling contact point and the clamped end. The electrical field strength in the gap is

$$E_e = \frac{v}{y + \frac{z}{\epsilon_{ox}}} \quad (3.48)$$

where y is the gap between two electrodes, z is the oxide layer thickness, and ϵ_{ox} is the relative electrical permeability of oxide. The force per unit length on the beam is given by

$$f_e = \frac{-b\epsilon_0 E_e^2}{2} = \frac{-b\epsilon_0 v^2}{2 \left(y + \frac{z}{\epsilon_{ox}} \right)^2} \quad (3.49)$$

where ϵ_0 is the permittivity of vacuum.

Before going to the detailed equation formation of this problem, a simple method could be used to estimate the maximum electrical energy as show in (3.50), which could be used to determine the lower bound of the required voltage to actuate the curved beams.

$$\text{Electrical Energy} = \int_0^L dx \int_{2\bar{w}(x)}^0 dy f_e = \int_0^l dx \frac{b\epsilon_0 v^2}{2} \left(\frac{1}{\frac{z}{\epsilon_{ox}}} - \frac{1}{2\bar{w}(x) + \frac{z}{\epsilon_{ox}}} \right) \approx \frac{bl\epsilon_{ox}\epsilon_0 v^2}{2z} \quad (3.50)$$

Now consider the detailed equation formation. The beam bending equation is

$$EI \left(\frac{d^4 w}{dx^4} - \frac{d^4 w_b}{dx^4} \right) + p \frac{d^2 w}{dx^2} = f = \frac{-b\epsilon_0 v^2}{2 \left(w + \bar{w} + \frac{z}{\epsilon} \right)^2}, \quad c < x < \frac{l}{2} \quad (3.51)$$

The beam compression equation is

$$\frac{pl}{Ebt} = \int_c^{\frac{l}{2}} \left[\left(\frac{d\bar{w}}{dx} \right)^2 - \left(\frac{dw}{dx} \right)^2 \right] dx \quad (3.52)$$

The beam boundary conditions at the rolling contact point are

$$w(c) = -\bar{w}(c), \quad \left(\frac{dw}{dx} \right)_{x=c} = \left(\frac{d\bar{w}}{dx} \right)_{x=c}, \quad \left(\frac{d^2 w}{dx^2} \right)_{x=c} = \left(\frac{d^2 \bar{w}}{dx^2} \right)_{x=c} \quad (3.53)$$

The beam boundary conditions at the beam center are

$$\left(\frac{dw}{dx} \right)_{x=\frac{l}{2}} = 0, \quad \left(\frac{d^3 w}{dx^3} \right)_{x=\frac{l}{2}} = 0 \quad (3.54)$$

Next, normalize the variables in (3.46) and (3.52)-(3.54) with

$$X = \frac{x}{l}, W = \frac{w}{h}, \bar{W} = \frac{\bar{w}}{h}, C = \frac{c}{l}, N^2 = \frac{pl^2}{EI}, Q = \frac{h}{t}, Z = \frac{z}{\epsilon h}, V = \frac{b\epsilon_0 v^2 l^4}{2EIh^2} \quad (3.55)$$

The new equations become

$$\frac{d^4 W}{dX^4} - \frac{d^4 W_b}{dX^4} + N^2 \frac{d^2 W}{dX^2} = \frac{-V}{(W + \bar{W} + Z)^2}, \quad C < X < \frac{1}{2} \quad (3.56)$$

$$N^2 = 12Q^2 \int_c^{\frac{1}{2}} \left[\left(\frac{d^2 \bar{W}}{dX^2} \right)^2 - \left(\frac{d^2 W}{dX^2} \right)^2 \right] dX \quad (3.57)$$

$$W(C) = -\bar{W}(C) \quad (3.58)$$

$$\left(\frac{dW}{dX} \right)_{X=C} = - \left(\frac{d\bar{W}}{dX} \right)_{X=C} \quad (3.59)$$

$$\left(\frac{d^2W}{dX^2}\right)_{X=C} = -\left(\frac{d^2\bar{W}}{dX^2}\right)_{X=C} \quad (3.60)$$

$$\left(\frac{dW}{dX}\right)_{X=\frac{1}{2}} = 0 \quad (3.61)$$

$$\left(\frac{d^3W}{dX^3}\right)_{X=\frac{1}{2}} = 0 \quad (3.62)$$

To remove the unknown boundary, make one more modification to X , let

$$\tilde{X} = \frac{2X - 2C}{1 - 2C} \quad (3.63)$$

then the new boundaries become $(0,1)$, and the initial shape is

$$\bar{W}(\tilde{X}) = \frac{1 - \cos\{\pi[2C + (1 - 2C)\tilde{X}]\}}{2} \quad (3.64)$$

To reduce the equations to an array of first order ordinary differential equations, define

$$W_1 = \frac{dW}{d\tilde{X}}, W_2 = \frac{d^2W}{d\tilde{X}^2}, W_3 = \frac{d^3W}{d\tilde{X}^3}, W_4 = \frac{d^4W}{d\tilde{X}^4} \quad (3.65)$$

then the equations become

$$\frac{dW}{d\tilde{X}} = W_1 \quad (3.66)$$

$$\frac{dW_1}{d\tilde{X}} = W_2 \quad (3.67)$$

$$\frac{dW_2}{d\tilde{X}} = W_3 \quad (3.68)$$

$$\frac{dW_3}{d\tilde{X}} = \frac{d^4\bar{W}}{d\tilde{X}^4} - \frac{(1-2C)^2}{4} N^2 W_2 + \frac{-V(1-2C)^4}{16(W + \bar{W} + Z)^2}, 0 < \tilde{X} < 1 \quad (3.69)$$

$$(W)_{\tilde{X}=0} = (\bar{W})_{\tilde{X}=0} \quad (3.70)$$

$$(W_1)_{\tilde{X}=0} = \left(\frac{d\bar{W}}{d\tilde{X}}\right)_{\tilde{X}=0} \quad (3.71)$$

$$(W_2)_{\tilde{X}=0} = \left(\frac{d^2\bar{W}}{d\tilde{X}^2}\right)_{\tilde{X}=0} \quad (3.72)$$

$$(W_1)_{\tilde{X}=1} = 0 \quad (3.73)$$

$$(W_3)_{\tilde{X}=1} = 0 \quad (3.74)$$

$$N^2 = \frac{24Q^2}{1-2C} \int_0^1 \left[\left(\frac{d\bar{W}}{d\tilde{X}} \right)^2 - W_1^2 \right] d\tilde{X} \quad (3.75)$$

Additional modification could turn the unknown C and (3.75) into differential equations. Define

$$N_p^2 = \frac{24Q^2}{1-2C} \int_0^{\tilde{X}} \left[\left(\frac{d\bar{W}}{d\tilde{X}} \right)^2 - W_1^2 \right] d\tilde{X} \quad (3.76)$$

We have

$$\frac{dC}{d\tilde{X}} = 0 \quad (3.77)$$

$$\frac{dN_p^2}{d\tilde{X}} = \frac{24Q^2}{1-2C} \left[\left(\frac{d\bar{W}}{d\tilde{X}} \right)^2 - W_1^2 \right] \quad (3.78)$$

and,

$$(N_p^2)_{\tilde{X}=0} = 0 \quad (3.79)$$

The six ordinary differential equations (3.66)-(3.69), (3.77) and (3.78), six boundary conditions (3.70)-(3.74) and (3.79), could be solved numerically.

At stage (b) of Figure 3-8, the beam deflects with the second derivative at the clamped site continuously changing until it matches the one of the ground. In this case,

$$C = 0 \quad (3.80)$$

$$(W_2)_{\tilde{X}=0} = g, \quad \frac{-\pi^2}{2} < g < \frac{\pi^2}{2} \quad (3.81)$$

The solution of this case involves five ordinary differential equations and five boundary conditions.

The modeling described above reduces a complex beam bending problem in electrostatic field with rolling boundaries to several ordinary differential equations involving fixed boundary conditions. Numerical solution of these equations was attempted but not finished due to shift of focus. Modeling of such actuator was discussed and continued in the work reported in [30].

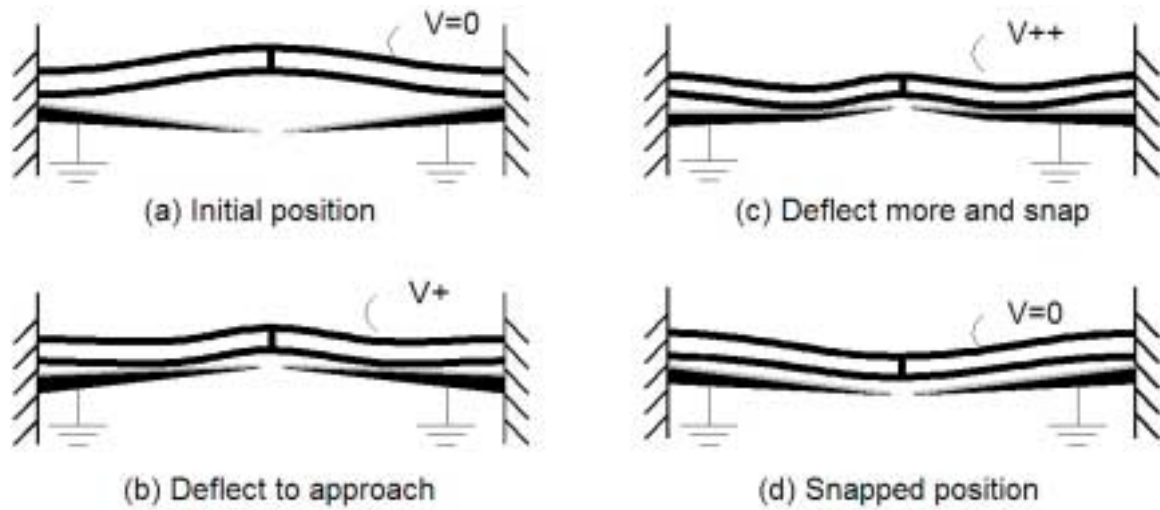


Figure 3-9 A zipper actuator concept with flexible elements

Electrical force is inversely proportional to the square of the gap between two electrodes, so the effectiveness of zipper actuator is critically dependent on the initial electrode gap. On the other hand, DRIE can not produce initially zero gap electrodes as shown in Figure 3-8 . A flexible electrodes concept may help close the initial electrode gap and increase the actuation force. Figure 3-9 (a) shows the initial stage of such a configuration. When a voltage is applied between the curved beam and the more-flexible cantilevers, an electrostatic force pulls the curved beam down, while pulls the flexible cantilevers up which helps reducing the gap as shown in stage (b). As both of them deflect more as shown in stage (c), the double beam finally snaps through to reach stage (d), the second stable position it can retain without voltage. In order to realizing both the approaching motion of the flexible beams to the double beam, and then the snap-through of both structures, this actuation scheme requires critical deflection coordination design of the double beam and the flexible beams. The deflection could be designed quasi-statically or dynamically, with a possible design parameter the thickness modulation of the flexible beams, which is shown as a wedge shape in Figure 3-9. This actuation mechanism was not modeled in this thesis due to its complexity and the decision to focus on electrothermal actuator instead. Several designs were included in the mask set #M1 as shown later in Table 5-3 which were planned to be experimentally tested. However, such experiment was not conducted. A good zipper design was later realized in the work reported in [30].

Chapter 4

RELAY CONTACT

This chapter describes the mechanical design and process development to achieve better relay contact.

4.1 Mechanical design of the contact

As shown in Figure 1-3, the basic contact component employed in this relay comprises a flat crossbar and two flat relay contacts. The crossbar, attached to the bistable double beam through a cantilever, is required to provide balanced contact force on both contacts when the double beam's deflection toward the second stable position is blocked. The shape of the contact structure and the mechanical characteristics of the double beam can both vary with the fabrication errors. The flat-flat contact shapes and the compliant cantilever coupler are designed to lower the dependence of the two contact forces on the fabrication variation. This section describes the details of these mechanical designs.

4.1.1 Identification of ideal contact shape



Figure 4-1 Contact geometry explored

Apart from the contact structure design comprising a flat crossbar and two flat relay contacts, various other crossbar and contact shapes have been fabricated and tested as shown in Figure 4-1. In the figure, the upper element is the crossbar, which can move vertically to close the two contacts at the lower position. Even with the extra cantilever compliance discussed later in Section 4.1.2, all of these have worse contact resistance than the flat-flat contact shown in Figure 1-3. In most cases, the crossbars shown in Figure 4-1 can only make contact on one of the two contacts, with the other one not touched.

The conclusion is that with non-flat shapes, it is hard to have balanced contact force on each of the two contacts. There may be three reasons. First, non-flat edges have more variation during the mask making and photolithography steps, so the position errors are larger than flat ones. Second, all of these non-flat shapes have point contact in 2D, while an equal amount of shape variation is more significant for points or sharp corner than for flat edges.

And third, several configurations shown in Figure 4-1 have the contact surface not perpendicular to the crossbar motion. Friction can occur in these cases, which makes the contact positions unpredictable.

4.1.2 Design of contact compliance

As Figure 2-5 shows, the f - d relation of a second-mode-constrained curved beam has three regions of different stiffness. They are two short segments of very large positive stiffness at the beginning and the end of the curve, and a long region of low negative stiffness in between. For a double beam bistable beam as shown in Figure 2-7 (a), the center clamped is designed to constrain the second (twisting) mode during beam deflection at the negative stiffness region. Even though most of the second mode is constrained, some remains, as can be observed in Figure 2-8 (c), which makes the orientation of beam center unpredictable. However, during the second positive stiffness region, there is no second mode presented so the beam center is perfectly leveled. Thus the second positive stiffness region is where the contact should be positioned.

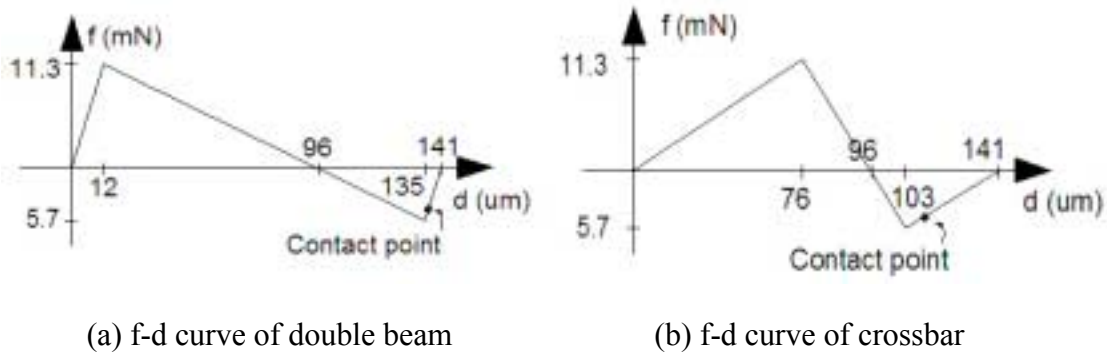


Figure 4-2 f - d characteristic of double beam and softspring-coupled crossbar

Figure 4-2 (a) shows the f - d curve of a double beam mechanism whose dimensions are given in Table 2-1. To have a total contact force of $4mN$, the contact point, as shown in Figure 4-2 (a), should be positioned at about $137\mu m$ on the d axis. However, two factors affect the relative position of the contact point on the f - d curve. First, photolithography and DRIE through-etching can typically produce an etched feature width variation of about $4\mu m$ from the mask design, as indicated by the measurement of the etched beam shown in Figure 2-9. Second, the variation of double beam thickness can change the shape of the f - d curve. Both these effects can make the relative position of the contact point on the f - d curve unpredictable and may even prevent contact.

Inclusion of a cantilever beam having the dimension described in Table 4-1, as shown in Figure 4-3, solves this problem. Figure 4-2 (b) shows the f - d curve of the crossbar attached to the cantilever. With the extra compliance of the cantilever, both positive stiffness regions of the double beam become much more compliant, while the negative stiffness region becomes stiffer. Now the contacts should be designed to be $114\mu m$ away from the etched

position of the crossbar, closer than without the extra compliance, to have the desired contact force of $4mN$. The contact force variance resulted from the etched gap variance of $4\mu m$ is reduced to $0.6mN$ with the modified f-d curve.

Table 4-1 Design of a contact structure

Double beam bistable mechanism	Defined in Table 2-1
Cantilever dimensions	$12\mu m$ thick, $500\mu m$ long, $300\mu m$ deep
Gap between cross bar and contact	$114\mu m$
Total contact force	$4mN$

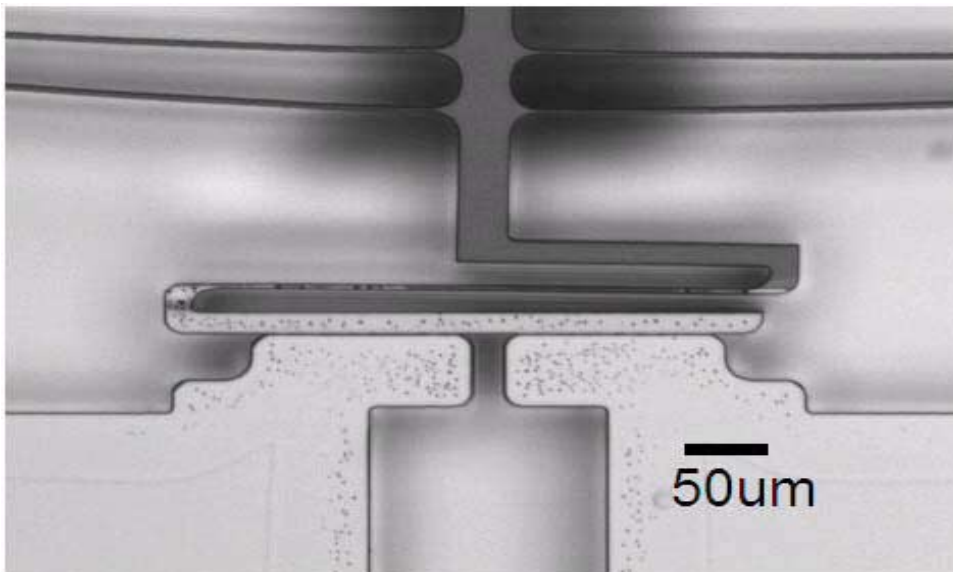


Figure 4-3 Microscope picture of the cantilever and the closed contacts

The center of the two contacts, the crossbar, and the double beam are aligned in the moving direction of the double beam. In this way the crossbar remains horizontal when pushed against the two contacts and the force on the two contacts are equal. The cantilever beam can also mechanically self-adjust to balance the force on each contact as well as to conform the crossbar to the contacts when opposite contact sidewalls are slightly unparallel vertically.

4.2 Process development for DRIE sidewall contact

4.2.1 Challenges

As restricted by the DRIE through-etch process, the relay components move parallel to the wafer surface. Consequently the relay contacts are through the sidewalls of the DRIE etched structures. As described in Table 4-2, this thesis identifies five challenges in making good

relay contact through the sidewalls, and proposed/experimented solutions to these challenges.

Table 4-2 Challenges of the DRIE sidewall relay contact and solutions

Section	Source of challenge	Challenges	Solutions attempted
4.2.2	DRIE bottom-of-etch problems	How to avoid point contact at the bottom of DRIE etch	(1) Direct mounting (2) Backside shallow etch
4.2.3.1	Teflon residue from DRIE	How to have reliable metalization at the sidewall	Cleaning processes
4.2.3.2	Grooves (vertical and horizontal) on the DRIE sidewall	How to smooth the sidewall for better contact and metalization	Wet etching
4.2.4	Sharp edge between wafer top and the DRIE etched sidewall	How to make metal coverage continuous over the DRIE channel edge	Etching of shallow nibbles on edge
4.2.3.3	Vertical sidewall and deep etched channel	How to have sufficient metal at the sidewall	Electroplating after sputtering

4.2.2 Alleviation of bottom-of-etch problem

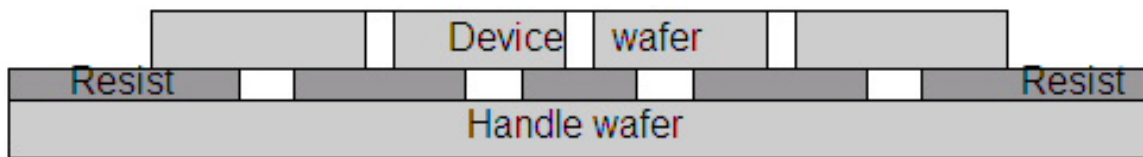
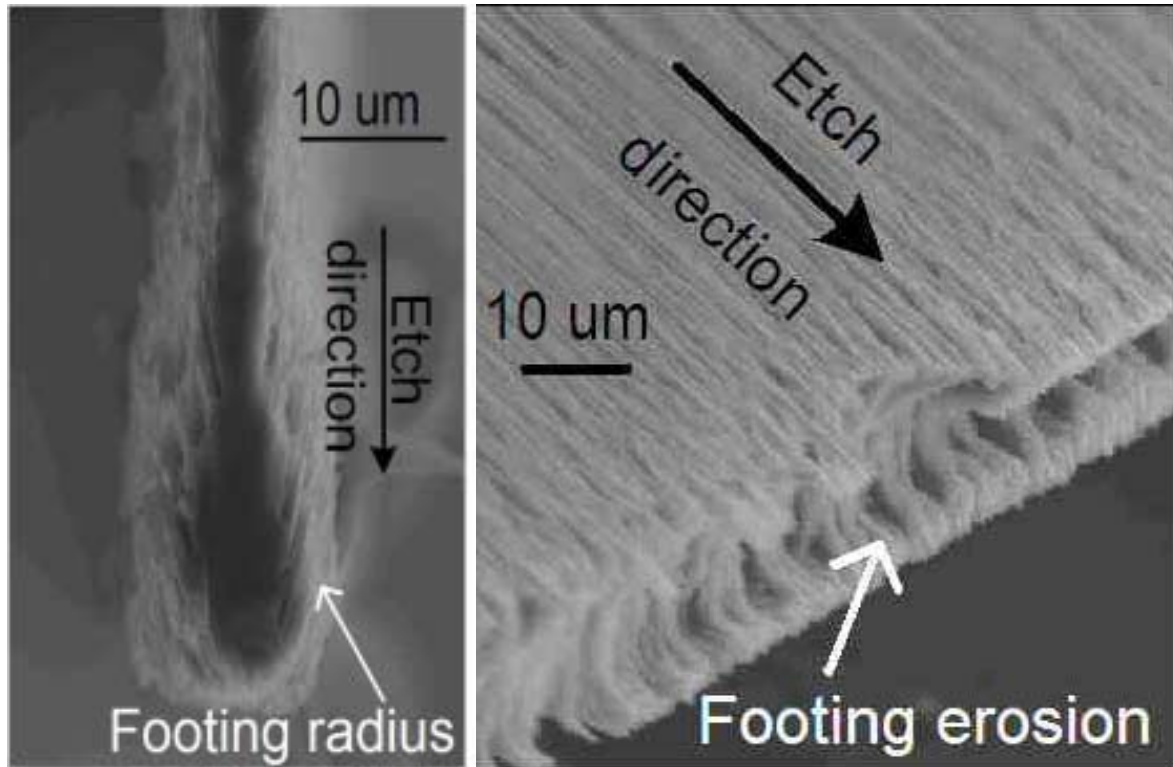


Figure 4-4 Regular wafer mounting method for DRIE through-etch

The DRIE generates significant heat during etching, which without proper cooling could damage both the etched features and the photoresist mask. The wafer is pressed down by pegs and helium is circulated at the back of the wafer to cool it down. For a through-etch, a handle wafer is resist mounted at the back of the device wafer so that the helium would not escape through the etched holes. Figure 4-4 shows this regular wafer mounting method by resist rings. The device wafer and handle wafer are dismantled after the etching.

The etching ions are deflected by the mounting photoresist when the wafer is etched through. This would create two effects. First, the bottom edge of the etched structure is not etched effectively due to the stagnancy of the etching ions, so a wider bottom of etch is resulted as shown in Figure 4-5 (a), which is a zoomed-in picture of the structure shown in Figure 2-9. As observed in many runs of etching, this effect can not be overcome by over-etching. Second, the backside of the etched structure is attacked by the deflected ions so eroded structure results; in an extreme case a concave shape at the bottom can be created as shown in Figure 4-5 (b). These two effects coexist, resulting in irregular extrusions at the bottom of etch, which also has low fracture stress. The crossbar and relay contacts with such

feature can only have point contact at the bottom, with poor electrical contact as a result. Two methods are conceived to solve this bottom-of-etch problem. One fails but the other worked out well. Both are described hereafter.



(a) Wider bottom

(b) Eroded bottom

Figure 4-5 SEM pictures of the bottom of DRIE etched beams

4.2.2.1 Direct mounting method

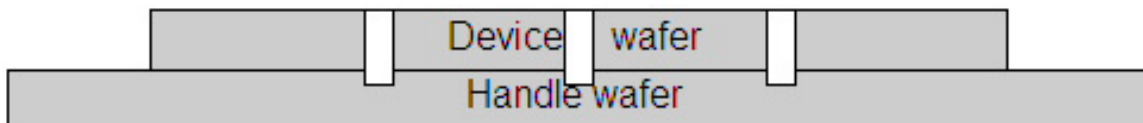


Figure 4-6 Direct mounting method

Figure 4-6 shows the direct mounting concept, where the device wafer is directly mounted to the handle wafer without the use of resist. With this mounting method, etching can continue to the handle wafer so a clearly etched bottom of the device wafer can result. The device wafer is to be separated from the handle wafer afterward. The mounting takes the form of temporary bonding. It should be good enough so that the heat generated in the etch can flow from the device wafer to the handle wafer, at the same time it should be reversible so after the etching the device wafer can be separated from the handle wafer without breakage. Experiment proves that this process can leave a well etched bottom structure. But despite the

many test runs shown in Table 4-3, a good enough bonding for thermal diffusion is not found so the resist burns during etching (#16,17,18), and even these inadequate bond can not be separated without causing wafer breakage.

Table 4-3 Test runs for the direct mounting method

#	Preparation	Result
1	Mounting sides cleaned (all cleaning is done on coater with acetone, methanol and water). Weight pressed for half hour.	Bonding not good.
2	Weight rolled on the wafer pair of #1 with a fab-wiper in between.	Bonding better but thin resist patterns damaged.
3	New wafers same process as #1. Device wafer peripheral resist-covered by coater, q-tip.	Bonding not good, the helium leak rate (HLR)=24m Γ
4	Handle wafer only, polished side down.	HLR=8m Γ
5	Handle wafer only, rough side down.	HLR=11m Γ .
6-9	Practice of mounting two bare silicon wafers. It is found that gently pressing two cleaned wafer together by hand is the best way to have good bonding.	Bonding becomes reliable. HLR~11m Γ .
10	Wafers cleaned and hand pressed together on table with fab wipes underneath. Device wafer peripheral covered with resist by q-tip.	Bonding good. HLR~24m Γ , even after piranha cleaning of the backside.
11	Device wafer and handle wafer cleaned on coater. Device wafer placed face down on coater and handle wafer pressed on.	Bonding ok. Many cracks on the resist due to the coater contact. HLR~11m Γ .
12	#11 covered by resist with q-tip on device wafer peripheral. prebake 15mins.	HLR~18m Γ .
13	#12 handle wafer back cleaned	HLR~15.5m Γ .
14	More than half of the resist at the peripheral of the device wafer removed from #13.	HLR~14m Γ .
15	A new set of wafer mounted with no resist on device wafer peripheral.	HLR~9m Γ . Resist on device wafer failed after 3 hours DRIE etch.
16	A new set same with #15 but weight pressed for 15mins.	Same problem with #15.
17	A new set first RCA cleaned, then bonder bonded to a 4in handle wafer, then photolithography and resist mounted to a 6 in handle wafer.	1/3 resist burned with etch not through. Cannot separate device from handle.
18	A new set RCA cleaned, BOE roughened the handle for 15mins. Manually mounted.	Resist burned.

In the test, quality of mounting is observed by an IR camera which can show fringes indicating the non-bonded area between two wafers. The DRIE machine uses helium

circulation at the back of the processed wafer for cooling. The helium leak rate (HLR) is measured as an indication of the quality of conforming between the handle wafer and the machine seat. The higher the HLR, the worse the conforming, and the harder the heat generated during etching can be diffused to the machine seat. The machine used to do the test allows a maximum HLR of $15m\Gamma$, above which it would not start etching. A high HLR is usually resulted from dirty wafer backside, wafer bowing, or even hidden cracks in the wafer. One interesting thing noticed during the direct mounting test is that the photoresist covering over the edge of the device wafer peripheral and the handle wafer always causes a helium leakage problem. This is believed to result from the internal force induced by the baked resist between the two wafers, which can bow the handle wafer up for helium to leak.

4.2.2.2 Backside shallow etch method

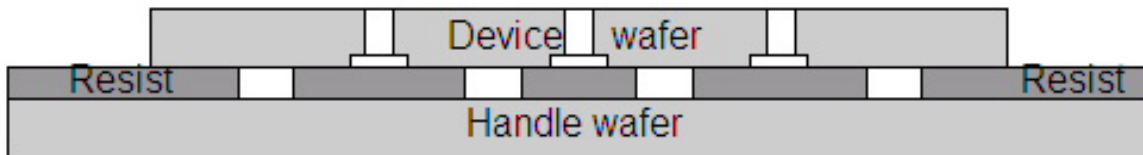


Figure 4-7 Backside shallow etch method

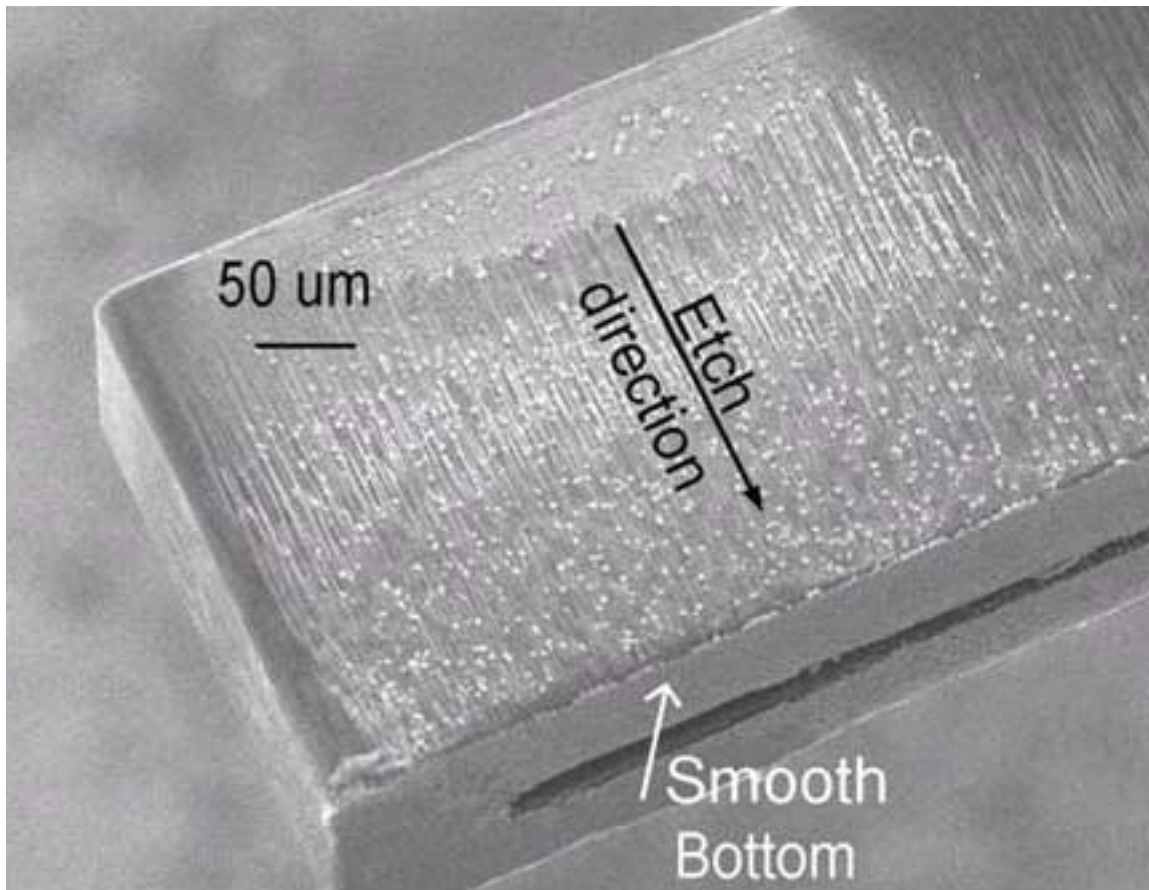


Figure 4-8 The clear bottom of etch with backside shallow etch method

Figure 4-7 shows the backside shallow etch method. The critical areas at the backside of the device wafer is first shallow etched by about 20 μm before being mounted and through-etched from the front side. Figure 4-8 shows a SEM picture of the bottom of structure etched by this method. Since the bottom of the etched structure does not directly contact the mounting resist, the etching ions can leave a clean bottom-of-etch without the problems shown in Figure 4-5.

4.2.3 Sidewall surface treatment and metalization

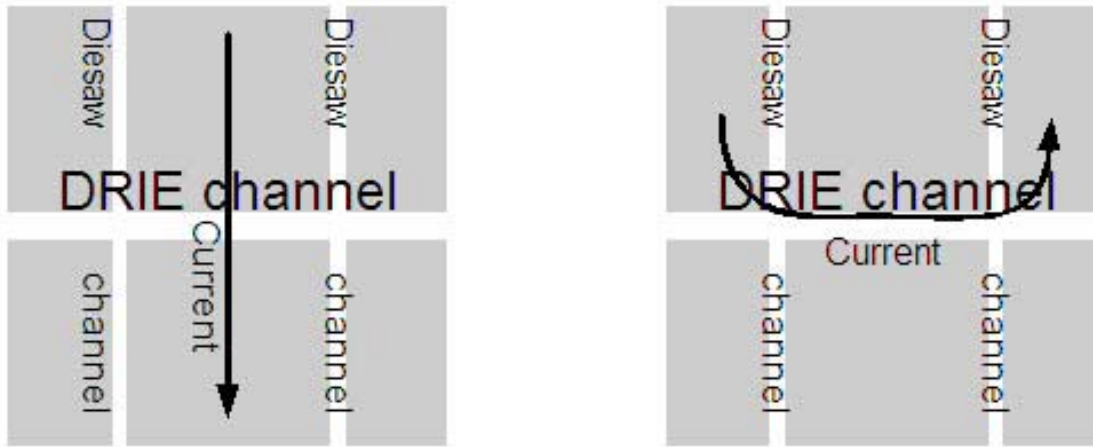
This thesis develops a three-step metalization to achieve a low on-state resistance for the relay contact. First, the sidewall is properly cleaned. Second, a seed layer is deposited through a hard mask of the shadow wafer by sputtering process. Third, the device is electroplated to get sufficient metal coverage on the sidewalls. This section explains the development works which converge to this metalization process.

4.2.3.1 Sidewall cleaning and seed metal layer deposition

Both e-beam and sputtering process may be used to deposit the seed metal layer. In the e-beam process, the small-size source metal is placed far from the wafers, so the evaporated metal beam can be considered to come from a point source. Two carriers of the wafers are available. In the first one a stationary plate stays directly above the metal source, so the metal beam hits the wafer almost in a normal direction. In the second one the carrying plates are placed at a tilted angle with the metal beam direction. The tilted plates can be rotated during the process, so metal beam can hit the wafer from different angles. To deposit the metal on DRIE etched sidewalls that is vertical to the wafer surface, the tilted wafer carriers must be used instead of the stationary one. To cover both sidewalls facing each other, the tilted plate must either be rotated continuously, or more efficiently, be placed in two positions consecutively so the metal can be e-beamed on the two sidewalls one at a time.

In the sputtering process, the target metal has a size comparable to the wafer, and is placed close to it. So each point on the wafer can receive metal from a large variation of angle, which makes the metal conformity better than with the e-beam process. However, in a deep channel, a point can only see the limited target metal directly above the channel opening, so the deposited metal is much thinner than on the wafer surface. Geometric estimation shows that a 300 μm deep sidewall with a 100 μm gap opening above it can only receive averagely about 10% of the metal deposited on the top wafer surface. Even with this drawback, the sputtering process is still needed to deposit seed layer of metal on DRIE sidewalls for the electroplating process discussed later.

Early experiments of the metalization with either e-beam or sputtering have significant adhesion problems, which is believed to result from the Teflon residue left from the DRIE etch. Several cleaning steps are conceived which include a DRIE isotropic etch using SF_6 for 20 seconds following the through-etch, a half-hour O_2 plasma ashing by asher, a 0.5- μm thermal oxide growth at the temperature of 1100 degree C, and a BOE striping of this oxide.



(a) Full channel method

(b) Half channel method

Figure 4-9 Metalization quality measurement method**Table 4-4 Metalization process matrix and resistance measurement**

Wafer piece #	DRIE MIT69A 90mins	DRIE SF614 20secs	Asher O ₂ 30mins	Tube SiO ₂ 0.5 μ m	HF oxide	Sputter Au 0.9 μ m	e-beam Au 0.54 μ m	Full channel (Ω)	Half channel (Ω)	Metal peeling
1	yes	yes	yes	yes	yes	yes		0.026	0.21	no
2	yes	yes	yes	yes		yes		0.129	0.31	no
3	yes	yes	yes			yes		0.226	0.29	some
4	yes	yes		yes		yes		0.069	0.44	some
5	yes	yes		yes	yes	yes		0.097		all
6	yes	yes				yes		0.353		all
7	yes	yes					yes			no
8	yes	yes	yes				yes		2.7	no
9	yes	yes	yes	yes	yes		yes		15.7	no
10	yes	yes	yes	yes			yes		34.9	no
11	yes	yes		yes	yes		yes		43.5	some
12	yes	yes		yes			yes		51.7	no

To obtain a quantitative measurement of the influences of each cleaning and metalization step on the final relay contact performance, a matrix study was performed on DRIE etched channel structures. Channels of about 200 μ m deep are DRIE etched on a wafer that is subsequently broken into many pieces to go through a matrix of processing steps as shown in Table 4-4. After metalization, the wafer pieces are first die-sawed into smaller pieces of approximately 1 cm by 1 cm, and then two die-saw cuts of about 50 μ m deep are applied on the pieces to remove the deposited metal as shown in Figure 4-9, which also shows the two resistance measurement methods used to quantify the metalization quality. In the full channel method shown in Figure 4-9 (a), the current is applied from the top center pad to the bottom center one, which goes through the metal on both the sidewalls and the bottom part

of the DRIE etched channel. In the half channel method shown in Figure 4-9 (b), the current is applied from the top left pad to the top right pad, which goes through the metal deposited on the segments of the upper sidewall of the DRIE channel intersected with the two die-saw cut shallow channels. In both measurements, 4-point-probe method is used to measure the resistance. The conclusion of the matrix study shown in Table 4-4 is that the sputtering process is much better than the e-beam process, and all the cleaning steps are helpful for either better metalization adhesion or lower resistance.

4.2.3.2 Wet etch process for smoothing the sidewall

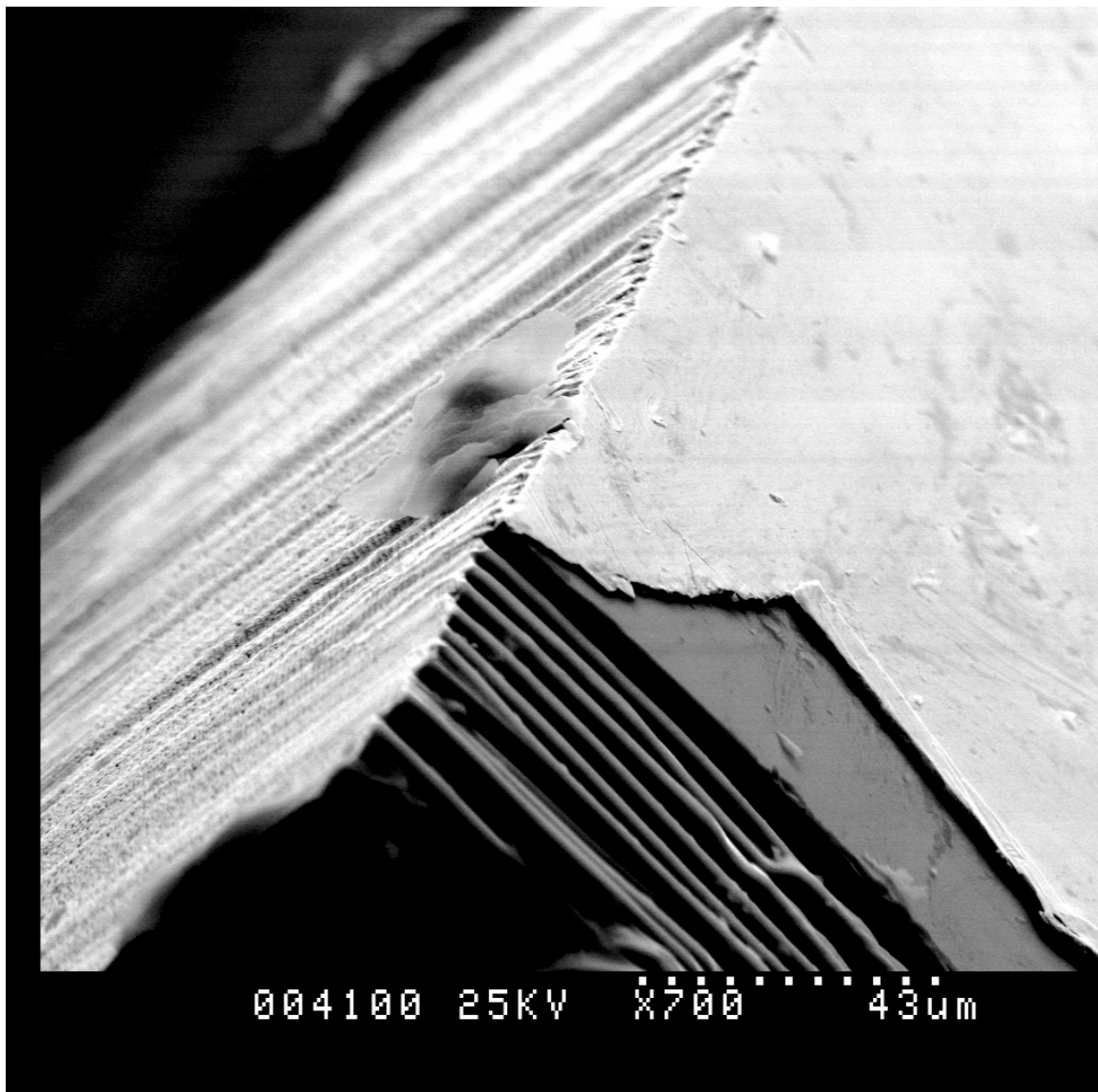
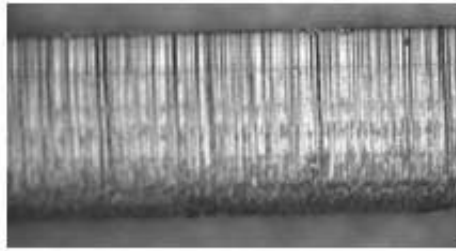
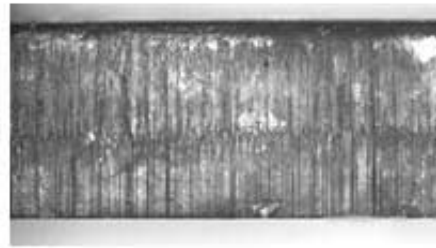
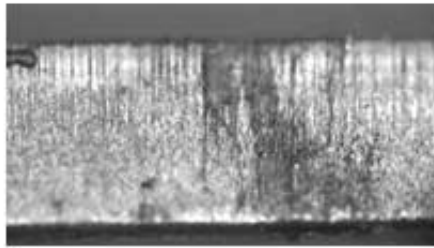


Figure 4-10 Metal on DRIE sidewall with many grooves

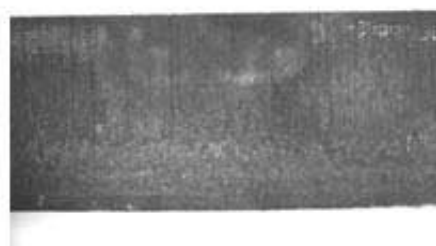
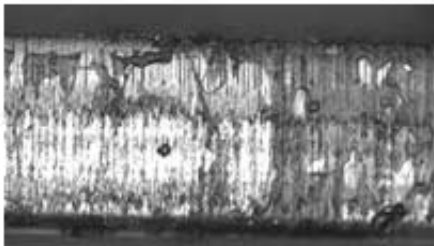
Before etch



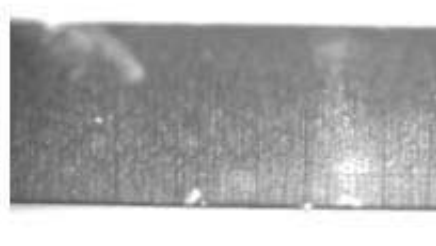
30 sec



1 min



2 min



5 min



HF:HNO₃:H₂O=50:10:40 HF:HNO₃:H₂O=70:10:20

Figure 4-11 Sidewalls of DRIE etched structure after wet etch

As Figure 4-10 shows, the sidewall of the DRIE etched surface has many vertical grooves following the etching direction. DRIE also creates smaller horizontal scallops that cannot be seen from this picture. These groove features can result in point contact when two sidewalls

are pushed together, and can also shadow the metal deposition on the bottom of these grooves to create low conductance current path.

Wet etching processes, which produce rounded corners and smooth surfaces due to their anisotropic nature, are attempted to remove the grooves of the DRIE etch. A wet etch with HF, HNO₃, and water [31] is found in literature to be able to etch silicon in a wide variety of etching speed depending on the composition of these three chemicals. Two sets of experiments were performed to develop this process to smooth the grooves. In the first experiment, five wafer pieces are immersed into five recipes, with five different chemical compositions, and the etch rate and resulting surface conditions are observed. It is found that the etch rate varies significantly; with large HF percentage, the wafer pieces disappears in less than one minute; with low HF, the etch rate is low and the surface turns a little gray. In the second set of experiment, two sets of concentration are selected based on the result of the first experiment, and DRIE etched silicon pieces are immersed into the chemicals for various length of time. As Figure 4-11 shows, two minutes etch with a composition of HF:HNO₃:H₂O=70:10:20 gives the most smooth sidewall. The channel depth was not measured precisely after the wet etches, but observation under microscope does not show a noticeable depth change after the etching. The smooth wafer surface becomes rough after wet etching, which shows that the wet etching makes rough surface smoother and at the same time makes the smooth surface rougher.

Table 4-5 Measured resistance for wet etched channels

		1 st sample	2 nd sample	3 rd sample
Samples w/o wet etching		200 mΩ	190 mΩ	
Samples with wet etching		65 mΩ	75 mΩ	61 mΩ
Wet etched samples annealed in N ₂ for 30 mins	200 degree C	65 mΩ	67 mΩ	66 mΩ
	250 degree C	61 mΩ	58 mΩ	52 mΩ
	300 degree C	40 mΩ	47 mΩ	52 mΩ

The test samples go through all the cleaning steps identified in the last section and are sputtered with 0.9 μm of gold. The same etched and die-sawed pattern as the one shown in Figure 4-9 was measured to quantify the influence of wet etching and post-sputtering annealing on metalization. The silicon samples were subjected to the wet etching of the second composition as shown in Figure 4-11 for 2 minutes. The measured resistance is shown in Table 4-5, which shows that wet etching does improve the resistance by about three times even without the post-sputtering annealing step. Annealing in a tube with nitrogen ambient further lower the resistance, with 300 degree C the reduction is about 30%. Note, however, the same improvement of resistance by annealing is not observed on the test samples that were not wet etched, as indicated later in the experiments summarized in Table 4-6.

Though the wet etch reduced metalization resistance significantly, it is not used in the final fabrication of the relay due to its fast etch rate. A beam of 20μm could be etched away by the two minutes wet etch identified in Figure 4-11. On the other hand, the electroplating

method described later could deposit a metal layer thickness larger than the depth of grooves, so the wet etch was not explored further.

4.2.3.3 Electroplating

As discussed earlier, neither the e-beam nor the sputtering can provide enough metal coverage at the vertical DRIE etched sidewalls. Electroplating transfers metal directly from the solution in which the wafer is immersed, so the metal coverage is not affected by the location. As long as there is a seed metal layer of above $0.1\ \mu\text{m}$, the current can go through it and the metal can be deposited. About 2 to $3\ \mu\text{m}$ of electroplated Cu give a very good contact resistance.

The copper plating for example is from a commercial acid sulfate solution. Periodic pulse plating with a 5-ms on time and a 1-ms off time is used to improve the uniformity of film thickness and sidewall coverage. The plating was done under constant temperature of 18 degree C with mild agitation of the plating solution. The current amplitude and plating time is determined by the desired plating thickness and area. In a typical setting, 0.1 A of current lasting for 9 minutes plates $2\ \mu\text{m}$ of Cu on a $10\ \text{cm}^2$ area. After electroplating, thorough rinsing and drying is performed to remove any sulfate from the device to avoid fast oxidation.

4.2.4 Edge nibble method for metal continuity across edge

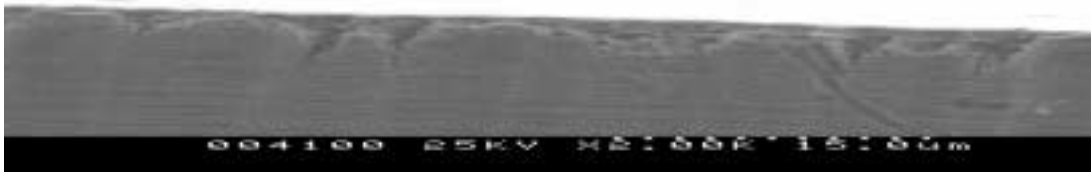


Figure 4-12 Poor metal continuity across the edge between wafer top and sidewall

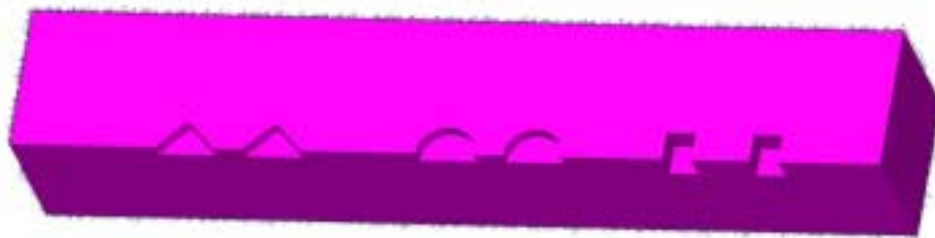


Figure 4-13 Edge nibble concept

Figure 4-12 shows a SEM picture of the sputtered Au across the edge between wafer top and DRIE sidewall. To have good conductance for current path, the poor continuity of metal

over the edge should be alleviated. Figure 4-13 shows a concept to improve the metal continuity. The nibbles are etched at the wafer top before the through-etch that then cuts across the nibbles so afterward, the nibbles would be on the edge. Ideally these nibbles, with depth and possibly also characteristic length on the same order or smaller than the thickness of metal to be deposited, would help accumulate the metal over the edge to make it continuous.

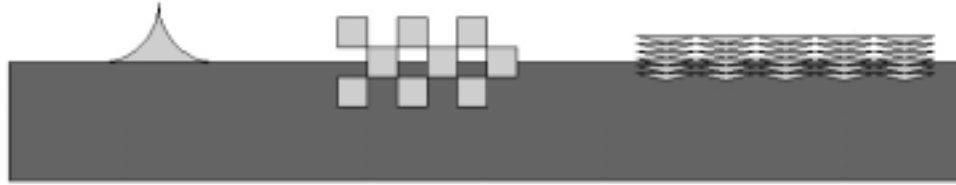


Figure 4-14 Edge nibble patterns

Figure 4-14 shows a top view of some possible nibble patterns, with the dark rectangle denotes the deep channel, and the light shapes denote shallow nibbles etched before the deep etch. Only shallow patterns on one side of the deep channel are shown. Apparently, the part of the light shapes inside the dark channel would be etched away during the deep etch. The first shape has a continuous transition toward the deep channel edge; this continuity may help the metal connection between the shallow etch sidewall and the deep etch sidewall. However, due to the alignment difficulty, this shape could not be aligned perfectly with the deep channels as shown in the figure. The remaining two patterns are thus more feasible. The second pattern consists of many small squares stacked together, the stacking in the horizontal direction ensures multiple possible nibble connections for the metal, and the stacking in the vertical direction lowers the alignment requirement between the two etchings. The characteristic dimension of these nibbles is on the order of the thickness of metal to be deposited. The third pattern has many wedge shapes stacked together. The large aspect ratio of these wedge shapes ensures an almost continuous transition between the sidewalls of the shallow etch and the deep etch.

Table 4-6 Measured resistance for edge nibbled channels

1 μm deep nibble w/ 0.9 μm sputtered Au	no nibble	big square	middle squares	Small squares	big wedge	Small wedges
1 st sample	0.20 Ω	0.23 Ω	0.24 Ω	Peel off	0.21 Ω	0.28 Ω
2 nd sample	0.19 Ω	0.20 Ω	0.23 Ω	0.23 Ω	0.20 Ω	0.24 Ω
250C 30min anneal	0.23 Ω				0.19 Ω	0.29 Ω
300C 30min anneal	0.17 Ω				0.16 Ω	0.18 Ω

Table 4-6 shows the resistance testing result of edge nibbled channels by a same approach as shown in Figure 4-9. No significant improvement of the resistance is observed. Figure 4-12 shows that the discontinuity of the metal at the edge is about 1 or 2 μm . The metal thickness and nibble depth are only about 1 μm . With a larger deposited metal thickness and/or etched nibble depth, the edge nibble method may show more promise.

Chapter 5

THE RELAYS

This chapter describes the design, fabrication and testing of the relay based on the component development presented in previous chapters. Most improvement from one generation of relay to the next is driven by the need to improve contact resistance.

5.1 Design

Table 5-1 Guidelines of design for fabrication of the relay

1.	The etching capability of DRIE dictates that the minimum feature thickness of the device is 10 μm .
2.	The DRIE process requires the minimum etched channel width of about 20 μm , otherwise the etch time would be too long and resist may fail.
3.	For uniform DRIE etch rate, the etch channel should have the same width across the wafer. For wide etches, a halo should be used where only the boundary of the silicon piece to be removed is etched and all enclosed silicon pieces will fall out after through-etch.
4.	The maximum strain level of all moving parts should be designed well below the fracture strain of DRIE etched silicon structure, which is about 0.2%.
5.	To lower stress concentration, fillets should be created at the sharp corners of moving structure.
6.	To prevent the structure from breaking during fabrication and handling, the lowest resonance frequency of any part should be above 1kHz.
7.	To lower the possibility of arcing during relay operation, all critical sharp corners of the relay should be rounded.
8.	To hold the device features together after through-etching, breakoff tabs should be used which would be removed after fabrication and before testing.
9.	Metal deposited on silicon has a eutectic temperature lower than either melting point, at which the metal will diffuse into the silicon and resistance will increase. So the thermal actuator working temperature should be designed as low as possible. For Au, it should be less than 300 degree C.

The functional requirements of the relay are described in Section 1.2.1. These requirements drive the design of the relay system. Also, the MEMS fabrication process put many constraints on the device design; the important ones for the design of this relay are shown in Table 5-1. With the functional requirements given in Section 1.2.1 and the design guidelines

of Table 5-1, the bistable double curved beam, the thermal actuators, and the relay contact structures can be designed in that order. All three components have been designed and modeled in the previous chapters.

Table 5-2 Characteristics of the design of relays with large and small dimensions

	Large	Small
Double beam thickness	20 μm	12 μm
Double beam apex height	120 μm	72 μm
Double beam length	6 mm	4 mm
Contact force	4 mN	4 mN
Actuation force	13 mN	13 mN
Actuation stroke	180 μm	120 μm
Thermal actuator length	12 mm	6 mm
Hot beam thickness	120 μm	80 μm
Cold beam thickness	120 μm	60 μm
Hot and cold beam gap	50 μm	20 μm
Actuation energy	150 mJ	50 mJ
Flexible cantilever length	12 mm	5 mm
Flexible cantilever thickness	20 μm	12 μm
Device wafer thickness	300 μm	300 μm
Device wafer resistivity	$\sim 10^{-2} \Omega\text{-cm}$	$\sim 10^{-2} \Omega\text{-cm}$
Actuation time	2 ms	1 ms
Actuation voltage	$\sim 80 \text{ V}$	$\sim 50 \text{ V}$

To save cost and time, transparency masks were used in masking for most of the relays. The minimum feature size of a transparency mask is about 20 μm . With the exposure dimension reduction of ten times by a stepper machine, the minimum feature size is theoretically 2 μm but practically 5 μm . However, the through-etching capability of DRIE process requires a minimum feature size above 10 μm . Two main groups of relays have been designed, one is relatively large, for which no stepper is needed, and the other is smaller. The large-scale design has a minimum feature size of 20 μm , while the smaller one has a minimum feature size of 12 μm . These numbers dictate the design of the double beam, which then dictates the design of the thermal actuators and the contact structure. Typical design values of the two groups of relay are listed in Table 5-2, where most of the design values of the small scale relays are given in Table 2-1, Table 3-1 and Table 4-1.

In all, thirteen mask variations are used, as described in Table 5-3. Mast set M13 of the relay are shown in Appendix B. Much time was spent to find out a way to produce these complex mask patterns and an efficient and reliable approach gradually converged. In this approach, Pro/E is used to create the 3D solid model of the masks, whose cross-sectional view is then generated and exported in dxf format. The dxf file is modified by AutoCAD for minor changes of color and line width, and then opened by Freehand or Adobe Illustrator for final touching. This approach can handle large and complex mask patterns.

Table 5-3 Relay mask set chart

Mask #	Description
M1	Double beams of various dimensions. Electrostatic Zipper actuator test structure: rigid zipper, flexible zipper, and taper-shaped flexible zipper. Electrical breakdown test structure.
M3	Large scale thermal relay. Only utilized half wafer area due to software problem for drawing masks. Flexible flat – bump contacts.
M5	Some detail improvement over M3. Flexible flat – bump contacts. Rigid flat – bump contacts. Half circle – bump contacts. Wedge -- bump contacts.
M6	Some detailed improvement over M5.
M7	Some detailed improvement over M6. Backside etch mask.
M8	Some detailed improvement over M7. Backside etch mask. Flexible flat – flat contacts. Hollow wedge – wedge contacts. Rigid flat – flat contacts.
M10	Small scale thermal relay. Backside etch mask. Flexible flat – flat contacts.
M11	Similar to M10. Small scale thermal relay. Wired shadow mask pattern for electroplating
M12	Similar to M11. Shadow mask opening shrunk to prevent electroplating overflow. Handle anchor shrunk for better plating isolation.
M13	Similar to M12. Thermal actuator disconnected from shadow mask wire pattern.

5.2 Fabrication

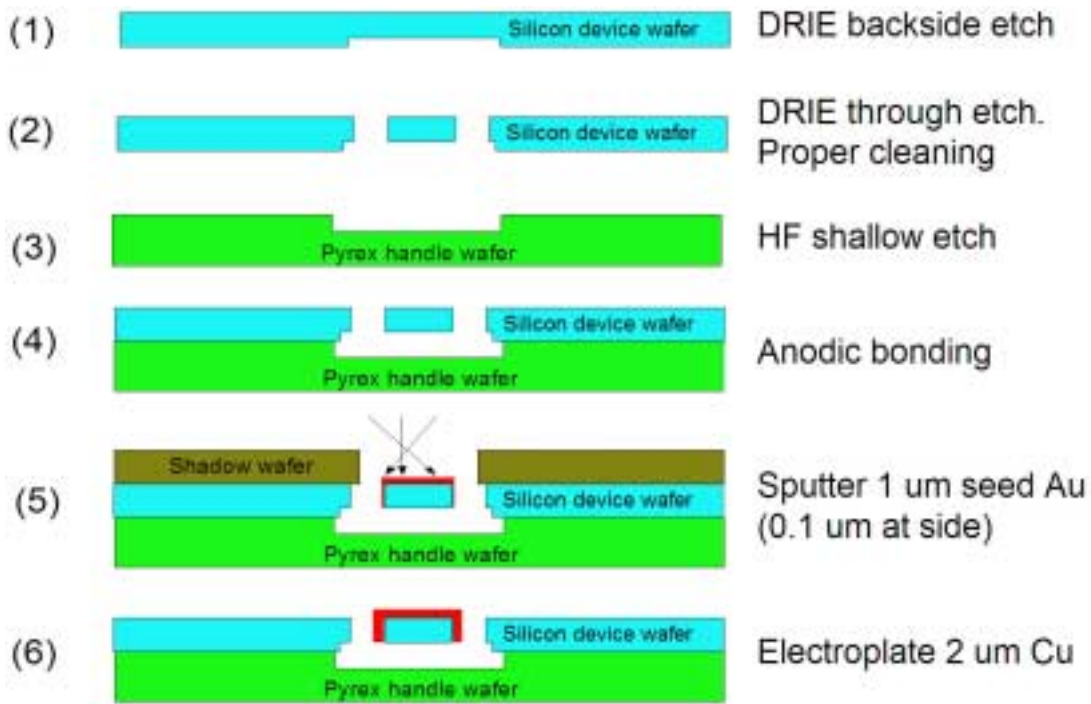


Figure 5-1 Key fabrication steps

The MEMS relays of both the large and small scales have been fabricated and successfully tested. The N-type 4-inch silicon wafer used for most fabrication has a 0.01-0.05 Ω -cm resistivity, and a 315- μ m thickness. The 4-inch Pyrex handle wafer has a 500- μ m thickness.

Fast-turnaround and economic mask printing was adopted for fabrication. The mask pattern was first printed on a transparency by a commercial service with a feature resolution of about 10 μ m. Then the transparency pattern was transferred to a resist-covered chrome glass plate by photolithography. Finally the chrome plate was etched and cleaned. The time required to turn a mask drawing into a real mask is two days. For better resolution, a stepper exposure process was used, which has a 10:1 dimension reduction capability.

Table 5-4 Relay device chart

Year	Wafer# Mask#	Ash	SiO2	Handle	Metalization	Backside etch	Resistance
01	G1 M3	No	No	Si	E-beam 0.3 μ m Au	No	Reduced from ~100 Ω to ~0.4 Ω
01	G2 M3	No	No	Si	E-beam 0.3 μ m Au	No	
01	G3 M3	No	No	Si	E-beam 0.3 μ m Au	No	
01	G4 M5	No	No	Si	E-beam 0.3 μ m Au	No	
01	G5 M6	Yes	Yes	Pyrex	Sputter 0.9 μ m Au	No	
01	G6 M7	Yes	Yes	Pyrex	Sputter 0.9 μ m Au	Yes	
02	G7 M8	Yes	Yes	Pyrex	E-beam 0.3 μ m Au	Yes	
02	G8 M8	Yes	Yes	Pyrex	E-beam 0.3 μ m Au	Yes	
02	G9 M8	Yes	Yes	Pyrex	E-beam 0.3 μ m Au	Yes	
02	G10 M10	Yes	No	Pyrex	Sputter 0.9 μ m Au	Yes	
02	G11 M10	Yes	No	Pyrex	Sputter Au Plate Au	Yes	140 m Ω
02	G12 M10	Yes	No	Pyrex	Sputter Au Plate Cu	Yes	60m Ω
02	G13 M11	Yes	No	Pyrex	Sputter Au Plate Cu	Yes	
02	G14 M12	Yes	No	Pyrex	Sputter Au Plate Au	Yes	
02	G15 M13	Yes	No	Pyrex	Sputter Au plate Cu	Yes	~160m Ω
03	G16 M13	Yes	No	Pyrex	Sputter 0.9 μ m Cu	Yes	>10 Ω
03	G17 M13	G15 metal stripped					
03	G18 M10	G11 metal stripped			Sputter 0.9 μ m Au		

Figure 5-1 shows the main fabrication process steps for the relay, and Appendix C lists the more detailed steps. First, a backside shallow pit of about 20 μ m is etched by DRIE on the device wafer. Second, the device feature is through-etched by DRIE from the front side. All isolated parts etched in this step remain attached to the wafer by break-off tabs so that they do not fall off. The DRIE etch recipe "MIT69A" was used as developed in the Microsystems Technology Laboratories (MTL) of MIT. The total time taken to etch through the wafer thickness of 300 μ m was about 3 hours with a 20 μ m halo gap. In the third step, a Pyrex handle wafer receives a shallow etch of 50 μ m to define pits below the device-wafer components that will move. Fourth, the device wafer is anodically bonded to the handle wafer. Fifth, a shadow wafer is etched by DRIE and is placed on top of the device wafer.

The device wafer is sputtered with 500 Å of Ti and 1 μm of Au with the shadow wafer acting as a mechanical mask. The shadow wafer is designed so that all sputtered metal on the relay contacts are wired together. This provides a current path for subsequent electroplating. In the sixth step, about 2 μm of copper or gold are electroplated on the device wafer. Details of the metalization processes are described in Section 4.2.

Many devices were fabricated during the course of this thesis, among them are about twenty sets of device, as shown in Table 5-4, that were completed and tested. The detailed description of each generation of device is presented in next section.

5.3 Testing

After fabrication, the break-off tabs, which functions as mechanical support and electroplating conduction lines, in the device wafer are manually broken to achieve electrical isolation between device features, and the relay is ready for testing. An external source, as shown in Figure 3-5, provides pulses for the thermal actuators through probes.

Referring to Table 5-4, G1–G9 are large-scale thermal relays. Initially, the silicon handle wafer was fusion bonded to the device wafer, various shapes of the contact were tried out, and the metalization was by e-beam. Thermal actuation worked out well from the beginning, but the contact resistance was high, ranging from several tens of Ω's to infinite. Work described in Chapter 3 were carried out to find ways to improve the contact resistance. Changes were then made on the new masks and devices. G10-G18 were small scale relays, where stepper was used to improve the resolution of transparency mask. Testing results of wafer G11-G16 are presented hereafter.

G11 and G12 were metalized without a shadow mask, so the testing was only for the relay contacts. G11 did not have good electrical isolation. When the relay was at the off-state position R was about 140 mΩ, while at on position R was about 70 mΩ. The bad isolation was believed to be from the non-ideal Au electroplating, which may connect the device wafer and handle wafer electrically. G12 contacts worked well. The lowest contact resistance measured was 60mΩ, while all measured resistances were below 100 mΩ.

G13 was the first attempt to include the wired metal pattern across the wafer for selective electroplating. The metalization was not good; the hot beams of the thermal actuators also received some metal. Brief testing of the contact resistance was not as good as G12. G14 had improved shadow mask and handle mask patterns to prevent the metalization overflow during electroplating, however, the overflowing still happens, as shown in Figure 5-2.

G15 and G16 had a better shadow mask pattern, where the thermal actuators are isolated from the wires to prevent the overflowing of electroplated metal. This worked. The bistability test results are shown in Figure 5-3. G15 was sputtered by Au, and then electroplated with Cu. Among the 37 dies, 21 dies survived the fabrication, and 14 of them showed bistability. G15 was fully functional. Typically, 1-ms pulses with between 50 and 60 Volt amplitudes are required to actuate a relay. Three contact resistances measured were 147 mΩ, 156 mΩ,

and 180 m Ω . One of the contacts carried 1.8A without melting the contact metal. The reason for higher resistance than G12 is believed to be the thinner Cu film judged from electroplating condition (2 μm versus 2.5 μm). The resistance did not change much even with a manual push to add force and it did not vary with the amplitude of the current passing through it.

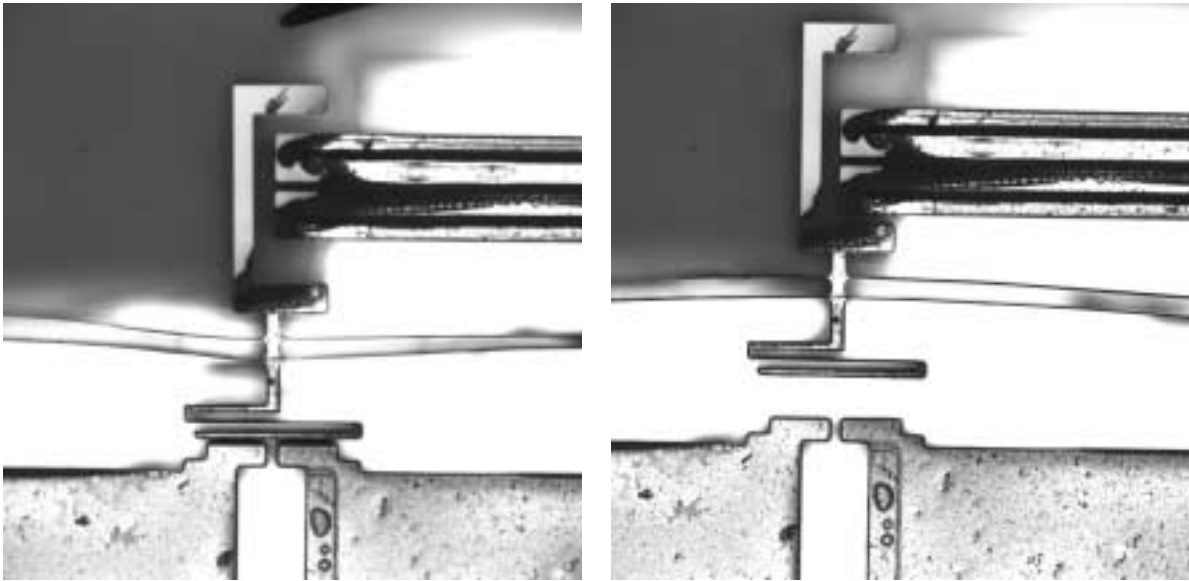


Figure 5-2 Au plated relay in G14

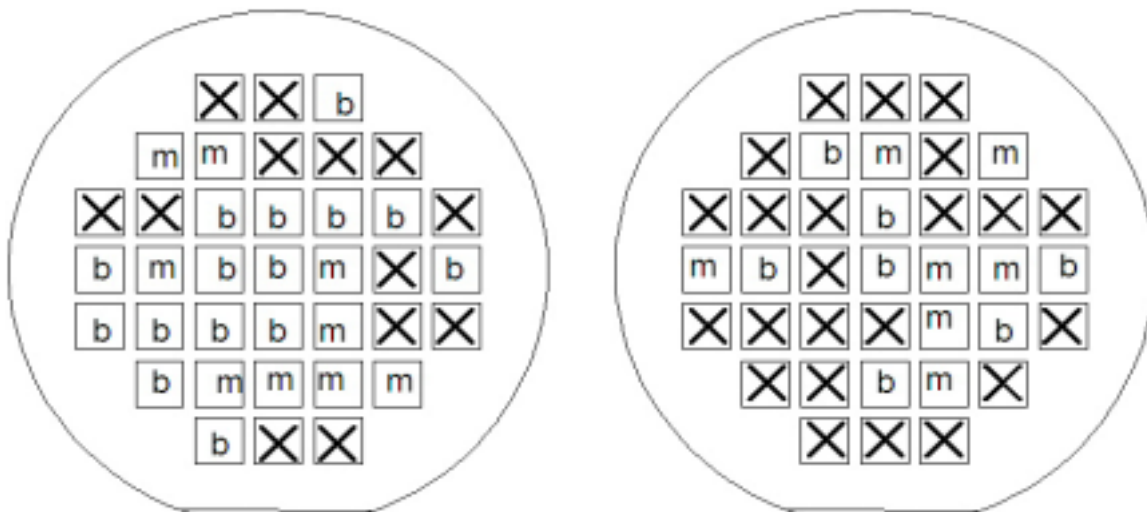


Figure 5-3 Bistability of G15 and G16. b (bistable) m(monostable), x(broken)

G16 was sputtered by Cu. The new metal was tested with the hope that the resistance would be low because of the lower resistivity of Cu than Au. Among the 37 dies, 14 devices survived, manual test shows that 7 of them were bistable as shown in Figure 5-3. Relay resistance was measured typically as 10-100 Ω 's. Four-point probe resistance tests on the same Cu pad gave a high resistance of several Ω 's. The high resistance was believed to

result from either the oxide layer on the Cu resulting from the hot sputtering process, or from the possible loose Cu structure from the sputtering process.

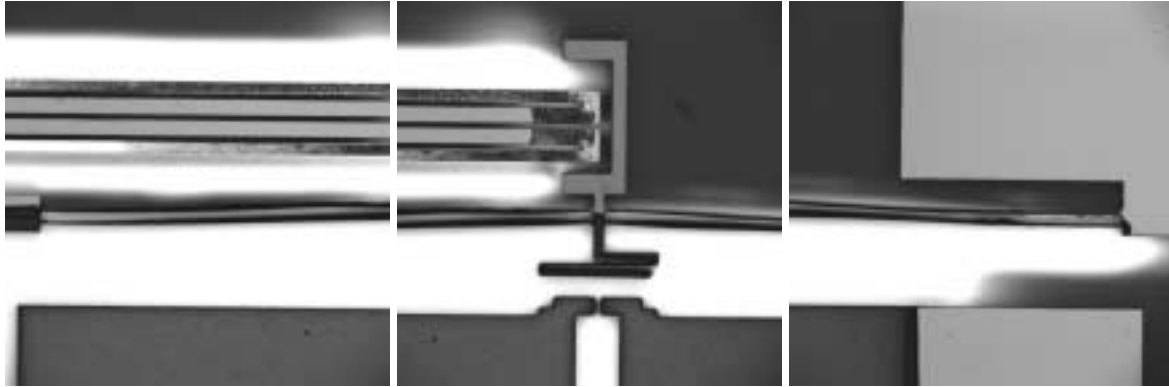
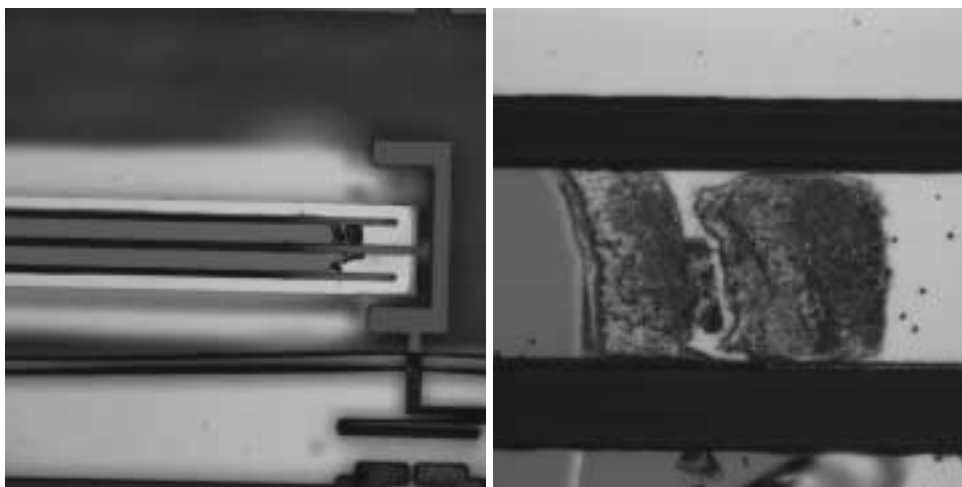


Figure 5-4 Cu plated relay in G15 after annealing

An annealing of 300 degree C and half hour was conducted on G15 and G16, but metal on many locations failed after the annealing, the reason was believed to be the low eutectic temperature between Cu and Si. The initial shape of the double beam changed after the annealing, as shown in Figure 5-4. This figure also shows that even some sputtered Au failed after the annealing at the tip of the thermal actuators. One upper thermal actuator that did not show Au failure was put under cyclic test, with actuation of 1 Hz and 50V, after 100,000 cycles, while still working, the metal on the tip of the thermal actuator recessed a little, as shown in Figure 5-5.



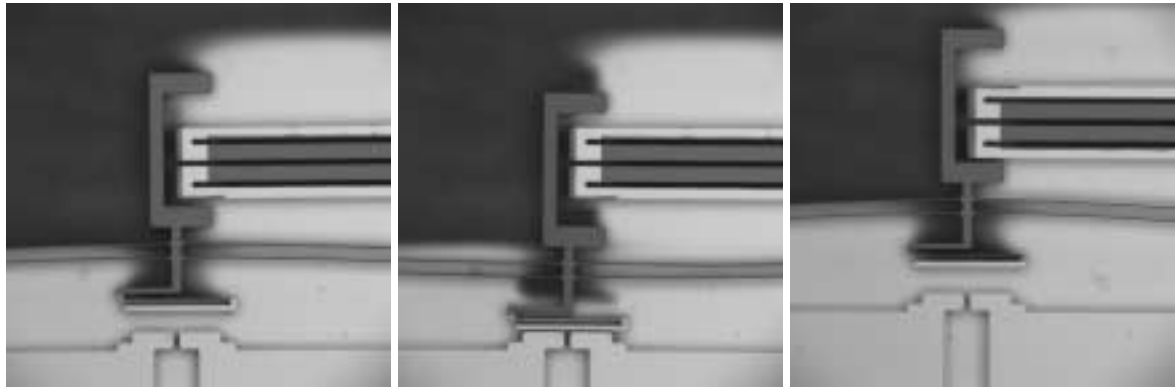
(a) zoom-out

(b) zoom-in

Figure 5-5 Upper thermal actuator in G15 after cyclic actuation

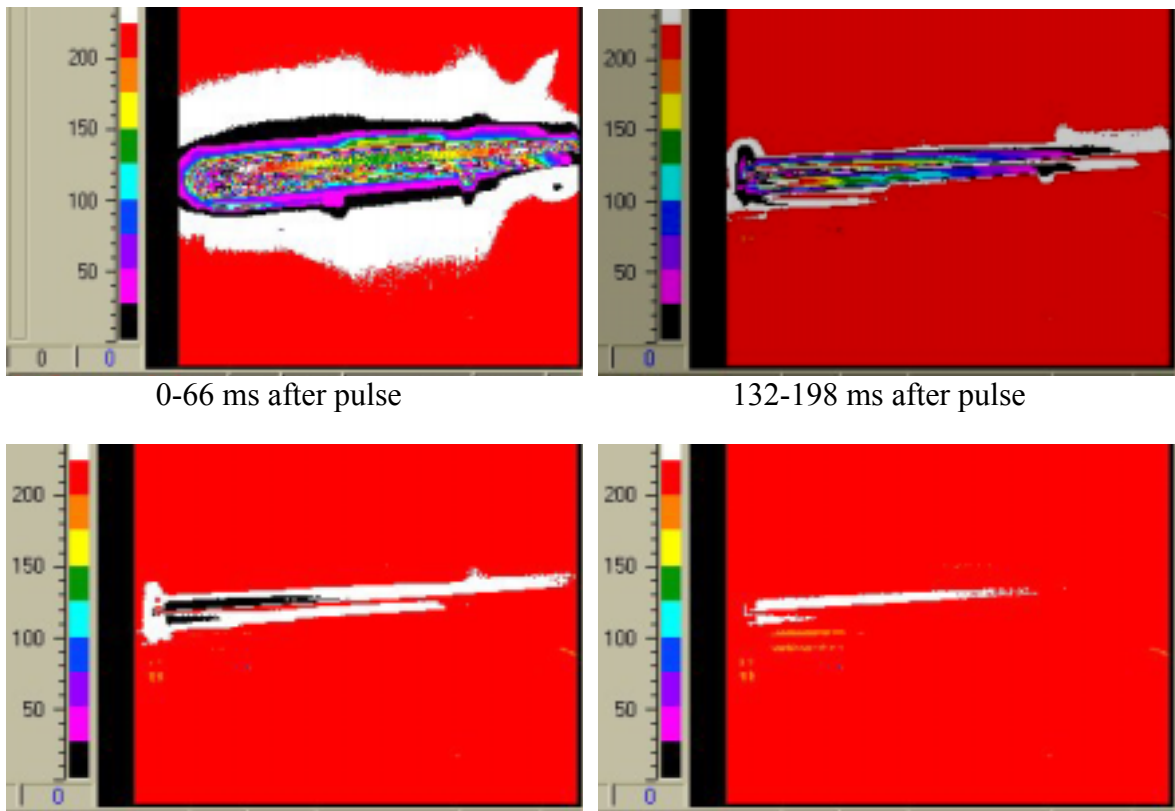
Two previous metalized wafers, G11 and G15, were stripped of metal and re-metalized for more testing, the new label are G17 and G18. G17 lost bistability, which may due to the

diffused metal into the silicon, which changes the mechanical property such as residual stress.



(a) Off-position (b) On-position (c) Lower actuator after cyclic test

Figure 5-6 G11 pictures



264-330 ms after pulse

442-508 ms after pulse

Figure 5-7 IR image of the thermal actuator in G18

An IR camera movie was taken of the thermal actuation on G18. Some images are shown in Figure 5-7. Due to the limited temperature, time and spatial resolution of the IR camera, only qualitative information can be obtained from the figure. The figure shows that it takes up to half second for the thermal actuator to cool down, which agrees well with thermal modeling predictions of equation (3.41).

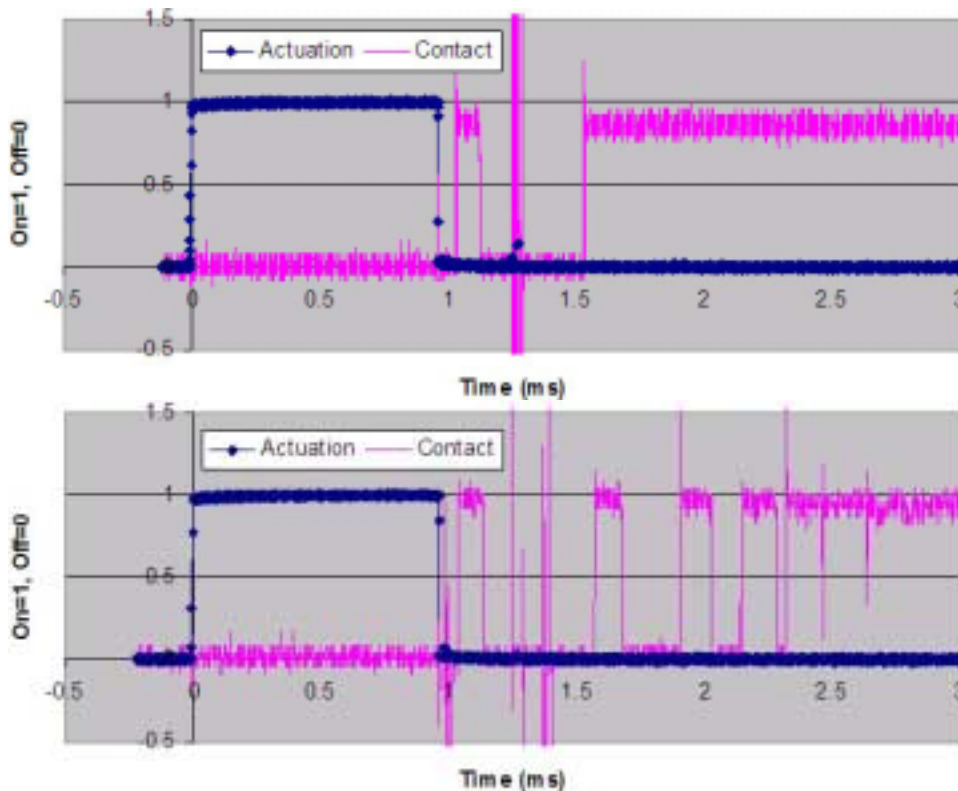


Figure 5-8 Switch-on contact response in G18

Due to the re-processing, G18 has only five unbroken dies, of which two of the double beams were bistable. The off-state and on-state of one of them are shown in Figure 5-6 (a) and (b). The thermal actuator works with voltage of 80-85volt. The actuation energy agrees with the theoretical prediction within a 20% difference. A cyclic test of the lower thermal actuator was done on one die in which the double beam was already broken before test, after 62000 cycles of actuation of 85V and 1Hz, the metal showed no degradation as shown in Figure 5-6 (c). Switch-on speed test was performed on G18 and two results are shown in Figure 5-8. The actuation voltage was ramped up until the relay just snapped the double beam from the open to the closed position. It was found that sometimes a voltage of 80 volt was needed, but sometimes 85 volts was needed. The pulse of the clear lines for 1 ms is the electrical actuation of the thermal actuator. The relay is switched on shortly after the pulse is off. The contacts bounced which takes 300 μ s. and then in some cases it would bounce for 3 or more times, and in other cases it would settle down after the first bounce.

Figure 5-9 shows the f-d curve measurement of the bistable mechanism. The thickness of the beam is 12 μm on mask, but the top thickness is only measured 7 μm for the fabricated beams. A model f-d curve for 7 μm beams, another model curve for 8 μm beams, and the flextester measured f-d curve are shown in the figure. Considering that the average thickness of beam is slightly larger than the top thickness, as indicated by the measurement of the beam shown in Figure 2-9, the measured force level can be explained by theory. Note that the measured displacement indicates that the double beam snaps through at a later point than prediction by theory, which is a typical f-d curve shifting if the beam is not pushed at the center.

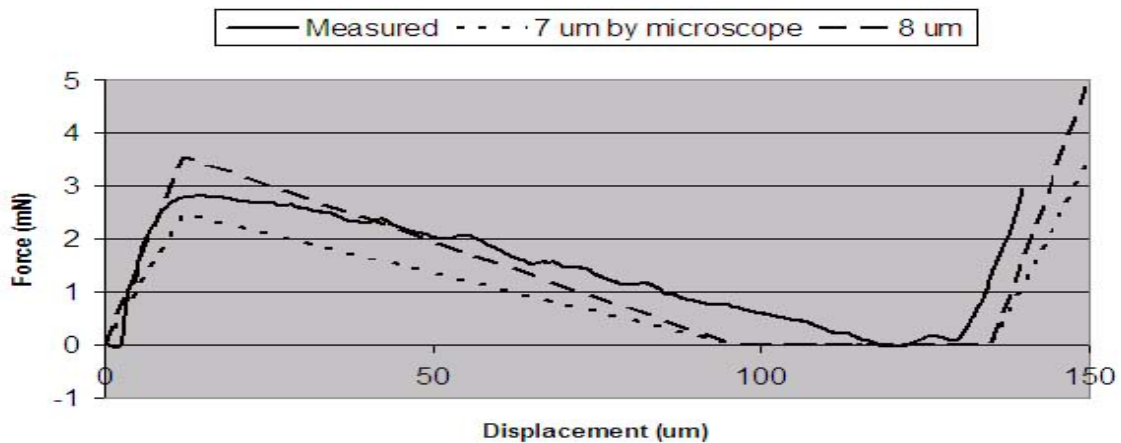


Figure 5-9 f-d measurement of the bistable mechanism in G18

In summary, MEMS relays are fabricated and tested. Functions of bistable structure, electrothermal actuator, and relay contact are realized. The force level of the bistable structure drifted from designed value due to the thinner beam thickness resulted from fabrication. However, the lower force level seemed to be adequate for the contact since higher force applied manually does not decrease the resistance. The yield of the fabricated relay is low. Working devices are usually below 50% of all fabricated ones. Future work on the reliability and yield is required.

Chapter 6

SUMMARY AND CONCLUSIONS

This thesis proposed, modeled, designed and fabricated an electrothermally-actuated bistable MEMS relay for power applications.

This thesis selected a straightforward deep etch and bonding fabrication sequence that facilitates the flexure design of relay components to meet the functional requirements (Section 1.2.2). One key requirement on this relay is its mechanical bistability. To have this, this thesis proposed and modeled several structures, among which a curved beam bistable mechanism is selected. The curved beam mechanism was modeled by buckling modal analysis, where the interaction of each mode, the beam axial force, and the beam lateral deflection were clearly revealed (Section 2.2). A double curved beam with high enough value of Q defined in equation (2.10) is designed to be bistable (Section 2.3). This mechanism is then micro-fabricated and tested (Section 2.4). The variation of the DRIE etched structure dimensions was identified, which affects the f-d curve of the bistable structure. The measured f-d curve by a specified MEMS flexure tester [26], however, agrees with modeling prediction based on the measured structure dimensions. The symmetry and stiffness of the curved beam bistable mechanism f-d curve was then optimized by a thin-thick-thin-thick-thin beam shape modulation (Section 2.5.1) and by a soft-spring coupler (Section 2.5.2).

This thesis then analyzed the feasibility of several actuators to actuate the bistable mechanism. A magnetic actuator was determined to not be practical. A taper comb drive actuator was feasible but required large size and sophisticated bearing design (Section 3.2.1). Preliminary study of electrostatic zipper actuator was carried out, and equations for a curved beam with rolling boundaries in an electrostatic field were formed reducing the problem to nonlinear ordinary differential equation arrays with fixed boundary conditions (Section 3.2.2). However, an electrothermal actuator was selected for its good actuation capability and simple fabrication, so detailed modeling and design was conducted on it. Two mechanical modes were developed, with the basic model (Section 3.1.2) giving closed-form solutions and the complete model (Section 3.1.3) accurately comprising the cross coupling relation of the beam force and deformation between lateral and axial directions. Electrothermal modeling (Section 3.1.5) showed the transient nature of the electrothermal actuator, which could be actuated by electrical pulse generated by a specialized external circuit designed and built.

For the relay contact, this thesis used a crossbar-contacts structure. Different shapes of the contact structure are fabricated and tested and the flat-flat one is selected (Section 4.1.1).

Crossbar compliance was designed so it can contact the two contacts reliably (Section 4.1.2). Then this thesis worked on design and processes to achieve good metalization and contact through the DRIE sidewalls. Two methods were conceived to alleviate the bottom-of-etch problem of DRIE, with the direct mounting method (Section 4.2.2.1) failed but the backside shallow etch method (Section 4.2.2.2) worked. Several processes were conceived to clean the Teflon residue of DRIE process, which caused metal adhesion problems. These cleaning steps, together with e-beam and sputtering, were carried out on silicon samples in a matrix study, which identified all cleaning steps as helpful and favored the sputtering over the e-beam metalization (Section 4.2.3.1). A wet etch experiment was carried out for removing the grooves at the sidewall resulted from DRIE etch, the result was positive but due to fast etch rate it was not included in the final relay device fabrication (Section 4.2.3.2). A three-step metalization process including cleaning, seed metal deposition by sputtering, and more metal deposition by electroplating (Section 4.2.3.3) was developed. An edge nibble method was conceived to help metal continuity over the sharp edge between wafer top surface and sidewalls, but the limited experiments did not identify such improvement (Section 4.2.4).

As described in Chapter 5, about twenty generations of relay devices were designed (Section 5.1), fabricated (Section 5.2), and tested (Section 5.3), with design and fabrication improvement from one generation to the next mainly driven by the need to lower the contact resistance. Several latest devices were tested in details. The current carrying capacity with the electroplated contacts were about 2-3A, and on-state resistance was on the order of 100m Ω , which are comparable to the best MEMS relays found in literature. The thermal actuator was tested but due to limited testing facilities, only rough quantitative data of the actuation power and temperature profile were obtained, which agreed with the design. The bistable double beam was again measured with a beam thickness smaller than mask value. The force was significantly less than design value but was consistent with measured beam dimension. Switching-on test of the relay shows that about 2 ms was needed for the relay to close and bounce.

The yield of the fabricated relays was low. Many double beams were etched away or broken during DRIE and subsequent handling. Among those survived, some were not bistable (Figure 5-3). During the cyclic test of the thermal actuator, it was found that the metal on some of the actuator gradually diffused into silicon (Figure 5-5). The relay has not been extensively tested for its long term contact behavior and arcing phenomenon. All these could be future work.

Appendix A

MATLAB CODE OF THE THERMAL ACTUATOR COMPLETE MODEL

mechbow.m

clear;

% dimensions: 1 is the hot beam, 2 is the cold beam
l1=6e-3; t1=80e-6; ew1=1.69e11*0.3e-3;
l2=l1; t2=80e-6; ew2=ew1; tg=80e-6; t0=(t1+t2)/2+tg;
alpha=3e-6; deltaT=220;

% nondimensional parameters

L2=l2/l1; T1=t1/l1; T2=t2/l2; T0=t0/l1; EPST=alpha*deltaT; EW2=ew2/ew1;

%Initial guesses for K1

K10_F=0.1; K10_DELTA1=0.1;

%Normalized blocked values and free values are obtained

[bDELTA1,bF,bK1,bF1,bM1,bF2,bM2]=blockedF(K10_F, L2, T1, T2, T0, EW2, EPST);
[fDELTA1,fF,fK1,fF1,fM1,fF2,fM2]=freeDELTA1(K10_DELTA1, L2, T1, T2, T0, EW2, EPST);

%blocked force=bF*foverF, free displacement=fDELTA1*doverDELTA1

bf=bF*ew1*t1^4/12/(l1^3); fdelta=fDELTA1*t1;

blockedF.m

function [DELTA1,F,K1,F1,M1,F2,M2]=blockedF(K10, L2, T1, T2, T0, EW2, EPST);

[K1,fval]=fminsearch(@error_blocked, K10, [], L2, T1, T2, T0, EW2, EPST);

if abs(real(fval))>1e-3 | abs(imag(fval))>1e-6

 fval

 [K1,fval]=fminsearch(@error_blocked, 2*pi, [], L2, T1, T2, T0, EW2, EPST);

end

if abs(real(fval))>1e-3 | abs(imag(fval))>1e-6

 fval

 error('K1 not found for blockedF');

end

```
[DELTA1,F,F1,M1,F2,M2]=K1solution(K1, L2, T1, T2, T0, EW2, EPST);
```

freeDELTA1.m

```
function [DELTA1,F,K1,F1,M1,F2,M2]=freeDELTA1(K10, L2, T1, T2, T0, EW2, EPST);
```

```
[K1,fval]=fminsearch(@error_free, K10, [], L2, T1, T2, T0, EW2, EPST);
```

```
if abs(real(fval))>1e-3 | abs(imag(fval))>1e-6
```

```
    fval
```

```
    [K1,fval]=fminsearch(@error_free, 2*pi, [], L2, T1, T2, T0, EW2, EPST);
```

```
end
```

```
if abs(real(fval))>1e-3 | abs(imag(fval))>1e-6
```

```
    fval
```

```
    error('K1 not found for freeDELTA1');
```

```
end
```

```
[DELTA1, F, F1, M1, F2, M2]=K1solution(K1, L2, T1, T2, T0, EW2, EPST);
```

error_blocked.m

```
function f=error_blocked(K1, L2, T1, T2, T0, EW2, EPST);
```

```
[DELTA1, F]=K1solution(K1, L2, T1, T2, T0, EW2, EPST);
```

```
f=DELTA1.^2;
```

error_free.m

```
function f=error_free(K1, L2, T1, T2, T0, EW2, EPST);
```

```
[DELTA1, F]=K1solution(K1, L2, T1, T2, T0, EW2, EPST);
```

```
f=F.^2;
```

K1solution.m

```
function [DELTA1, F, F1, M1, F2, M2]=K1solution(K1, L2, T1, T2, T0, EW2, EPST);
```

```
%straightforward calculations
```

```
K2=sqrt(T1.^3./T2.^3./L2./EW2).*K1;
```

```
EPS1=T1.^2.*K1.^2./12;
```

```
EPS2=T2.^2.*K2.^2./12;
```

```
%The rest of the variables are to be solved linearly
```

```
%x=[DELTA1 THETA1 F1 M1 DELTA2 THETA2 F2 M2]
```

```
%All the following functions should be zero
```

```

%fun1=EPST-EPS1-L2.*EPS-T1.^2.*(1./4.*(2.*K1.*(cos(K1)).^2-
3.*cos(K1).*sin(K1)+K1)./(cos(K1)).^2./K1.^5.*F1.^2+(-1)/4.*(cos(K1).*sin(K1)-
K1)/K1.^3./(cos(K1)).^2.*M1.^2+1./2.*(2.*(cos(K1)).^2+sin(K1).*K1-
2.*cos(K1))./K1.^4./(cos(K1)).^2.*F1.*M1)+T2.^2.*(1./4.*(2.*K2.*(cosh(K2)).^2-
3.*cosh(K2).*sinh(K2)+K2)./((cosh(K2)).^2.*K2.^5).*F2.^2+1./4.*(cosh(K2).*sinh(K2)-
K2)./(K2.^3.*(cosh(K2)).^2).*M2.^2+1./2.*(2.*(cosh(K2)).^2-sinh(K2).*K2-
2.*cosh(K2))./(K2.^4.*(cosh(K2)).^2).*F2.*M2)+THETA1.*T1.*T0
%fun2=THETA2-T1./T2.*THETA1;
%fun3=(tan(K1)-K1)/K1.^3.*F1+(1-cos(K1))/K1.^2./cos(K1).*M1-DELTA1;
%fun4=(1-cos(K1))/K1.^2./cos(K1).*F1+tan(K1)/K1.*M1-THETA1;
%fun5=(-tanh(K2)+K2)/K2.^3.*F2+(-1+cosh(K2))/K2.^2./cosh(K2).*M2-DELTA2;
%fun6=(-1+cosh(K2))/K2.^2./cosh(K2).*F2+tanh(K2)/K2.*M2-THETA2;
%fun7=DELTA1-T2.*L2./T1.*DELTA2;
%fun8=M1+1./L2.^3.*EB2.*T2.^4.*L2.^4./T1.^4.*M2+K1.^2.*T0./T1;

```

% The above functions can be written with the following constants

```

% a1+a2.*F1.^2+a3.*M1.^2+a4.*F1.*M1+a5.*F2.^2+a6.*M2.^2+a7.*F2.*M2+
a8.*THETA1=0
% THETA2-b1.*THETA1=0
% c1.*F1+c2.*M1-DELTA1=0
% d1.*F1+d2.*M1-THETA1=0
% e1.*F2+e2.*M2-DELTA2=0
% f1.*F2+f2.*M2-THETA2=0
% DELTA1-g1.*DELTA2=0
% M1+h1.*M2+h2=0

```

```

a1=EPST-EPS1-L2.*EPS2;
a2=-T1.^2.*1./4.*(2.*K1.*(cos(K1)).^2-3.*cos(K1).*sin(K1)+K1)./(cos(K1)).^2./K1.^5;
a3=T1.^2.*1./4.*(cos(K1).*sin(K1)-K1)/(K1.^3.*(cos(K1)).^2);
a4=-T1.^2.*1./2.*(2.*(cos(K1)).^2+sin(K1).*K1-2.*cos(K1))./(K1.^4.*(cos(K1)).^2);
a5=T2.^2.*1./4.*(2.*K2.*(cosh(K2)).^2-
3.*cosh(K2).*sinh(K2)+K2)./((cosh(K2)).^2.*K2.^5);
a6=T2.^2.*1./4.*(cosh(K2).*sinh(K2)-K2)./(K2.^3.*(cosh(K2)).^2);
a7=T2.^2.*1./2.*(2.*(cosh(K2)).^2-sinh(K2).*K2-2.*cosh(K2))./(K2.^4.*(cosh(K2)).^2);
a8=T1.*T0;

```

```

b1=T1./T2;
c1=(tan(K1)-K1)/K1.^3;      c2=(1-cos(K1))/K1.^2./cos(K1);
d1=(1-cos(K1))/K1.^2./cos(K1);  d2=tan(K1)/K1;
e1=(-tanh(K2)+K2)/K2.^3;      e2=(-1+cosh(K2))/K2.^2./cosh(K2);
f1=(-1+cosh(K2))/K2.^2./cosh(K2); f2=tanh(K2)/K2;
g1=T2.*L2./T1;
h1=1./L2.^3.*EW2.*T2.^4.*L2.^4./T1.^4;  h2=K1.^2.*T0./T1;

```

%The solution of the above equations are:

```

%F1=A1.*THETA1+A2
%M1=B1.*THETA1+B2
%F2=C1.*THETA1+C2
%M2=D1.*THETA1+D2
%DELTA1=E1.*THETA1+E2

```

```

denominator=(d2.*h1.*c1.*f1-d1.*c2.*h1.*f1+d1.*g1.*e1.*f2-d1.*g1.*e2.*f1);
A1=(-d2.*h1.*g1.*e1.*b1+c2.*h1.*f1-g1.*e1.*f2+g1.*e2.*f1)/denominator;
A2=(-d2.*h2.*g1.*e1.*f2+d2.*h2.*g1.*e2.*f1)/denominator;
B1=(h1.*c1.*f1-h1.*g1.*e1.*b1.*d1)/denominator;
B2=(-h2.*d1.*g1.*e1.*f2+h2.*d1.*g1.*e2.*f1)/denominator;
C1=(f2.*c1+b1.*d2.*h1.*c1-b1.*d1.*c2.*h1-b1.*d1.*g1.*e2)/denominator;
C2=(f2.*d2.*h2.*c1-f2.*d1.*c2.*h2)/denominator;
D1=(-(c1.*f1-g1.*e1.*b1.*d1)/denominator;
D2=(-(d2.*h2.*c1.*f1-d1.*c2.*h2.*f1)/denominator;
E1=g1.*(e1.*f2.*c1+e1.*b1.*c1.*d2.*h1-e1.*b1.*c2.*h1.*d1-e2.*c1.*f1)/denominator;
E2=g1.*(e1.*f2.*c1.*d2.*h2-e1.*f2.*c2.*h2.*d1-
e2.*c1.*f1.*d2.*h2+e2.*c2.*h2.*f1.*d1)/denominator;

```

```

%The above equations are reduced to: AA.*THETA1.^2+BB.*THETA1+CC=0
AA=a2.*A1.^2+a3.*B1.^2+a4.*A1.*B1+a5.*C1.^2+a6.*D1.^2+a7.*C1.*D1;
BB=2.*a2.*A1.*A2+2.*a3.*B1.*B2+a4.*A1.*B2+a4.*A2.*B1+2.*a5.*C1.*C2+2.*a6.*D1.*D2+a7.*C1.*D2+a7.*C2.*D1+a8;
CC=a1+a2.*A2.^2+a3.*B2.^2+a4.*A2.*B2+a5.*C2.^2+a6.*D2.^2+a7.*C2.*D2;

```

```

THETA1=(-BB+sqrt(BB.^2-4.*AA.*CC))/(2.*AA);

```

```

F1=A1.*THETA1+A2;
M1=B1.*THETA1+B2;
F2=C1.*THETA1+C2;
M2=D1.*THETA1+D2;
DELTA1=E1.*THETA1+E2;
F=F1+1./L2.^3.*EW2.*T2.^4./T1.^4.*L2.^4.*F2;

```

Appendix B

MASKS

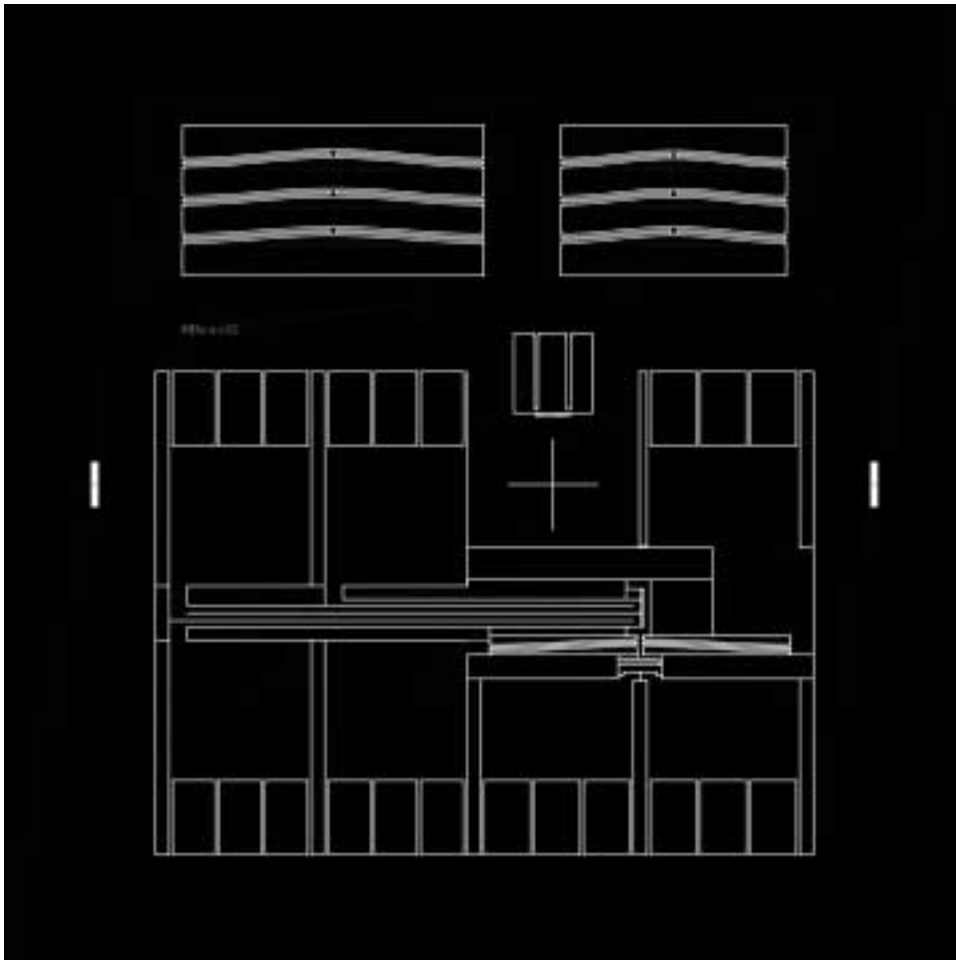


Figure B-1 Device mask

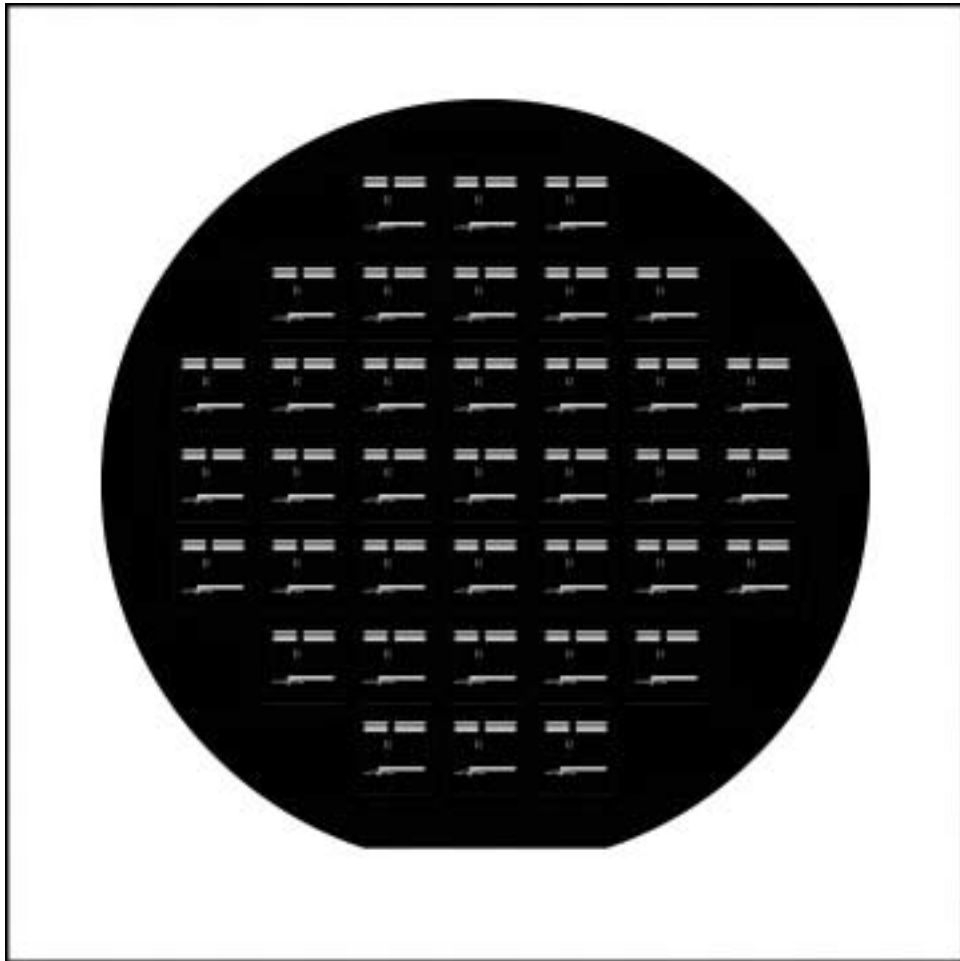


Figure B-2 Device backside mask

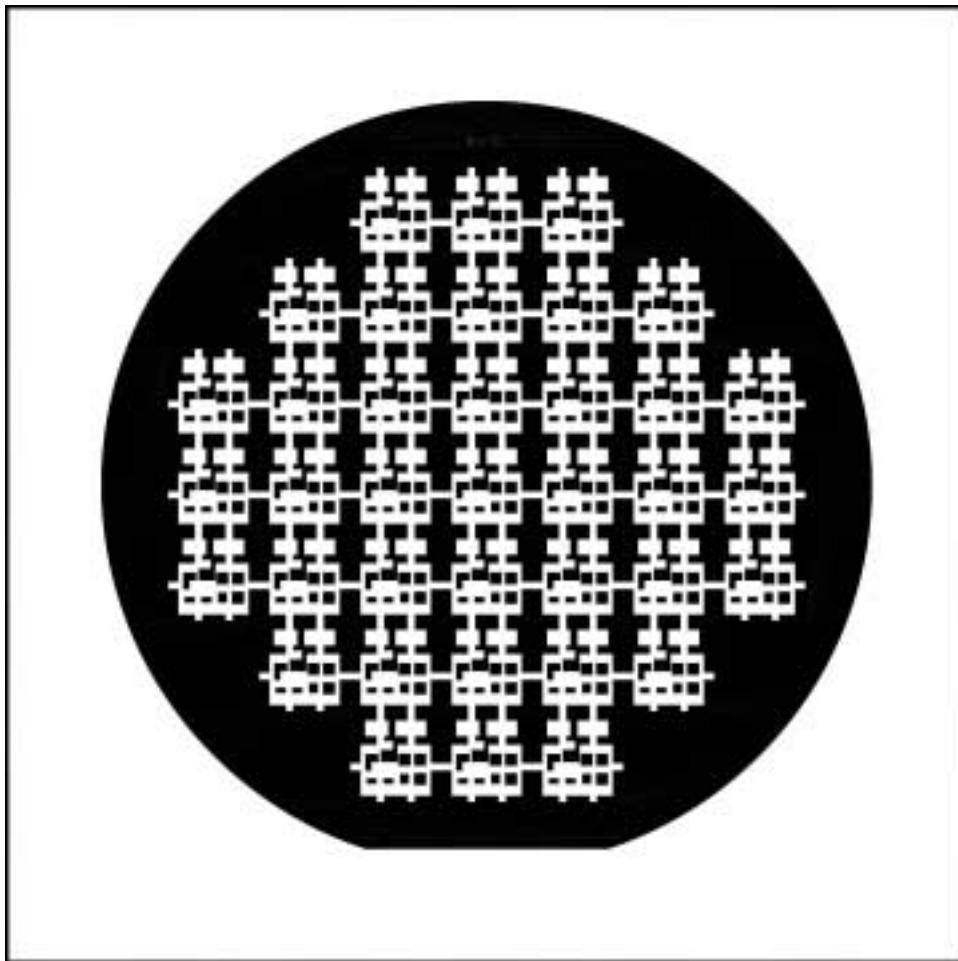


Figure B-3 Handle mask

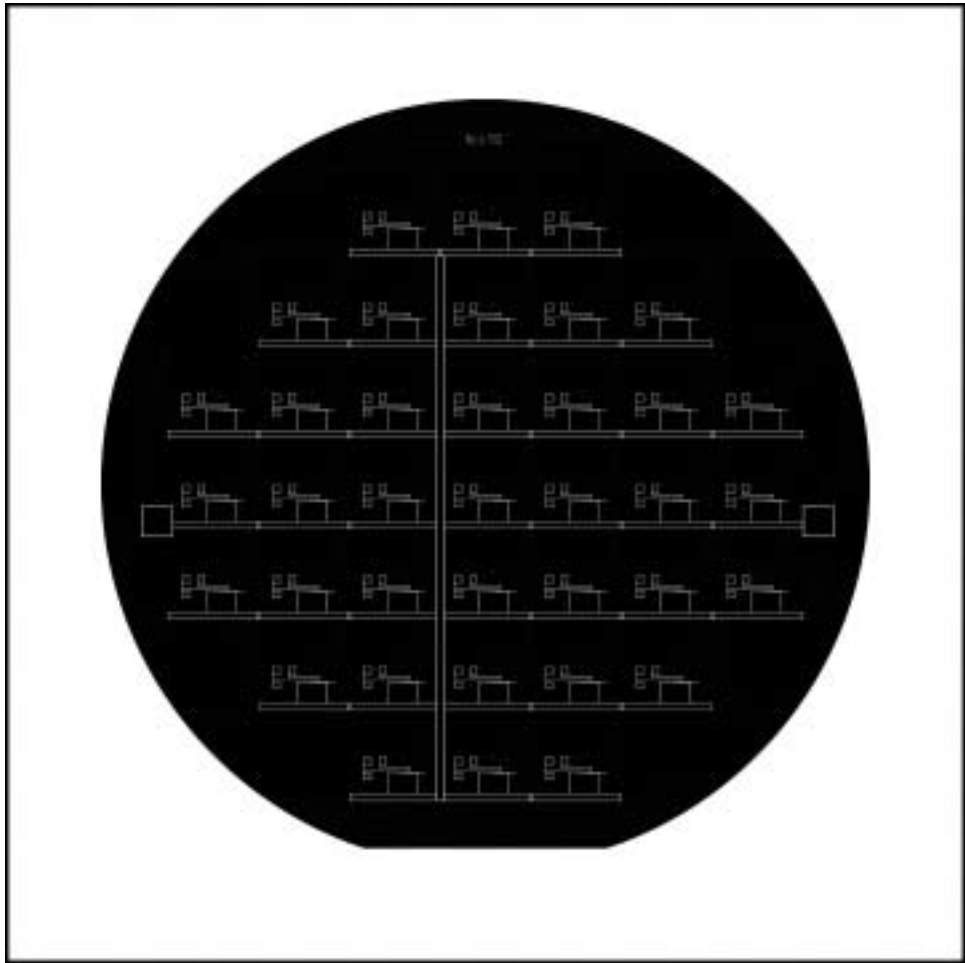


Figure B-4 Shadow mask

Appendix C

FABRICATION PROCESS FLOW

Table C-1 Fabrication process flow

Make chrome masks from transparency	
	Photolithography.
	Chrome wet etch.
	Nanostrip clean for half hour.
Handle wafer process	
	Coat pyrex wafer on both sides with double layers of thick resist
	Photolithography.
	50% HF dip for shallow etch.
Device wafer process	
	HMDS, coater, prebake on silicon wafer.
	Expose with stepper.
	Coat back side with thin resist.
	Expose back side.
	DRIE for 10 mins for backside, $\sim 20\mu\text{m}$
	DRIE MIT69 for three hour to through-etch for front side.
	Dismount device wafer from handle wafer in acetone.
	Piranha clean.
Shadow wafer process:	
	Photolithography.
	DRIE 2.5 hours to through-etch.
	Dismount by acetone and clean by piranha.
Bonding and metalization process:	
	Anodic bond handle wafer and device wafer.
	Temporarily bond shadow wafer to device wafer.
	Sputter 100A Ti, 1 μm Au onto the device.
	Separate shadow wafer from device wafer.
	Electroplate $\sim 2\mu\text{m}$ of Cu

Bibliography

- [1] S. Senturia, *Microsystem design*, 2000 Kluwer Academic Publishers.
- [2] N. Maluf, *An introduction to microelectromechanical systems engineering*, 2000 Artech House, Inc.
- [3] MEMS clearinghouse website: www.memsnet.org.
- [4] B. Jensen et al, Design of two-link, in-plane, bistable compliant micromechanisms, *Journal of Mechanical Design*, 121:3, 416-423, 1999.
- [5] J. Kassakian et al, *Principles of power electronics*, 1992 Addison-Wesley Publishing Company.
- [6] M. Galla et al, Design considerations for PPTC devices used as primary overcharge protection in battery packs, *Battery power products and technology* March 2003.
- [7] Y. Wang et al, Low-voltage lateral-contact micro relays for RF applications, *MEMS '02*, 645-648.
- [8] M. Ruan et al, Latching micro magnetic relays with multistrip permalloy cantilevers, *MEMS '01*, 224-227.
- [9] J. Simon et al, A liquid-filled microrelay with a moving mercury microdrop, *Journal of MEMS* 6 (1997), 208-216.
- [10] H. Lee et al, Electrostatically actuated copper-blade microrelays, *Sensors and Actuators A* 100 (2002), 105-113.
- [11] J. Wong et al, An electrostatically-actuated MEMS switch for power applications, *MEMS '00*, 633-638.
- [12] W. Taylor et al, Fully integrated magnetically actuated micromachined relays, *Journal of MEMS* 7 (1998), 181-191.
- [13] J. Qiu et al, A high-current electrothermal bistable MEMS relay, *MEMS '03*, 64-67.
- [14] M. Hoffmann et al, All-silicon bistable micromechanical fiber switch based on advanced bulk micromachining, *IEEE Journal on Selected Topics in Quantum Electronics*, Vol 5:1, 46-51, 1999.
- [15] X. Sun et al, A bistable microrelay based on two-segment multimorph cantilever actuators, *MEMS '98*, 154-159.
- [16] E. Kruglick et al, Bistable MEMS relays and contact characterization, *Proc Solid-state sensors and actuators Workshop*, 333-337, 1998.
- [17] M. Taher, On a tunable bistable MEMS-theory and experiment, *Journal of MEMS*, Vol 9:2, 157-170, 2000.
- [18] M. Vangbo, Analytical analysis of a compressed bistable buckled beam, *Sensors and Actuators A*, 69:3, 212-216, 1998.
- [19] Y. Yang et al, Testing and characterization of a bistable snapping microactuator based on thermo-mechanical analysis, *Proc. Solid-state sensors and actuators*, 1995, 337-340.
- [20] B. Wagner et al, Bistable microvalve with pneumatically coupled membranes, *MEMS '96*, 384-388.
- [21] J. Qiu et al, A feasibility study of bistable micro-relays, internal report, 1999.

- [22] J. Qiu et al, A centrally-clamped parallel-beam bistable MEMS mechanism, MEMS '01, 353-356.
- [23] M. Brenner et al, Optimum design of a MEMS switch, Proc. 5th International Conf. on Modeling and Simulation of Microsystems, USA. April 2002.
- [24] J. Kim et al, Why is (111) Silicon a better mechanical material For MEMS, Transducers '01, 2C1.02.
- [25] K. Chen et al, Silicon strength testing for mesoscale structural applications, MRS Spring Meeting Symposium, N3.8.
- [26] J. Qiu et al, An instrument to measure the stiffness of MEMS mechanisms, Proc 10th International Conference on Precision Engineering, July 2001, Yokohama Japan.
- [27] J. Comtois et al, Characterization of electrothermal actuators and arrays fabricated in a four-level, planarized surface-micromachined polycrystalline silicon process, Transducers '97, 769-772.
- [28] C. Lott et al, Modeling the thermal behavior of a surface micromachined linear-displacement thermomechanical microactuator, Sensors and Actuators A 101 (2002), 239-250.
- [29] F. Pourahmadi et al, Silicon accelerometer with new thermal self-test mechanism, Solid-state sensor and actuator workshop, 1992, 22-25.
- [30] J. Li et al, Low Pull-In Electrostatic Curved Electrode Actuators Using Deep Reactive Ion Etching, to appear in Transducers'03.
- [31] H. Robbins et al, Chemical etching of silicon I. the system HF, HNO₃, and H₂O, Journal of the electrochemical society, June 1959 505-508.
- [32] J. Qiu et al, Bistable actuation techniques, mechanisms, and applications, US patent pending, filed by MIT January 2002.
- [33] A. Slocum et al, Characterization of microstructure force-displacement behavior, US patent pending, filed by MIT January 2002.
- [34] J. Qiu et al, A curved beam bistable mechanism, to be submitted to Journal of MEMS.